

**COLLOIDAL NANOPARTICLES TETHERED BY OLIGOMERS AND SHORT
POLYMERS IN ORGANIC AND POLYMERIC MEDIA**

A Dissertation

by

MIN HAO WONG

Submitted to the Office of Graduate Studies of
Texas A&M University
in partial fulfillment of the requirements for the degree of

DOCTOR OF PHILOSOPHY

Approved by:

Chair of Committee,	Hung-Jue Sue
Committee Members,	Hongcai Zhou
	Karen L. Wooley
	Mustafa Akbulut
Intercollegiate Faculty Chair,	Ibrahim Karaman

May 2013

Major Subject: Materials Science and Engineering

Copyright 2013 Min Hao Wong

ABSTRACT

Nanoparticles and related nanomaterials are increasingly being utilized in technological applications. Controlling the dispersion and organization of these advanced materials is crucial towards realizing their full potential. In this dissertation, we employ methods of tethering oligomers and short polymers to the surfaces of spherical nanoparticles and 2D crystals. ZnO quantum dots are spherical nanoparticles which are direct bandgap semiconductors (3.37 eV) with large exciton binding energies (60 meV) and show strong photoluminescence. We show that poly (methyl methacrylate) grafted onto ZnO quantum dots via radical polymerization yields polydisperse brushes that are particularly effective in forming stable, fine dispersions in melt-blended nanocomposites. Nanocomposites prepared via this method exhibit tunable properties in refractive index, glass transition temperature and energy bandgap as a result of their linear dependence on ZnO concentration. It is further shown that the glass transition behavior of these nanocomposites is analogous to that of polymer thin films.

α -ZrP nanoplatelets are 2D crystals which are being studied for use as a catalyst, drug delivery agent, proton conductor, nanofillers for nanocomposites, etc. Exfoliated α -ZrP nanoplatelets of large aspect ratios tethered by polyoxyalkyleneamines form photonic structures in high polar, aprotic solvents. The polyoxyalkyleneamines form a brush layer on the nanoplatelets allowing the formation of lamellar phases with large d -spacings. Bragg reflection by the mesomorphic structures in the visible wavelengths gives rise to iridescence with brilliant colors that are tunable by adjusting the

concentration of nanoplatelets. In epoxy, α -ZrP nanoplatelets tethered by polyoxyalkyleneamines self-assemble into smectic phase when spray-coated onto polyimide substrates. These spray-coated thin films of smectic α -ZrP/epoxy exhibit excellent gas barrier properties that perform consistently in low and high humidity conditions. The highly ordered nanoplatelets are aligned parallel to the substrate forcing gas molecules to traverse a tortuous path resulting in a reduction of permeability in the film. Observations of the occurrence of liquid crystalline phases in the bulk α -ZrP/epoxy liquid shows that the self-assembly behavior of these smectic α -ZrP are consistent with the predictions of Onsager's theory.

DEDICATION

To my wife, *Rumi*, who supported me through all these years in my Ph.D. research, and my son, *Alexander*, who is the joy and hope of my life.

In loving memory of my mother, Cheh Har Nui (1943-2002)

ACKNOWLEDGEMENTS

I am deeply indebted to Dr Sue, who has served as my mentor and advisor. Throughout all these years, he has given me the freedom to pursue the research that I am interested in. I would also like to express my gratitude to Dr Takahara, who has mentored me in the field of synchrotron-based x-ray scattering techniques, Dr Ishige, who has taught me so much about liquid crystals, Johannes and Dr Blümel, for helping me with NMR spectroscopy, my committee members who have spent time and effort advising on my research and special thanks in particular to Dr Wooley, who has given me access to her lab with all the instruments that were crucial to my research.

Thanks also go to the people at MIC and MCF who have helped me with instrumentation. Special thanks are given to Daehak and Dr Krishnamoorti, at the University of Houston who allowed me to use their SAXS.

My colleagues, Ehsan, Spencer, Kevin White, Kevin Laux, Sugiyama-san, Peng Liu and Mohammed, Jerry, Haiqing, Peng Li and others who I have spent every group meeting together debating on issues; I would like to express my thanks to you.

My deepest gratitude goes to my family, my father and sister who have supported me all these years when I have been away from home, my wife, Rumi, who has endured a less than comfortable life in a foreign land so different from home yet given me her unwavering support while I worked on my Ph.D., and finally my son, Alexander, who has given me the greatest joy and hope I have ever had.

TABLE OF CONTENTS

	Page
ABSTRACT	ii
DEDICATION.....	iv
ACKNOWLEDGEMENTS	v
TABLE OF CONTENTS	vi
LIST OF FIGURES	viii
LIST OF TABLES.....	x
CHAPTER I INTRODUCTION AND LITERATURE REVIEW.....	1
1.1 Introduction.....	1
1.2 Polymer Brushes	3
1.3 Dispersion and Organization of Nanoparticles	5
1.4 Functional Properties Arising from Incorporation of Nanoparticles	8
CHAPTER II STABLE DISPERSIONS OF NANOPARTICLES TETHERED WITH SHORT, DENSE AND POLYDISPERSE BRUSHES IN POLY(METHYL METHACRYLATE)*	15
2.1 Introduction.....	15
2.2 Materials and Methods	16
2.3 Characterization	19
2.4 Oligomer-Grafted Nanoparticles.....	23
2.5 Fine, Stable Dispersion of Nanoparticles	31
2.6 Nature of Brushes.....	42
2.7 Physics of Stable, Fine Nanoparticles Dispersion.....	46
2.8 Conclusions.....	48
CHAPTER III GLASS TRANSITION TEMPERATURE CHANGES OF MELT- BLENDED POLYMER NANOCOMPOSITES CONTAINING FINELY DISPERSED ZINC OXIDE QUANTUM DOTS*	51
3.1 Introduction.....	51
3.2 Methods and Materials	52

	Page
3.3 Transparent Nanocomposites Composing of Fine Dispersions of Nanoparticles	56
3.4 Linear Dependence of T_g on ZnO Concentration.....	57
3.5 A Quantitative Model for T_g Behavior in Nanocomposites.....	64
3.6 Conclusions.....	72
CHAPTER IV IRIDESCENCE OF α-ZrP NANOPATELETS IN ORGANIC SOLVENTS DUE TO LYOTROPIC MESOMORPHISM.....	75
4.1 Introduction.....	75
4.2 Methods and Materials	75
4.3 Oligomer-grafted α -ZrP Nanoplatelets.....	78
4.4 Iridescence of α -ZrP Nanoplatelets in Organic Solvents	81
4.5 Lyotropic Mesomorphism of α -ZrP Nanoplatelets in Organic Solvents.....	85
4.6 Conclusions.....	87
CHAPTER V SPRAY-COATABLE SMECTIC 2D CRYSTALS/EPOXY FILMS.....	89
5.1 Introduction.....	89
5.2 Methods and Materials	92
5.3 Oligomer-grafted α -ZrP Nanoplatelets.....	96
5.4 Spray-coated α -ZrP/Epoxy Films.....	101
5.5 Gas Barrier Properties of Spray-coated α -ZrP/Epoxy Films	104
5.6 Self-assembly Mechanism of Smectic α -ZrP/Epoxy Films.....	109
5.7 Conclusions.....	116
CHAPTER VI CONCLUSIONS.....	118
CHAPTER VII FUTURE RESEARCH	121
7.1 Structured Nanoparticles in Melt-processable Polymers.....	121
7.2 Phase Behavior and Preparation of Smectic α -ZrP/Epoxy.....	122
7.3 Control and Stabilization of Photonic Structures of 2D Crystals	122
7.4 Exploring Novel Functional Properties with Different Form Factors.....	123
REFERENCES	125

LIST OF FIGURES

	Page
Figure 1.1 Illustration of Onsager’s theory explaining the isotropic–nematic transition of rigid rods.	7
Figure 2.1 (a) Reaction scheme for the preparation of PMMA-grafted ZnO.....	24
Figure 2.2 (a) TEM image of PMMA-grafted ZnO dispersed by melt blending in neat PMMA, (inset) HRTEM of PMMA-grafted quantum dots.....	26
Figure 2.3 Gel permeation chromatography (GPC) trace of commercial and grafted PMMA.....	27
Figure 2.4 Monomer conversion during radical copolymerization of MMA and silanized ZnO.....	28
Figure 2.5 TEM images of unannealed (Batch 1) nanocomposites (left column) and nanocomposites annealed at 160°C for 5 days (right column).....	33
Figure 2.6 (a) UV-Vis transmission of annealed nanocomposite sheets at different ZnO loadings showing high transmission levels close to neat PMMA.....	35
Figure 2.7 Graphical method for determining the density of silane. Error bars indicate standard deviation.	38
Figure 2.8 (a) Linear dependence of T_g to ZnO weight fraction demonstrates tunability of T_g by varying ZnO loading.....	41
Figure 2.9 (a) AFM height image of a 2 μm \times 2 μm area of PMMA-grafted ZnO deposited on Si wafer.....	45
Figure 3.1 ZnO nanocomposite bars made by injection molding are shown in the photograph on the left, showing excellent transparency even after thermal processing.....	57
Figure 3.2 Representative DMA curves for different weight fractions of nanocomposite.	58
Figure 3.3 Representative normalized DSC curves for different weight fractions of nanocomposite.....	60
Figure 3.4 (a) Increasing T_g with ZnO weight fraction, w_{ZnO} . DMA data from E'' (half-filled symbols) and $\tan \delta$ peaks (open symbols) are presented.....	63

	Page
Figure 3.5 DMA data from E'' (half-filled symbols) and $\tan \delta$ peaks (open symbols) and DSC data (filled symbols) are presented.	67
Figure 4.1 Two possible mechanisms to increase interlamellar spacing.	79
Figure 4.2 (a) Transmission electron micrograph of irregular hexagons of α -ZrP nanoplatelets.	81
Figure 4.3 (a) Reflection spectra of 625 nm α -ZrP nanoplatelets in butyronitrile at various concentrations.	82
Figure 4.4 (a) Peak positions (λ_{max}) of reflectance spectra against ZrP wt%, demonstrating the dependence of iridescence color on ZrP concentration.	84
Figure 4.5 (a) Photograph of an acetone solution containing α -ZrP nanoplatelets enclosed in a glass cell under white light displays brilliant blue color.	86
Figure 4.6 Atomic force micrographs of single ZrP nanoplatelet (~760 nm) on silicon wafer.	87
Figure 5.1 Process of spray-coating smectic 2D crystals /epoxy films.	91
Figure 5.2 (a) Transmission electron microscopy of α -ZrP nanoplatelets with average size of 100 ± 51 nm.	98
Figure 5.3 Evidence of smectic phase in spray-coated film.	100
Figure 5.4 Optical microscopy of smectic (4.4 vol%) α -ZrP/epoxy films.	103
Figure 5.5 Gas barrier property of films.	105
Figure 5.6 Smectic (4.0 vol%) α -ZrP/epoxy liquid.	107
Figure 5.7 Molding process for α -ZrP/epoxy bulk nanocomposites.	110
Figure 5.8 Smectic (4.4 vol%) α -ZrP/epoxy nanocomposite.	112
Figure 5.9 Transmission electron microscopy of smectic (4.4 vol%) α -ZrP/epoxy nanocomposite.	115

LIST OF TABLES

	Page
Table 1.1 List of permeability models for filled polymer systems.....	14
Table 2.1 Processing condition in blending the PMMA-g-ZnO with PMMA.....	18
Table 2.2 Experimental conditions for the grafting of PMMA to ZnO.....	30
Table 2.3 Densities of the components of PMMA-grafted ZnO.....	38
Table 3.1 Comparison of $T_{g,bulk}$ and derived characteristic lengths.....	69

CHAPTER I

INTRODUCTION AND LITERATURE REVIEW

1.1 Introduction

Nanoparticles and related nanomaterials are increasingly used in all aspects of the technological world we live in. There are many areas of research in this subject that is worthy of serious academic investigation, but this dissertation is decidedly focused on the practical and applied aspects. In the sense that we are seeking methods to maximize the potential of using these materials by demonstrating practical and efficient production, substantial improvement of properties or creating new opportunities for technological applications. This is achieved by tethering oligomers or short polymers to the surface of these nanoparticles.

An oligomer is defined as a molecule of *intermediate relative molecular mass* which comprises of a small plurality of units derived from molecules of lower relative molecular mass (IUPAC definition). As such there is no strict limit on the molecular mass that can be defined as an oligomer other than that it should not be too large but it should be larger than a monomer. For the purpose of this dissertation, an oligomer is defined as having a degree of polymerization (N) of 100 or less. The reason being polymers of such low N possess properties (mechanical, physical, thermal etc.) that are significantly different from larger polymer chains to be classified in a different category. This classification also satisfies the IUPAC definition of a molecule having an intermediate relative molecular mass, where properties will vary significantly with the

removal of one or a few of the monomer units. The selection of using oligomers to modify nanoparticles is intentional. They are larger than the small molecules frequently used which are often highly reactive, toxic or unstable over long periods of time. In contrast, oligomers resemble polymers in terms of stability and non-toxicity but are easier to prepare due to the lower degree of polymerization. Oligomers are also better at improving the affinity of nanoparticles to polymer matrices due to their similar structures when compared to small molecules. Thus, the overall theme of this dissertation can be understood as exploring the use of oligomers on nanoparticles to achieve meaningful functional properties in organic media, including polymeric matrices.

This dissertation is organized as follows: Chapter I reviews the literature relevant to this research. Chapter II discusses the stable dispersion of polymer-grafted zinc oxide (ZnO) spherical nanoparticles formed via a melt-blending process. Chapter III discusses further the implications of this nanocomposite on the glass transition behavior of the polymer. Chapter IV discusses α -zirconium phosphate (α -ZrP) nanoplatelets that self-assemble into lamellar structures in organic solutions. Chapter V discusses the formation of large-scale ordered liquid crystalline structures of α -ZrP nanoplatelets. Each chapter from Chapters II to V is an independent, complete work of research in its own right, at the same time, they are also linked by the fact that tethering oligomers to the nanoparticles can result in very significant and often interesting changes to their behavior. Chapter VI presents the conclusions of this dissertation and Chapter VII suggests the future directions for this work.

1.2 Polymer Brushes

Inorganic nanoparticles tethered with polymer brushes are an important class of materials with unique properties that are dependent on the nature of the brushes. They form extremely stable Pickering emulsions (1) and have been shown to self-assemble into 2D ordered structures (2, 3). Recent progress suggests that colloids comprised of such nanoparticles are also promising candidates as stimuli-responsive materials (4) that respond to thermal (1, 5, 6) and pH (7-9) stimuli, opening up new vistas for applications. The use of functional inorganic nanoparticles such as titanium dioxide (10), silica (11, 12), aluminium oxide (13), iron oxide (14), zinc oxide (15-17), cadmium selenide (18), gold (19) and others in nanocomposites is a promising approach to introduce new functionalities to a polymer such as tunable refractive index, magnetism, surface hardness, UV absorption, etc. However, aggregation of nanoparticles is commonly encountered, leading to unsatisfactory performance of nanocomposites and frustrating efforts to utilize functional nanoparticles in applications. Many approaches exist to alleviate the aggregation problem. Amongst them, the polymer brush/nanoparticle system remains the most promising. This is due to the fact that numerous examples of stable and highly dispersed nanoparticles in nanocomposites already exist. Such stable dispersions work through the “wetting-dewetting” phenomenon of polymer brushes. Wetting of the brush by free polymer chains ensures a good dispersion while dewetting of the brush, forming the so-called “dry brush”, encourages aggregation of the nanoparticles. Wetting occurs when free polymers mix freely with the grafted polymer brush; conversely, dewetting occurs when free polymers do not penetrate into the brush

and as a consequence, no mixing happens. In the absence of enthalpic effects, i.e. interactions due to different brush-matrix chemical structures, and other effects such as magnetic or electrostatic attractions, the dispersion of polymer-grafted nanoparticles in a chemically identical matrix is determined by entropic factors. Existing studies done on polymer brushes on flat (20, 21) and curved surfaces (22, 23) identified several parameters, namely matrix polymer degree of polymerization P , brush polymer degree of polymerization N and graft density σ , that are critical in determining the formation of a stable dispersion. There is an entropic penalty associated with stretching out a coiled chain when matrix polymer and brush polymer interpenetrate. A longer brush polymer suffers less penalty to stretch out, thus for $N > P$ brush-polymer interpenetration is favorable, which leads to wetting of the brush and good dispersion. Conversely, when $P > N$, dewetting of the brush occurs, which results in poor dispersion. Hasegawa *et al.* (22) examined in detail the effect of graft density on the aggregation phenomenon in polymer/particle mixtures and concluded that when $P \sim N$ an optimal graft density σ_c can be estimated by $\sigma_c \approx N^{-1/2} a^{-2}$, where a is the monomer size. Experimental studies have generally confirmed these predictions in both planar and colloidal brushes (14, 19, 24-26). Recently, it has been recognized that surface curvature plays a huge role in the dispersion of nanoparticles (27, 28) to account for the fact that good dispersion is still observed in cases where $P > N$ (14).

1.3 Dispersion and Organization of Nanoparticles

1.3.1. Spherical Nanoparticles

Spherical nanoparticles are perhaps the most studied nanoparticles. This category of nanoparticles is the simplest in shape, and most readily analyzed in many phenomenon. Through clever techniques such as, sedimentation (29), electrophoresis (30), evaporation induced self-assembly (31) or template-directed crystallization (32) they can be induced to form highly ordered colloidal crystals. The structures created from these techniques tend to be common crystal lattices such as face centered cubic or hexagonal lattices due to the homogeneous surface properties of each nanoparticle. Anisotropy can be introduced to the spherical particles by preparing Janus particles, where each particle possesses two halves of contrasting surface properties, *e.g.* hydrophilic vs. hydrophobic. Highly complex structures can be formed from the interactions of these particles due to preferred directions of connection (33, 34). In general, an isotropic dispersion in polymer matrices is expected from polymer-grafted spherical nanoparticles. However, anisotropic assemblies of polymer-grafted nanoparticles have been reported in polymer matrices (26). This is a surprising result considering that the surface of the nanoparticles is homogeneous. The observations were reconciled with simulations and explained as an emergent property resulting from a competition between a short-range attraction and long-ranged repulsive interaction between nanoparticles.

1.3.2. 2D Crystals

2D crystals, alternatively nanosheets or nanoplatelets, are flat monolayers of nanoparticles with very high aspect ratios due to their thin thicknesses and very large

lateral dimensions. 2D crystals have been proven to show a rich variety of mesophases including nematic (35, 36), smectic (37, 38), columnar (39, 40) and even chiral phases (41). The complex liquid crystalline behavior of 2D crystals presents opportunities to control the assembly of these crystals to create mesoscale structures with unique properties. Composites of smectic liquid crystal polymers and boron nitride particles greatly enhanced thermal conductivity in both the normal and in-plane directions (42). The ability to form liquid crystalline phases in solutions is critical to allowing highly aligned fibers of high mechanical performance materials to be spun, which is the only practical means of forming such fibers. Some examples of which include Kevlar, Twaron, carbon nanotubes (43-45) and graphene oxide and reduced graphene (41). A key feature of this processing method is that the resulting fibers inherit the orientation and alignment from the liquid crystalline phase in the parent solution, which is largely responsible for the observed superior properties. The discovery of the unique properties of graphene (46, 47) has led to a surge in the study of other classes of 2D crystals such as silicates, metal oxides and hydroxides (48, 49), phosphates (50), transition metal dichalcogenides (48, 51, 52) and boron nitride (48, 51, 52), etc. The possibility of using such a wide range of materials in the form of liquid crystals permits the engineering of new advanced materials that couples the intrinsic properties of these materials with the properties arising from the mesoscale structures.

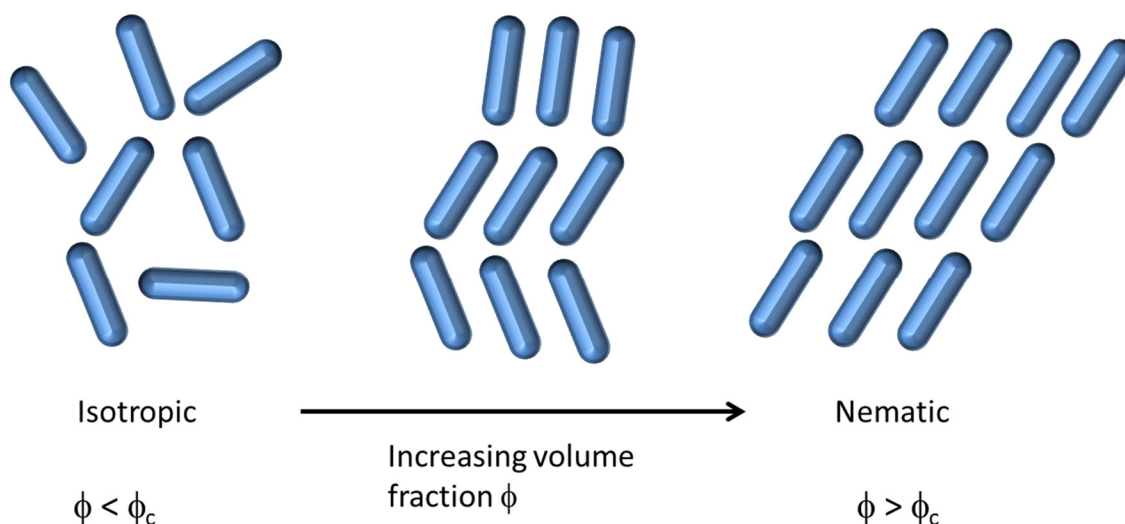


Figure 1.1 Illustration of Onsager’s theory explaining the isotropic–nematic transition of rigid rods.

Onsager’s theory predicts that hard rigid rods form nematic phases at high volume fractions, due to a net gain in entropy as the increased translational entropy compensates for the loss of orientational entropy (Figure 1.1), and the critical volume fraction ϕ_c for isotropic to nematic transition is lower for rods with high aspect ratios (53). A similar behavior is observed in 2D crystals. The challenge then is to preserve the long-range orientational and positional order of mesomorphic 2D crystals from the parent solution to a robust form that can be used to address technological needs. Even though the high orientational and positional order of graphene oxide and reduced graphene 2D crystals is preserved in the fibers drawn from its liquid crystal solution (41), this process is not suitable for assembling mesoscale structures on a substrate to form a continuous film.

1.4 Functional Properties Arising from Incorporation of Nanoparticles

A list of functional properties of major interest to this dissertation is discussed here.

1.4.1. Glass Transition Temperature of Polymers

Previous studies of polymer thin films have shown that the reduction of thin film thickness results in significant shifting in T_g , depending on the nature of surface interactions (54, 55). Multiple theories have been proposed to explain this phenomenon. Some researchers support the idea that a polymer film is composed of multiple layers exhibiting different glass transition temperatures (55-58). Others have suggested that glass transition is related to dynamic heterogeneities in the polymer (59-62). Yet others have attempted to explain this phenomenon using memory effects in the viscoelastic eigenmodes (63) or intermolecular coupling of polymer chains (64).

Polymer nanocomposites (PNCs) reportedly show a T_g dependence on nanofiller content. Researchers have sought to explain this phenomenon by assuming that the confinement effect between nanoparticles affects T_g much as a polymer thin film is affected when sandwiched between two substrates (65, 66). Rittigstein *et al.* (65) reported that polymer thin films can serve as good model systems for PNCs, while Bansal *et al.* (66) has claimed quantitative equivalence in the T_g behavior for both forms of polymer. However, results have shown that nanofillers can affect glass transition beyond what is expected via polymer chain confinement. PNCs can show significant changes in T_g even when the interparticle distance, h_p is greater than the size of the polymer ($h_p > 2R_g$, R_g = radius of gyration) and chain relaxation time is not affected by the filler (67, 68). According to one report, C₆₀ particles can affect polymer segmental

dynamics at the particle surface in the nanosecond time scale (69), which is much lower than typical chain relaxation time scales. The general explanation to this is the existence of local pockets of heterogeneity that can percolate throughout the matrix at T_g , according to a model recently proposed by Long and Lequeux (60). A relevant question is whether PNCs can be described by the same equations governing glass transition behavior of polymer thin films. As the use of nanofillers in polymers grows in importance, an accurate physical model of PNCs is necessary to design and engineer new PNCs with desirable thermophysical properties.

1.4.2. Photonic Crystals

In Nature, reflectin nanoplatelets are an essential component in the color adaptive ability of cephalopods, which serves as a technique to camouflage against predators and signaling/communication tool between animals. The reflectin form nanoplatelet stacks within iridophores that reflect light by multilayer reflection and changes its wavelength in response to biological stimuli (70, 71). In the synthetic world, iridescence has been observed in solutions of surfactant molecules and inorganic nanoplatelets in the presence of highly ordered mesophases. Bragg reflection in the visible wavelengths occurs as surfactant bilayers or inorganic nanoplatelets form periodic smectic/lamellar structures with interlamellar spacings on the order of 200 nm (72-74), which is perceived as iridescence. Thus, the occurrence of iridescence is an indication that light is interacting with a material due to its photonic structure (75-77).

Creating photonic structures out of 2D crystal materials (vide supra) gives rise to the potential of coupling the intrinsic properties of these materials with the interaction of

light. The assembly of photonic structures out of colloidal particles typically requires a delicate balance of long-range repulsive forces and short-range attractive forces, *i.e.*, van der Waals forces. In aqueous dispersions, long-range interaction is moderated by the electrical double layer formed by the ionization of dissolved charge carriers. Practical methods of fabricating and processing device components often involve the use of organic solvents, which in the case of nonpolar solvents, such a long-range electrostatic repulsion is nonexistent. To overcome this limitation, the addition of charge control agents or surfactants can result in nanosized reverse micelles that interact *via* electrostatic repulsions that can have Debye screening lengths κ^{-1} up to 0.2–1.4 μm (78). This approach was successfully utilized to create magnetically tunable photonic crystals comprising of $\text{Fe}_3\text{O}_4/\text{SiO}_2$ nanoparticles, where magnetism provides the attractive force. In this case, a variable magnetic field can be used to manipulate the interparticle distance leading to Bragg reflections at different wavelengths (79).

Assembling 2D crystals to form photonic crystals in solution can be achieved *via* several methods. Surfactant molecules may form lamellar phases with the careful control of concentration. Strong electrostatic repulsion will result in interlayer spacings approaching visible wavelengths in a dilute solution. This phenomenon was observed in dilute aqueous solutions of alkylsuccinic acids by Satoh and Tsujii and decyldimethylamine oxide in the presence of small amounts of cosurfactants and hydrocarbon by Hoffmann *et al* (72, 74). Inorganic nanoplatelets are typically large monolayer sheets, often taking hexagonal form, with high D/t ratios (D = diameter, t = thickness) which can also form mesomorphic lamellar phases in aqueous dispersions.

This was first observed in $\text{H}_3\text{Sb}_3\text{P}_2\text{O}_{14}$ nanosheets by Gabriel *et al* (37). Iridescence appears as water swelled the solid gel of this material and increased interlamellar spacing. Color shifted from blue to red as more water molecules inserted between the nanosheets when concentration of the nanosheets was reduced.

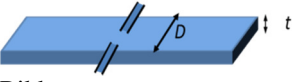




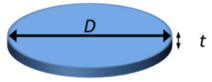
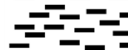
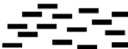
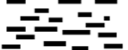
Despite its effectiveness, the formation of photonic crystals in aqueous solutions presents some disadvantages. Usually, a very low ionic concentration is necessary to maximize the Debye screening length, requiring a very thorough deionization of water. Furthermore, modifying 2D crystals in an aqueous solution with hydrophobic or water-sensitive molecules can be difficult or impossible, which are reasons why organic solutions can be very useful. Sterically-stabilized inorganic nanoplatelets dispersed in nonpolar solvents have been observed to undergo isotropic to nematic to columnar phase transitions typical of highly anisotropic mesogens (80-83). At very high concentrations (volume fraction $\phi > 0.50$), iridescence has been observed due to the formation of hexagonal columnar phases with lattice spacings of about 250 nm (80). Only recently, it was reported that gibbsite nanoplatelets suspended in dimethyl sulfoxide (DMSO), a polar aprotic solvent, forms a smectic B phase where the nanoplatelets are organized in a hexagonal order within each lamella (38). Strong electrostatic repulsion due to the charges on each nanoplatelet in a low-ionic strength solution enables the layers to maintain a large distance up to 125 nm. Interestingly, iridescence was not reported, presumably because the interlamellar distance was not sufficiently large to observe Bragg reflection in the visible wavelengths (we estimate that for DMSO, a d -spacing of

135 nm is required for iridescence in violet, based on the approximation $d = \lambda_{max}/2\eta$, where λ_{max} is the peak reflectance and η is the refractive index, see Platz *et al.* (72)).

1.4.3. Gas Barrier Films

Theoretical models of gas permeability in polymers filled with inorganic particles have been investigated as early as 1967 by Nielsen (84). The Nielsen model has been criticized for ignoring the geometric factor of the fillers, although it is widely accepted as giving fairly close results of filled polymers in the dilute regime. In the dilute regime $\alpha\phi \ll 1$, filler particles are spread far apart with little overlapping. Since then more sophisticated models have been proposed by Cussler *et al.* (85, 86), Fredrickson and Bicerano (87) and Gusev and Lusti (88) to account for increasingly higher concentrations of fillers in the semi-dilute regime, where $\alpha\phi \gg 1$, $\phi \ll 1$. The Cussler models (85) assume two-dimensional, ideal periodic arrays of ribbons to yield equations of the form $P/P_0 = [1+(\mu^{1/4} \alpha^2 \phi^2)/(1-\phi)]$, where μ is a geometric factor. For an ideal array of regular sized flakes, $\mu = 1$. According to the derivations of Fredrickson and Bicerano (87), $\mu = \pi^2/16\ln^2(\alpha/2)$, giving rise to the modified Cussler-Aris model when this value is employed. The modified Cussler-Aris model gives reasonably good predictions in the semidilute regime where there is strong overlapping of fillers. The Fredrickson-Bicerano model is a more sophisticated approximation that collapses to the Nielsen or Cussler-Aris model at certain limits. The Gusev-Lusti model is computationally derived from a finite-element model and is considered to be closer to the real performance of a polydisperse array of isolated plates in an isotropic matrix. A list of the permeability models mentioned above is summarized in Table 1.1.

Early attempts at producing gas barrier polymers filled with clay yielded improvements with some degree of success (89) with an order of magnitude reduction in permeability commonly reported (90, 91). It has been found that several characteristics pertaining to the filler is important to achieve low permeability, namely large aspect ratios, good compatibility with matrix, good exfoliation and highly oriented. In recent years, extremely low permeabilities have been reported in epoxy-clay fabrics (92) and layer-by-layer (*LbL*) assembled films (93, 94). *LbL* assembly of clay 2D crystals/polymers has been studied as a method to assemble highly oriented nanoplatelets in a thin polymer film onto flat (95) and irregular surfaces (96, 97), resulting in highly anisotropic ionic conductivities (95), excellent gas barrier property (94) and are being evaluated as flame retardants for textiles (97). The *LbL* process is highly efficacious, but it requires each layer of clay and polymer to be deposited individually requiring many iterations to build up the films with the desired properties. A variant of this technique improves manufacturing efficiency by iterative spraying of individual layers to form the films (96, 98). Due to the use of hydrophilic polyelectrolytes, the *LbL* films are particularly sensitive to moisture. Increase in permeability can be as much as 0.2 cc mm/ m² day atm or larger at high humidity levels (93, 94). It should be noted that even though these assemblies of clay 2D crystals exhibit orientation conformal to the substrate, they have not been shown to demonstrate long-range positional order.

Model	Filler Geometry	Flake Size, Array Type	Model Dimension	Equation*
Nielsen	Ribbon 	Monodisperse, Regular Array 	2D	$\frac{P}{P_0} = \frac{1}{1 + \frac{\alpha}{2}\phi}$
Ideal Cussler Regular Array	Ribbon	Monodisperse, Regular Array 	2D	$\frac{P}{P_0} = \left(1 + \frac{1/4 \alpha^2 \phi^2}{1 - \phi}\right)^{-1}$
Cussler Random Array Monodisperse Flakes	Ribbon	Monodisperse, Random Array 	2D	$\frac{P}{P_0} = \frac{1 - \phi}{[1 + \frac{\alpha}{3}\phi]^2}$
Cussler Random Array Polydisperse Flakes	Ribbon	Polydisperse, Random Array 	2D	$\frac{P}{P_0} = \frac{1 - \phi}{\left[1 + \left(\frac{\sigma}{\bar{D}}\right)^2\right]^2 \left[1 + \frac{\alpha}{3}\phi\right]^2}$
Modified Cussler-Aris	Disc 	Monodisperse, Random Array 	3D	$\frac{P}{P_0} = \left(1 + \mu \frac{1/4 \alpha^2 \phi^2}{1 - \phi}\right)^{-1}$ $\mu = \pi 2 / 16 \ln 2 \frac{\alpha}{2}$
Fredrickson-Bicerano	Disc	Monodisperse, Random Array 	3D	$\frac{P}{P_0} = \frac{(2 + x)^2}{4(1 + x + 0.1245x^2)^2}$ $x = \pi \alpha \phi / [2 \ln(\alpha/2)]$
Gusev-Lusti	Disc	Polydisperse, Random Array 	3D	$\frac{P}{P_0} = e^{-(\frac{\alpha \phi}{3.47})^{0.71}}$

* $\alpha = D/t$, $\sigma = \text{standard deviation}$, $\bar{D} = \text{mean value of } D$

Table 1.1 List of permeability models for filled polymer systems.

CHAPTER II

STABLE DISPERSIONS OF NANOPARTICLES TETHERED WITH SHORT, DENSE AND POLYDISPERSE BRUSHES IN POLY(METHYL METHACRYLATE)*

2.1 Introduction

Despite being such a well-studied field, an explosion of polymer brush–nanoparticles being used in technological applications has yet to be seen, with one notable exception of nylon–clay nanohybrids (99, 100). A few reasons may be suggested to explain such paucity of diverse applications; complex synthesis, specificity of surfactant molecules, limited applicability of synthesis methods for different polymer/nanoparticle systems, etc. One of the most important limiting factors is the lack of a synthesis method that can be adapted easily to commonly used polymer processing techniques, most notably melt-processing. The success of the nylon–clay nanohybrids can in huge part be attributed to the melt-processability of the material. The primary objective of this chapter is thus to present a synthesis method that is generally applicable to diverse nanoparticle/polymer combinations and yields a product that is amenable to melt-processing methods. This means that the nanoparticle remains stable and finely dispersed during melt-processing without detrimental effects to its functional properties. A corollary to the aforesaid goal is demonstrating that the nanocomposites thus fabricated exhibit multiple new functionalities as a result of the fine dispersion of inorganic nanoparticles.

*Reprinted by permission of John Wiley and Sons, Inc. from “Synthesis and Fabrication of Multifunctional Nanocomposites: Stable Dispersions of Nanoparticles Tethered with Short, Dense and Polydisperse Polymer Brushes in Poly(methyl methacrylate)” by Minhao Wong *et al.* 2012, *Adv. Funct. Mater.* 22, 3614–3624. Copyright 2012, WILEY-VCH Verlag GmbH & Co. KGaA, Weinheim. <http://onlinelibrary.wiley.com/doi/10.1002/adfm.201200083/full>

The mechanisms that allow the oligomer brush tethered zinc oxide (ZnO) nanoparticles to maintain their dispersion in the melt phase will also be discussed in detail. ZnO is a wide bandgap semiconductor which has a high-exciton binding energy of 60 meV at room temperature, making it an attractive material for optoelectronic devices. Nanoparticles of ZnO smaller than 10 nm in size exhibit the quantum confinement effect. This allows the bandgap of ZnO to be tuned by controlling the size of the nanoparticle. Nanoparticles that show this property are also called quantum dots (QDs). Spherical ZnO QDs of a very fine diameter of 5 nm can be easily produced by the hydrolysis of a methanol solution of zinc acetate dihydrate (101). This makes it a convenient material to be used for the purpose of this research.

A hybrid material that remains stable under repeated thermal processing steps without any signs of surface segregation have been prepared. Since the QDs are covered with grafted PMMA chains, this is essentially an athermal polymer mixture. Conditions for the stable dispersion of nanoparticles in athermal polymer mixtures have been reported elsewhere (102). A necessary condition for stability is that the nanoparticle diameter must be less than the radius of gyration of the host polymer. The ZnO QDs used in this study are appropriately sized to satisfy this condition.

2.2 Materials and Methods

2.2.1 *Materials for Synthesis*

N,N – dimethylformamide (DMF), methanol, and toluene were special grade chemicals purchased from Wako Chemicals. 2,2'-azobisisobutyronitrile (AIBN) and methyl

methacrylate (MMA) with 0.005% hydroquinone were Wako special grade chemicals from Wako Chemicals. Zinc acetate dihydrate was special grade and potassium hydroxide was semiconductor grade chemicals purchased from Nacalai Tesque. 3-(Trimethoxysilyl)propyl methacrylate (TSMA) 98% was purchased from Aldrich. Poly(methyl methacrylate) (PMMA) was obtained from Sumitomo Chemicals. Sumipex was analyzed by gel-permeation chromatography using standard polystyrene reference. Number average molecular weight (M_n), weight average molecular weight (M_w) and polydispersity index were found to be 65 kgmol⁻¹, 145 kgmol⁻¹ and 2.241, respectively. MMA was purified through an activated alumina column to remove the inhibitor hydroquinone. All other chemicals were used as received.

2.2.2 Materials for Elemental Analysis

Nitric acid was electronic grade, sulfuric acid and hydrochloric acid were Ultrapur grade chemicals and potassium carbonate and sodium carbonate were special grade chemicals purchased from Kanto Chemicals.

2.2.3 Preparation of PMMA-grafted ZnO Nanoparticles

The synthesis and modification of ZnO nanoparticles with TSMA and the subsequent grafting of PMMA is described in detail in Chapter III (103). In brief, a methanol solution of TSMA-ZnO was transferred into DMF, followed by polymerization of MMA with AIBN as initiator under nitrogen atmosphere. Polymerization was carried out for 5 hours at 85°C and monomer conversion was monitored to ensure completion of the reaction. The nanoparticles were recovered by precipitation in cold methanol.

Purification was conducted by dissolving the nanoparticles in toluene and re-precipitation in cold methanol.

2.2.4 Melt-blending ZnO/PMMA Nanocomposites

The PMMA-grafted ZnO batches prepared previously were blended with commercial PMMA to form blended nanocomposite/polymer alloys. Melt-blending was done using a Labo Plastomill from Toyoseiki Co. Ltd., which is a batch-mixer used for homogenizing polymer blends. The ratios of commercial PMMA and PMMA-grafted ZnO, and processing conditions used for preparing each nanocomposite are listed in Table 2.1. The blended polymers are subsequently injection-molded into bars of dimensions 63.5 mm × 12.7 mm × 2 mm using a ThermoHaake Injection Molding Unit.

Batch no.	ZnO wt %	Si wt %	PMMA-g-ZnO weight /g	PMMA weight /g	Blending Temperature /°C
1	18.11	0.28	-	-	-
1	9.87	0.15	25.9	19.2	200
1	4.75	0.07	13.0	32.6	200
1	1.04	0.02	2.7	42.6	200
2	15.56	0.24	-	-	-
2	11.95	0.19	45.8	14.2	180
2	6.60	0.10	25.0	35.0	180
2	1.62	0.03	6.3	53.8	180

Table 2.1 Processing condition in blending the PMMA-g-ZnO with PMMA. Nanocomposite blends and virgin PMMA were injection-molded at 235 °C and 255 °C, respectively.

2.2.5 Annealing of ZnO/PMMA Nanocomposites

Injection molded nanocomposites were annealed under vacuum for 5 days at 160°C. The annealed samples were hot-pressed to form 0.20 mm thick sheets and embedded in epoxy for the preparation of thin sections for TEM observation.

2.3 Characterization

2.3.1 Procedure for Cleaving Grafted Oligomer from Nanoparticles

PMMA-grafted ZnO (100 mg) was dissolved in chloroform (4 mL) and Aliquat 336 (10 mg) phase transfer catalyst (a quarternary ammonium salt) was added. 49% HF acid (2 mL) was added to the chloroform solution and the mixture was stirred overnight. Stirring was stopped to allow phase separation, after which the chloroform phase was siphoned off with a polypropylene pipette. The chloroform phase was neutralized by adding saturated sodium bicarbonate solution (4 mL) and shaken vigorously. This procedure was carried out twice, followed by washing with deionized water to remove any remaining ions. The result is a clear solution (5 mL) with a concentration of about 0.017 g mL⁻¹ of solute. The solute contains a majority of cleaved PMMA and the remaining Aliquat 336.

2.3.2 NMR Characterization of PMMA-grafted ZnO

The ²⁹Si solid-state NMR spectra were measured on a Bruker AVANCE 400 spectrometer operating at 79.49 MHz. The ²⁹Si CP/MAS (Cross Polarization with Magic Angle Spinning) experiments were carried out at MAS rates of 4 kHz using densely packed powders of the materials in 7 mm ZrO₂ rotors. The ¹H $\pi/2$ pulse was 4.0 μ s and TPPM (two-pulse phase modulation) decoupling was applied during the acquisition. The

Hartmann-Hahn matching condition was optimized at a rotational speed of 4 kHz using polycrystalline tetrakis(trimethylsilyl)silane, which also served as the external chemical shift standard. All spectra were measured with a contact time of 8.0 ms and a relaxation delay of 4 s, and 11284 and 5946 FIDs (Free Induction Decays) were accumulated for Batch 1 and Batch 2, respectively. An exponential multiplication line broadening factor of 100 Hz was applied for the processing of the spectra.

2.3.3 GPC Determination of Molecular Weight of Grafted Oligomers

Gel permeation chromatography (GPC) was performed on an EcoSEC HLC-8320GPC (TOSOH Bioscience, LLC) equipped with a differential refractometer and UV detector with two TSKgel SuperHM-M 3 μm , 150 \times 6.0 mm columns connected in series, using the ECOsec Control (version 1.04, TOSOH Bioscience, LLC) software. The instrument was operated at 40 $^{\circ}\text{C}$ with CHCl_3 as the eluent (flow rate set to 0.60 mLmin^{-1}). Polymer solutions were prepared at a known concentration ($\sim 2 \text{ mgmL}^{-1}$) and an injection volume of 10 μL was used. The data was analyzed with ECOsec Analysis (version 1.04, TOSOH Bioscience, LLC) software with a system calibration curve generated from plotting molecular weight as a function of retention time for a series of broad polydispersity polystyrene standards.

2.3.4 Elemental Analysis of PMMA/ ZnO Nanocomposites

The zinc oxide and silicon contents of the nanocomposites were determined using Inductively Coupled Plasma Atomic Emission Spectroscopy (ICP-AES) using an ICPS-8100 unit from Shimadzu. The zinc content was first determined then multiplied by a factor of 1.245 (weight ratio of ZnO/Zn) to obtain the ZnO content. Determination of the

Zn and Si contents provides information about the amount of silane coupling agents attached to the ZnO surface. The preparation of analyte solutions for Zn and Si analysis were done separately. Analyte solutions for Zn analysis were prepared in a Teflon container using sulfuric acid and nitric acid with microwave digestion using a Milestone MLS –1200 MEGA microwave digestion unit. In the preparation of analyte solutions for Si analysis, nitric acid was added to the samples in a platinum crucible and charred on a hotplate, followed by alkaline fusion using potassium carbonate and sodium carbonate. Subsequent ashing was done in a muffle oven FM-48 from Yamato Scientific. Excess hydrochloric acid was added after ashing to neutralize the analyte solution.

2.3.5 Transmission Electron Microscopy (TEM) of ZnO/PMMA Nanocomposites

Transmission electron micrographs were obtained on a JEOL JEM–1200Ex and high resolution images were taken with a JEOL JEM 2010. TEM specimens were prepared by cutting nanocomposite samples from the injection-molded bars and ultrathin sections were obtained using an ultramicrotome from Leica Microsystems (EM UC6/FC6).

2.3.6 UV-Vis Spectrophotometry of ZnO/PMMA Nanocomposites

UV-Visible transmission spectra were recorded using the Hitachi U-4100 UV-Vis-NIR spectrophotometer. Standalone film samples were prepared by compression molding at 180°C and measured for characterizing their transmission properties. Nanocomposites were sandwiched between heated 1 mm thick glass slides and pressed to form a clear film with a thickness of ~0.1 mm. The sandwiched nanocomposites were analyzed with a Shimadzu UV-3600 UV-Vis-NIR spectrophotometer for the absorption spectra. The bandgap energy was determined by characterizing the knee of the absorption edge by

taking the intersection of two straight lines extended from the absorption trace before and after the knee. The energy shift was calculated by determining $E_g - E_{g0}$, where E_{g0} and E_g are the bandgap energies of PMMA-g-ZnO dissolved in chloroform and melt-blended in the nanocomposite, respectively. The average measurement of two samples was plotted in the $E_g - E_{g0}$ plot.

2.3.7 Refractive Index of ZnO/PMMA Nanocomposites

The refractive index was measured by a prism coupler (Metricon Model 2010) at three wavelengths, 404 nm, 594 nm and 825 nm. Cauchy curve fitting was performed to obtain the refractive index curve from 400 nm to 825 nm. The refractive index at 589.3 nm (sodium D-line) was read from this curve and reported for all samples.

2.3.8 Dynamic Light Scattering (DLS) of PMMA-grafted ZnO

Dynamic light scattering (DLS) measurements were conducted using Delsa Nano C (Beckman Coulter, Inc., Fullerton, CA) equipped with a laser diode operating at 658 nm. Size measurements were made in acetone (refractive index = 1.3575, viscosity = 0.3160 cP at 25 ± 1 °C). Scattered light was detected at 165° angle and analyzed using a log correlator over 70 accumulations for a 0.7 mL of sample in a glass size cell (0.9 mL capacity). The calculation of the particle size distribution and distribution averages was performed using CONTIN particle size distribution analysis routines. The peak average of histograms from intensity weighted distributions and the z-average diameter out of 70 accumulations was reported as the average diameter of the particles. 5 aliquots of 10^{-3} gmL⁻¹ solution prepared from a 10^{-2} gmL⁻¹ solution of PMMA-grafted ZnO dispersed in acetone were measured to obtain an average value from 5 solutions.

2.3.9 Atomic Force Microscopy (AFM) of PMMA-grafted ZnO

Tapping-mode atomic force microscopy was carried out by a Digital Instruments Nanoscope AFM/STM system comprising a Nanoscope II and system controller fitted to a MultiMode TM scanhead. The image was acquired in air using a SuperSharpSilicon SSS-NCL-10 probe (Nanoworld Innovative Technologies; tip radius, cone half angle, nominal force constant and resonance frequency are <2 nm, 10°, 48 Nm⁻¹ and 190 kHz, respectively). Highly diluted solutions of nanoparticles were dropped onto a Si wafer cleaned previously by piranha solution. The samples were dried for 3 days at 70°C before scanning. The lateral particle size was measured and used in the statistical analysis of brush height. To account for tip convolution, which causes a broadening of the lateral dimensions of the scanned particles, a correction was applied using the following Equation 2-1, which is valid when the tip radius is small compared to the particle size,

$$r_c = r \left[\cos \theta + \sqrt{\cos^2 \theta + (1 + \sin \theta) \left(\frac{\tan \theta}{\cos \theta} - 1 \right) + \tan^2 \theta} \right] \quad 2-1$$

where r_c is the radius of the measured particle size, r is the true radius of the particle and θ is the cone half angle.

2.4 Oligomer-Grafted Nanoparticles

PMMA-grafted ZnO nanoparticles were prepared *via* a free radical copolymerization process according to the reaction scheme shown in Figure 2.1a. The ZnO nanoparticles are synthesized, followed by silanization. The nature of the silane anchored to the ZnO surface is probed using ²⁹Si solid-state CP/MAS NMR (104). The identification of the silane-ZnO bonding mode follows the classification by Veeman *et al.* (105, 106), which

is illustrated in Figure 2.1b. The silane bonding type T^0 can be unequivocally assigned to both samples based on the peaks at -34.1 ppm and -33.5 ppm for Batch 1 and Batch 2, respectively (Figure 2.1c). The absence of any peaks in the area of -60 to -68 ppm rules out T^2 surface-bonding (106) and Q^3 species (105), and therewith the formation of multiple cross-linked silane layers on the surface, or a gel process taking place in solution. Furthermore, the absence of any signals in the region from -42 to -46 ppm, which would indicate T^1 surface-bound species, proves unequivocally that the silane molecules do not cross-link on the surface.

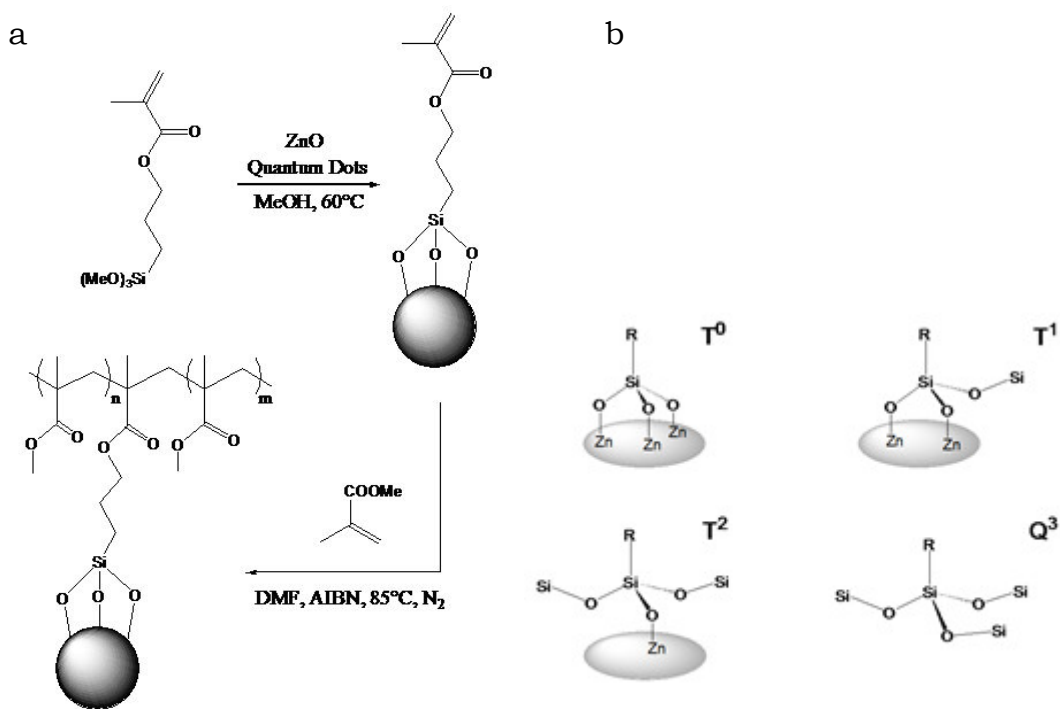


Figure 2.1 (a) Reaction scheme for the preparation of PMMA-grafted ZnO. (b) Classification of silane bonding types T^0 , T^1 , T^2 , and Q^3 . [23, 24] (c) The ^{29}Si solid-state NMR spectra of two PMMA-grafted ZnO batches. The ^{29}Si signals appear at chemical shifts of $\delta = -34.1$ and $\delta = -33.5$ ppm for Batch 1 and Batch 2, respectively.

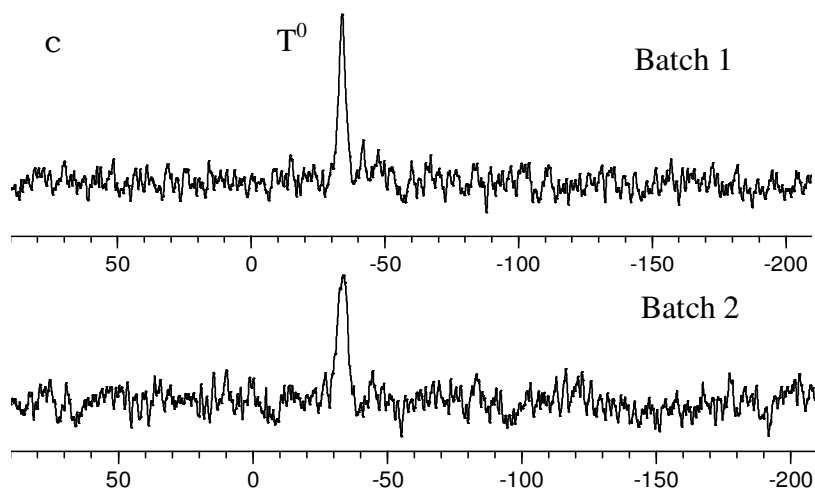


Figure 2.1 Continued.

Therefore, we conclude that all silane molecules fall into the T^0 category and are exclusively bound to the ZnO surface by three Si-O-Zn bridges. The silanized ZnO nanoparticles were then copolymerized in the presence of methyl methacrylate (MMA) monomer in *N,N*-dimethylformamide (DMF) solution in order to form PMMA-grafted ZnO nanoparticles.

Transmission electron microscopy (Figure 2.2a) shows that the nanoparticles exhibit a narrow size distribution of 3.4 ± 0.8 nm in diameter (107) according to the histogram of particle diameters from a total of 150 nanoparticles measured over several TEM images (Figure 2.2b). In contrast to the more common method of grafting polymers using surface- initiated polymerization techniques (108-111), this approach allows us to tether polydisperse brushes with a polydispersity index (PDI) ≈ 2 , closely matching the PDI of the matrix polymer used in subsequent melt-blending. In fact, a bimodal distribution is detected (Figure 2.3), where the major peak is found to have $M_n = 9.5 \text{ kgmol}^{-1}$, $M_w = 21 \text{ kgmol}^{-1}$, PDI = 2.2 and the minor peak is found to have $M_n = 0.5$

kgmol^{-1} , $M_w = 0.6 \text{ kgmol}^{-1}$, $\text{PDI} = 1.2$. By integration of the area under the peaks, the mass ratio of major to minor population is found to be 16 : 1. Similar copolymerization procedures have been utilized to synthesize well-dispersed nanocomposites with high nanoparticle concentrations (112-115). Nevertheless, a major drawback of this method has been that the nanocomposites synthesized are not redispersible in a solvent or polymer melt due to the formation of cross-links with the nanoparticles acting as cross-linking nodes during polymerization. This limitation has now been overcome by controlling the concentration of the nanoparticles in solution to prevent the formation of cross-links.

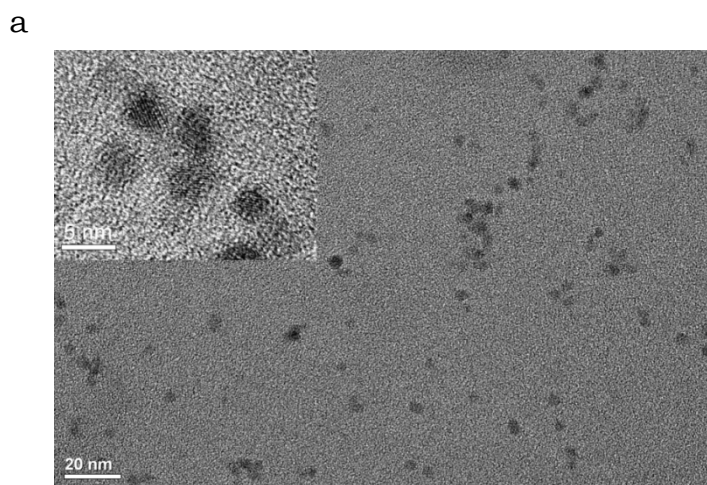


Figure 2.2 (a) TEM image of PMMA-grafted ZnO dispersed by melt blending in neat PMMA, (inset) HRTEM of PMMA-grafted quantum dots. (b) Histogram of particle diameters of 150 nanoparticles yielding an average diameter of $3.4 \pm 0.8 \text{ nm}$. (c) Photographic image of a nanocomposite sheet (thickness = 0.20 mm) formed by melt blending of PMMA-grafted ZnO with neat PMMA followed by annealing, ZnO = 9.81 % by weight, demonstrating the quality of transparency with no preferential absorption of a particular color in the visible range.

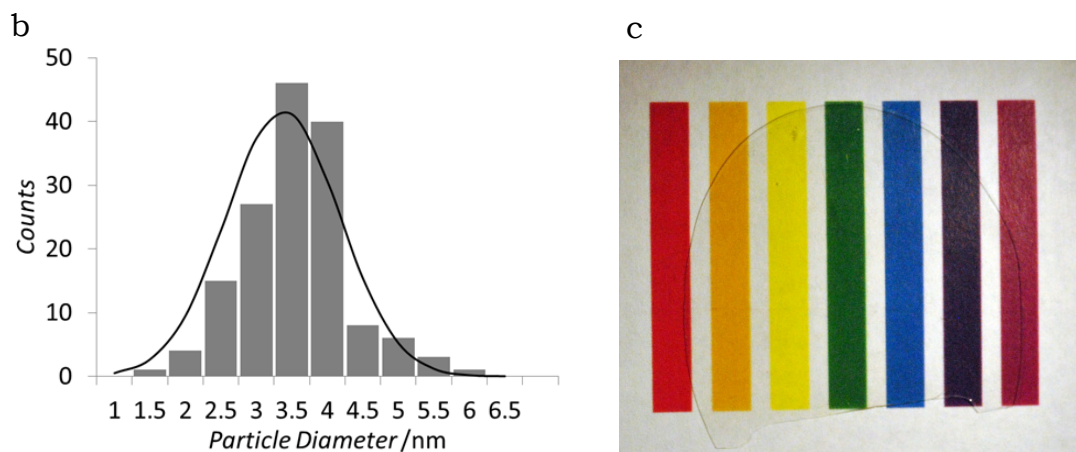


Figure 2.2 Continued.

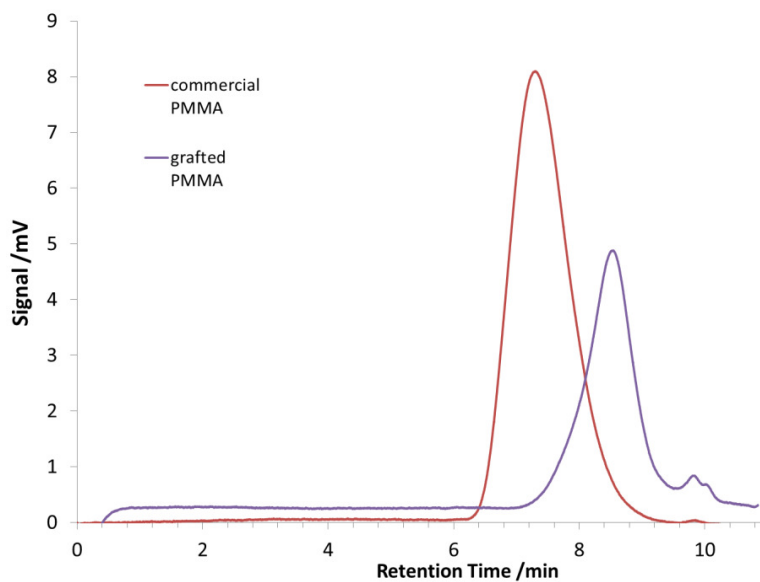


Figure 2.3 Gel permeation chromatography (GPC) trace of commercial and grafted PMMA. The major peak is found to have $M_n = 9.5 \text{ kgmol}^{-1}$, $M_w = 21 \text{ kgmol}^{-1}$, $\text{PDI} = 2.2$ and the minor peak is found to have $M_n = 0.5 \text{ kgmol}^{-1}$, $M_w = 0.6 \text{ kgmol}^{-1}$, $\text{PDI} = 1.2$. By integration of the area under the peaks the mass ratio of major to minor population is found to be 16 : 1.

A series of experiments was conducted to determine the optimal conditions for polymerization in the presence of silanized ZnO. The experimental conditions are presented in Table 2.2. Reaction temperature, ZnO concentration, ZnO/MMA ratio and silane species were varied. Monomer conversion during polymerization was measured by weighing the solid content of the samples. 1 mL of reaction solution was taken at 30 minute intervals and placed in an aluminum pan. The solution was dried at 130°C for one hour in an oven; the solid residue of the solution was weighed to obtain the change in solid content with the polymerization time. The maximal monomer conversion of the polymerization for the silanized ZnO in DMF is around 88%, while polymerization of MMA without ZnO yields only 47% conversion. Figure 2.4 shows the conversion during polymerization. The reason for the observed increase in conversion is unclear; however, this result is consistent with the report that the rate of polymerization of MMA, when mediated by RAFT agents anchored to silica nanoparticles, was much higher than the rate of polymerization in the absence of nanoparticles (110).

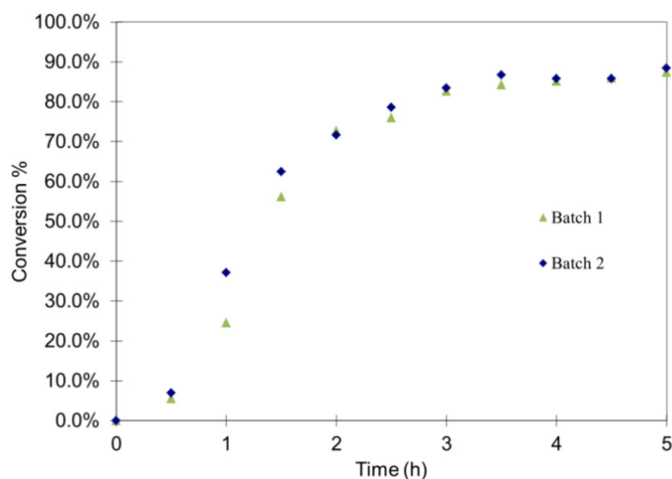


Figure 2.4 Monomer conversion during radical copolymerization of MMA and silanized ZnO.

On the basis of the maximum conversion of monomer (Table 2.2), the higher temperature reactions 6 and 7 were determined as optimal. Products from reactions 6 and 7 were used in the subsequent preparation of nanocomposites in this paper and identified as Batch 1 and Batch 2, respectively. We found that a higher concentration of ZnO (reaction 3) resulted in a gelatinous solid that was neither redispersible in toluene nor melt-processable. This suggests that cross-linking of the polymer chains occurred during polymerization with the densely grafted ZnO acting as nodes. Increasing ZnO concentration relative to monomer concentration (reaction 5) depressed the maximum conversion of monomer, indicating that the ZnO/MMA ratio exerts a strong effect on the kinetics of polymerization. Finally, ZnO functionalized by phenyltrimethoxysilane (PTMS), which lacked a vinyl group, was used instead of 3-(trimethoxysilyl)propyl methacrylate (TSMA) in reaction 2. Surprisingly, the resulting product was redispersible in toluene yielding a transparent solution, despite the absence of covalent linkage between polymer and ZnO. However, the dried product did not form a transparent nanocomposite after melt-processing, due to the presence of aggregates in the polymer matrix, demonstrating that the grafting of the polymer through a covalent bond is necessary in achieving a fine dispersion of nanoparticles in the melt phase.

S/N	Silane [†]	Temp- eratur e (°C)	ZnO			MMA			ZnO/MMA			Total Volume of Reaction (mL)	Maximum Conversio n* (%)	Re- dispersible in toluene ?
			Conc. (% wt)	Conc. [M]	Conc. (% vol)	Conc. (% wt)	Conc. [M]	Conc. (% vol)	wt /wt	[M] / [M]	vol/vol			
1	T SMA	65	1.60	0.19	0.27	9.07	0.86	9.13	0.18	0.22	0.030	269	66.7	Yes
2	PTMS	65	1.60	0.19	0.27	9.07	0.86	9.14	0.18	0.22	0.030	269	64.9	Yes
3	T SMA	65	3.99	0.46	0.67	22.7	2.14	22.82	0.18	0.22	0.029	100	81.8	No
4	T SMA	85	1.61	0.19	0.27	9.10	0.86	9.14	0.18	0.22	0.030	215	76.8	Yes
5	T SMA	85	1.60	0.19	0.27	3.74	0.35	3.77	0.43	0.53	0.072	215	60.2	Yes
6	T SMA	85	1.80	0.21	0.30	9.12	0.86	9.19	0.20	0.24	0.033	1912	87.3	Yes
7	T SMA	85	1.80	0.21	0.30	9.11	0.86	9.19	0.20	0.24	0.033	2256	88.4	Yes

Table 2.2 Experimental conditions for the grafting of PMMA to ZnO.

2.5 Fine, Stable Dispersion of Nanoparticles

The resultant polymer-grafted nanoparticles are fully melt-blendable and resistant to aggregation even with extended annealing above the glass transition temperature T_g . We were able to produce melt-blended nanocomposites that are highly transparent, as illustrated by a nanocomposite containing 9.87 wt% ZnO, formed into a 0.2 mm thick sheet, shown in Figure 2.2c. The transparent sheet showed no preferential absorption of color, resulting in a high quality, near colorless appearance. The nanocomposites exhibit surprising tunability of T_g , refractive index and energy bandgap. To the best of our knowledge, this is the first example of a melt-blendable nanocomposite exhibiting such multifunctional properties. Nanocomposites with varying ZnO concentrations are prepared by melt-blending proportional amounts of PMMA-grafted ZnO with a commercial grade PMMA ($M_n = 65 \text{ kgmol}^{-1}$, $M_w = 146 \text{ kgmol}^{-1}$, PDI = 2.2) in a batchmixer, after which the melt-blended nanocomposites are injection molded into bars. The dispersion stability is investigated by comparing the dispersion of the nanofillers of injection molded nanocomposites with nanocomposites that are subsequently annealed for 5 days at 160°C, which is well above the T_g values of the nanocomposites.

The state of the dispersion is monitored using transmission electron microscopy (TEM), UV-Vis spectroscopy, refractive index analysis using a prism coupler, and T_g characterization by dynamic mechanical analysis (DMA) and differential scanning calorimetry (DSC). From the TEM results (Figure 2.5), it is observed that the dispersion of the nanoparticles shows only little change before and after annealing. Significantly, in contrast to previous studies (26, 116, 117) we do not observe any aggregation, self-

assembly of nanoparticles into secondary structures or segregation of nanoparticles to a free surface after annealing. In the pre-annealed samples (Figure 2.5, left column), there appear to be clusters of ZnO nanoparticles distributed throughout, but detailed analysis reveals that the nanoparticles remain individually separated and the tunability of T_g does not seem to be affected. The linearity of the relation of T_g to ZnO concentration has been verified independently through DMA and DSC. This behavior is related to the physics of polymer thin films, where chain dynamics are altered as thickness of the films approaches nanoscale. It can be shown that the linearity of T_g can be described by the Long-Lequeux model, which postulates that dynamic regions of polymer chains determine glass transition behavior. Detailed arguments supporting this conclusion will be discussed in Chapter III and will not be repeated here. The electron micrographs of the annealed nanocomposites (Figure 2.5, right column) show that the nanoparticles remain well-dispersed throughout the matrix with an apparent improvement of homogeneity due to fewer occurrences of the clusters.

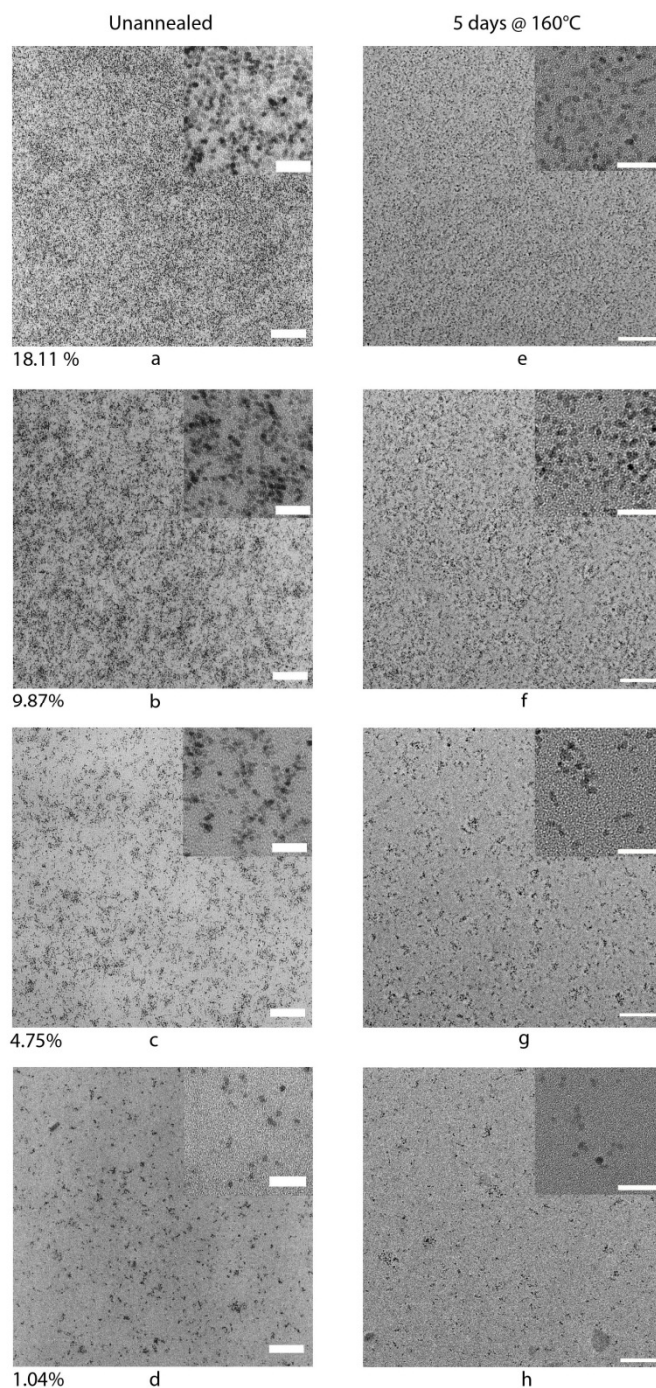


Figure 2.5 TEM images of unannealed (Batch 1) nanocomposites (left column) and nanocomposites annealed at 160°C for 5 days (right column). Brush polymer $M_n = 9.5 \text{ kgmol}^{-1}$, $M_w = 21 \text{ kgmol}^{-1}$, PDI = 2.2, matrix polymer $M_n = 65 \text{ kgmol}^{-1}$, $M_w = 146 \text{ kgmol}^{-1}$, PDI = 2.2. Scale bars represent 100 nm and 25 nm for the main and inset images, respectively. ZnO content is indicated at the bottom of the images in the left column.

2.5.1 Tunability of Energy Bandgap

UV-Vis spectroscopy (Figure 2.6a) of nanocomposites that were annealed at 160°C for 5 days and subsequently pressed into sheets (~0.20 mm thick) shows transmission levels close to neat PMMA (~90%). However, at higher ZnO loadings, weak absorption around 400 to 500 nm leads to a very slight yellowish tinged appearance of the nanocomposite. The nanocomposite sheets absorbed all wavelengths shorter than 370 nm. The dependence of the absorption wavelength of the nanocomposite on the quantum dot concentration is due to the quantum coupling of exciton states in closely spaced quantum dots. The formation of delocalized energy bands as the quantum dots approach each other lowers the energy of the radiation absorbed (118, 119), in effect decreasing the energy bandgap of the quantum dots. This phenomenon is clearly observed in the absorption spectra (Figure 2.6b) of our nanocomposites where the absorption edge red-shifts from 3.51 eV to 3.41 eV from lowest to highest ZnO concentration, respectively. PMMA-g-ZnO dispersed in chloroform is used as a model for isolated ZnO quantum dots. The absorption red-shifts of the nanocomposites are referenced to the absorption energy of isolated ZnO quantum dots and plotted against the interparticle distance h_p , which, surprisingly, showed a linear dependence of energy red-shift to h_p (Figure 2.6c). To obtain h_p , we consider that the QDs are homogeneously and randomly dispersed. We can relate the interparticle distance h_p to the nanoparticle volume fraction ϕ and nanoparticle radius a , by the following equation, $h_p = 2a[(\phi_0/\phi)^{1/3} - 1]$ where $\phi_0 = 0.64$, is the maximum volume fraction of a random disordered particle system (120). Although highly concentrated quantum dots in polymer matrices have been known to show red-

shifts in the energy absorbed, this is the first known report of such linear dependence (107, 121) and may be a result of the uniform dispersion. This explanation is consistent with the observation of homogeneous distribution of nanoparticles in the TEM images (Figure 2.5).

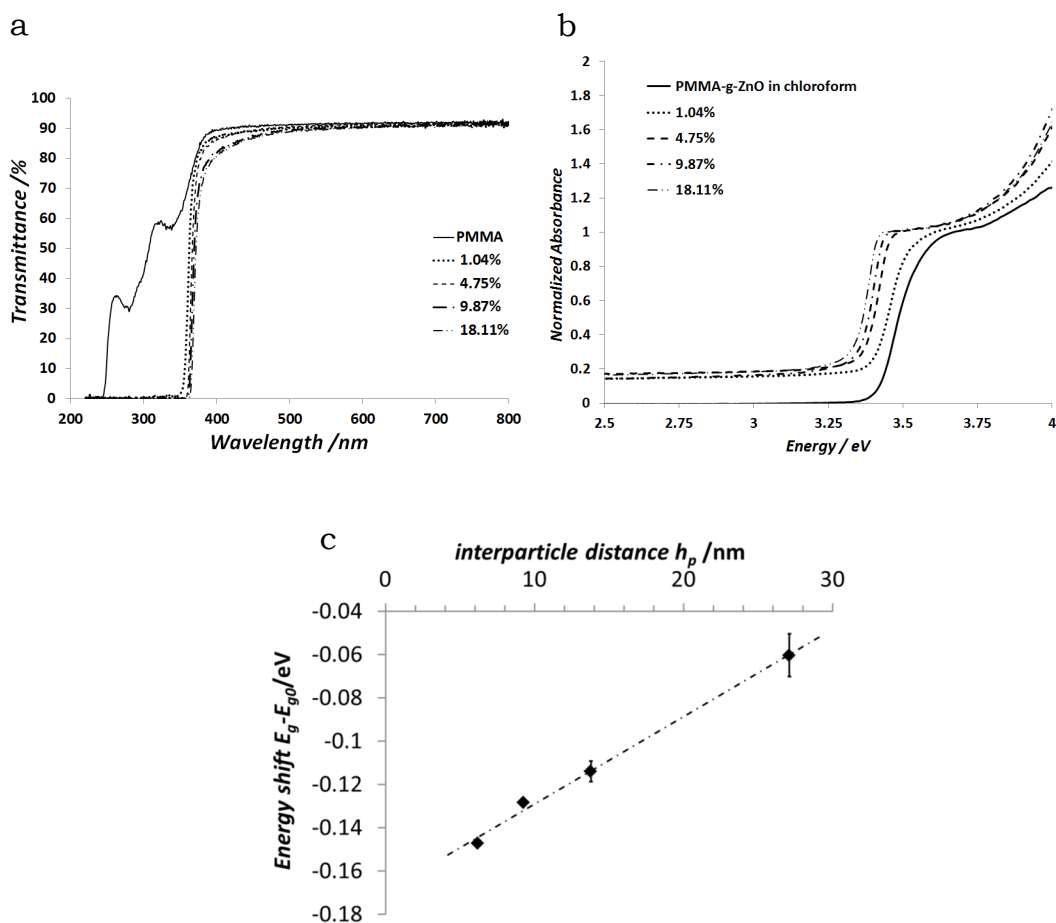


Figure 2.6 (a) UV-Vis transmission of annealed nanocomposite sheets at different ZnO loadings showing high transmission levels close to neat PMMA. The absorption edge red-shifts as ZnO concentration increases. (b) Normalized absorption spectra of nanocomposites compared to isolated PMMA-g-ZnO in chloroform solution. The absorption was normalized to the absorbance at the knee of the trace. (c) Magnitude of energy red-shift of ZnO increases linearly with shorter interparticle distance h_p . Interparticle distances (nm) are 27.1, 13.8, 9.3 and 6.2 for nanocomposites of 1.04%, 4.75%, 9.87% and 18.11% ZnO by weight, respectively.

2.5.2 Tunability of T_g

The nanocomposites showed a tunability of T_g when the ZnO content was varied; T_g , as measured by DSC, increased linearly with the ZnO concentration (figure on p.41). This phenomenon was reproducibly observed in two different batches of nanocomposites and also in the T_g measured by DMA. The T_g s of the nanocomposites were found to be a function of h_p , in excellent agreement with the Long-Lequeux model based on the percolation of slow dynamic domains. The presence of nanoparticles has been found to have a significant impact on T_g trend (65, 66), while linear T_g dependence has been observed only in the absence of particle aggregation (122, 123).

2.5.3 Tunability of Refractive Index

To obtain an accurate analysis of the refractive index, the volume fractions of all the components were considered. By plotting the ZnO weight against the reciprocal of the nanocomposite density, the slope of this graph can be used to evaluate the effective density of the silane in the nanocomposite. The procedure for determining silane density is as follows: The density of the nanocomposite was measured using a laboratory balance AB204-S (Mettler-Toledo) with a density measurement kit. A sample block of 5 mm × 5 mm × 2 mm was cut and weighed in air; the sample was weighed again in water. The density of the sample was calculated according to Archimedes' principle (Equation 2-2). Each data point was obtained as an average of two measurements.

$$\rho = \frac{W_A}{W_A - W_B}(\rho_0 - \rho_L) + \rho_L \quad 2-2$$

ρ = density of sample

W_A = weight of sample in air

W_B = weight of sample in water ρ_0 = density of water

ρ_L = density of air (0.0012 g/cm³)

One can reasonably assume that the grafted polymer has a density similar to PMMA, thus forming a three-component nanocomposite system of ZnO, silane and PMMA. The density of the nanocomposite ρ_T is related to the densities of PMMA ρ_{PMMA} , ZnO ρ_{ZnO} and silane ρ_{TSMA} , and weight fractions of ZnO w_{ZnO} and silane w_{TSMA} , according to the follow equation,

$$w_{ZnO} = \frac{\rho_{PMMA}}{Q\rho_T} - \frac{1}{Q} \quad 2-3$$

where β and Q are defined as

$$\beta \equiv \frac{w_{TSMA}}{w_{ZnO}}$$

$$Q \equiv \frac{\rho_{PMMA}}{\rho_{ZnO}} - 1 + \beta \left(\frac{\rho_{PMMA}}{\rho_{TSMA}} - 1 \right)$$

A graphical method (Figure 2.7) based on Equation 2-3 can be used to determine the density of the silane in the nanocomposite. The ZnO weight fraction w_{ZnO} , is plotted against the reciprocal of the nanocomposite density $1/\rho_T$, to obtain a straight line, the slope of which is equal to ρ_{PMMA}/Q . We assume that ZnO QDs have the same density as bulk ZnO, and because all other parameters are known, the value of ρ_{TSMA} is easily obtained. Table 2.3 shows that the density of the silane in the nanocomposite is approximately equal to the density of silane in the liquid state.

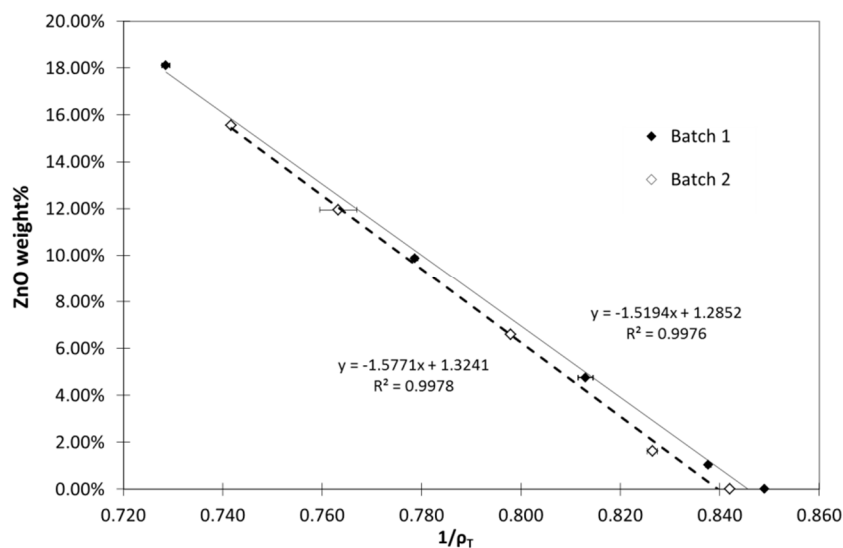


Figure 2.7 Graphical method for determining the density of silane. Error bars indicate standard deviation.

	Batch 1	Batch 2
ZnO density (assumed), ρ_{ZnO}	5.606 gcm ⁻³	5.606 gcm ⁻³
PMMA density, ρ_{PMMA}	1.178 gcm ⁻³	1.188 gcm ⁻³
β	0.137	0.136
Liquid silane density (Manufacturer data)	1.045 gcm ⁻³	1.045 gcm ⁻³
Surface modifier density (measured), ρ_{TSM}	1.094 gcm ⁻³	1.160 gcm ⁻³

Table 2.3 Densities of the components of PMMA-grafted ZnO

It was found that the effective density of the silane in Batch 1 and Batch 2 nanocomposites are 1.094 gcm⁻³ and 1.160 gcm⁻³, respectively. The difference in densities between the silane and PMMA (1.180 gcm⁻³) is less than 10%, thus justifying the assumption that the volume contribution from the silane is small and negligible. In Figure 2.8b (inset), the volume fraction of ZnO QDs is plotted against its weight

fraction. Subsequently, the refractive index of the nanocomposite is plotted against the ZnO volume fraction and compared with known physical models. The refractive indices of mixtures are described by the Lorentz-Lorenz formula (Equation 2-4) if the mixing occurs at the molecular level (124).

$$\left(\frac{\eta_o^2 - 1}{\eta_o^2 + 2}\right) = v_1 \left(\frac{\eta_1^2 - 1}{\eta_1^2 + 2}\right) + (1 - v_1) \left(\frac{\eta_2^2 - 1}{\eta_2^2 + 2}\right) \quad 2-4$$

where η_o , η_1 , and η_2 are the refractive indices for the nanocomposite, nanofiller and matrix polymer, respectively, and v_1 is the volume fraction of the nanofiller.

The refractive index of a mixture with mesoscale level mixing requires the use of other forms of effective medium theories to describe the contribution of nanosized inclusions in a host medium (125), of which the Maxwell-Garnett (Equation 2-5) and Bruggeman (Equation 2-6) theories are of particular relevance here.

The Maxwell-Garnett model is described by

$$\eta_o^2 = \eta_2^2 \left(1 + \frac{3v_1 \left(\frac{m^2 - 1}{m^2 + 2} \right)}{1 - v_1 \left(\frac{m^2 - 1}{m^2 + 2} \right)} \right) \quad 2-5$$

$$m = \frac{\eta_1}{\eta_2}$$

The Bruggeman model is described by

$$v_1 \left(\frac{\eta_1^2 - \eta_o^2}{\eta_1^2 + 2\eta_o^2} \right) + (1 - v_1) \left(\frac{\eta_2^2 - \eta_o^2}{\eta_2^2 + 2\eta_o^2} \right) = 0 \quad 2-6$$

The Maxwell-Garnett model assumes that monodispersed, nanosized spheres are dispersed in a host medium, while the Bruggeman theory describes polydispersed spheres and intermixing phases in a host medium. In the calculations of the refractive index of nanocomposites, the refractive index of bulk ZnO was taken as 2.021 at 589.3 nm (126), and we assumed that the refractive index of grafted silane is very similar to PMMA due to their similar chemical structures. Although the refractive index of the liquid silane (1.431) is significantly different (~4%, a large difference for refractive indices) compared to PMMA (1.4912), the absence of any true silane “liquid” in the nanocomposite and the grafting of the silane to PMMA chains should render its polarizability and therefore refractive index close to that of PMMA. The refractive index of the nanocomposite was found to increase linearly with the ZnO concentration (Figure 2.8b). The Lorentz-Lorenz formula consistently underestimates the measured refractive indices of the nanocomposites, suggesting that the nanoparticles have not achieved the level of homogeneity observed in other studies (127). By contrast, both the Maxwell-Garnett and Bruggeman theories were in excellent agreement with the experimental data. It is noteworthy that very close agreement between theory and experiment was achieved without any empirical adjustment. By comparing the predictions from different models, we see a measurable change in the refractive index with different degrees of dispersion of the nanoparticles. These results suggest that further studies of the impact of the

dispersion on the refractive index may yield a quantitative measure of the state of dispersion.

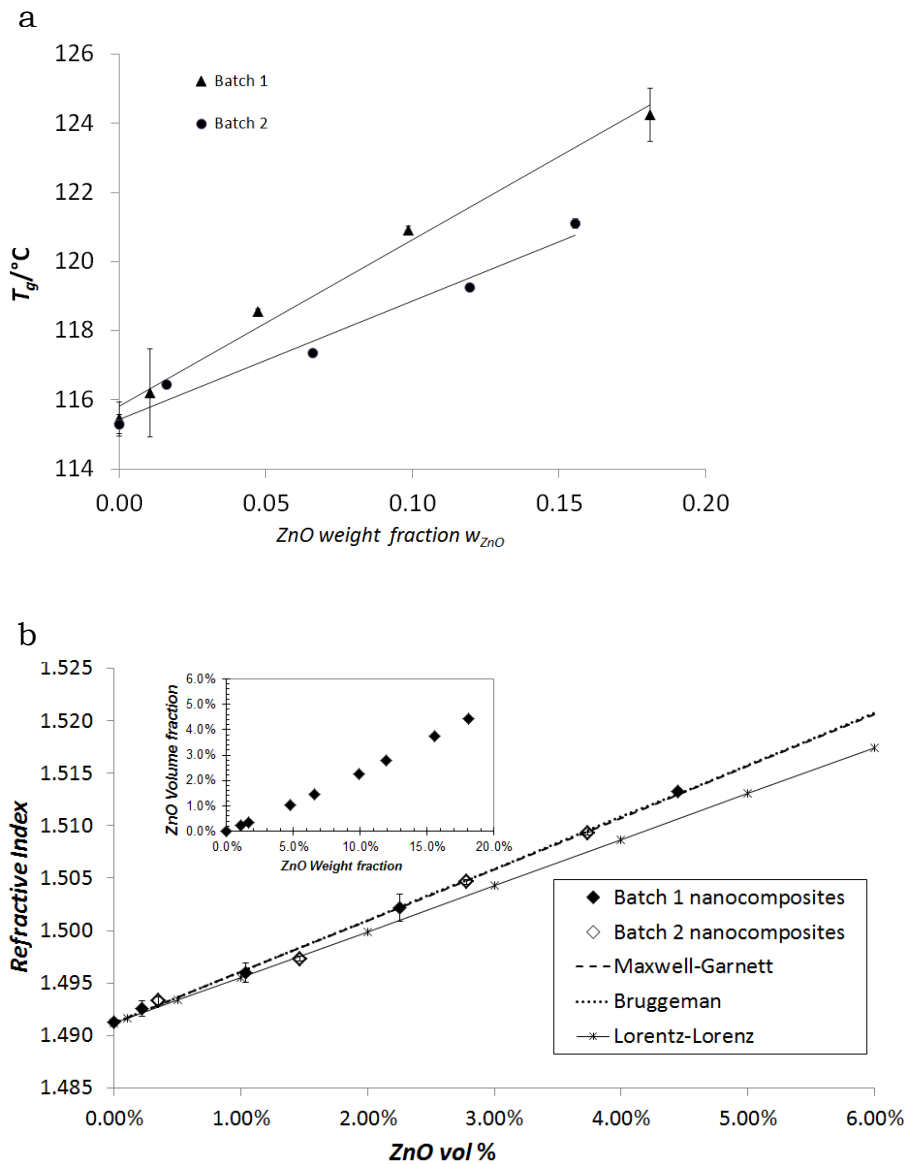


Figure 2.8 (a) Linear dependence of T_g to ZnO weight fraction demonstrates tunability of T_g by varying ZnO loading. Error bars indicate standard deviation. (b) Plot of refractive index against ZnO vol%. Theoretical predictions from Maxwell-Garnett, Bruggeman and Lorentz-Lorenz models are plotted for comparison. Error bars indicate standard deviation. (inset) ZnO volume fraction plotted against weight fraction.

2.6 Nature of Brushes

It is worthwhile to investigate the reasons for the stable dispersion of the PMMA-grafted ZnO. If the grafting degree g_d , which is the weight ratio between the grafted species to the particle, particle diameter D , particle density ρ and molecular weight of the grafted species M_g are known, the graft density σ can be calculated by the following equation

$$\sigma = \frac{g_d D \rho N_A}{6M_g} \quad 2-7$$

where N_A is Avogadro's number.

Based on elemental analysis, the graft density of silane on ZnO is found to be 1.05 molecules per nm². From the GPC results, using $M_n = 9.5 \text{ kgmol}^{-1}$, $g_d = 4.44$ (organic weight = 81.6%, inorganic weight = 18.4%), $D = 3.4 \text{ nm}$ and $\rho = 5.606 \text{ gcm}^{-3}$, the graft density for the major PMMA population is found to be 0.89 chains per nm². We note that the choice of M_n over M_w to calculate graft density is justified as it is closer to the chains with the most probable molecular weight in the molecular weight distribution. This result suggests that the grafted polymer chains did not occupy all available grafting sites. In spite of this, a very densely grafted nanoparticle is produced that is comparable to those reported in the literature using surface-initiated polymerization methods (1, 14, 128). The intriguing question is whether the minor polymer population is grafted to the nanoparticles or exists as free chains. Nevertheless, due to its extremely short chain length and low concentration, it is reasonable to assume that the minor population plays a small role in the brush-matrix interaction.

Based on the above results, the reduced tethered density $\Sigma = \sigma\pi R_g^2$ was found to be ~ 21 , assuming the unperturbed radius of gyration $R_g = 2.76$ nm (according to Tamai *et al.* (129) for $M_w = 10.9$ kgmol⁻¹). This implies that the grafted polymer forms an extended stretched-out brush if it consists of end-tethered chains, according to Brittain and Minko (130). To verify that a dense stretched-out brush was indeed formed, the particle size was analyzed by dynamic light scattering (DLS) and atomic force microscopy (AFM). Five aliquots of PMMA-grafted ZnO dispersed in acetone at a concentration of $\sim 10^{-3}$ gL⁻¹ were prepared and measured by DLS at 25°C. The Z-average diameter was reported as 37.8 ± 0.80 nm with a polydispersity of 0.121 ± 0.029 , CONTIN derived intensity-weighted distribution peak average was 46.6 ± 2.1 nm. A drop of acetone solution of $\sim 10^{-5}$ gL⁻¹ PMMA-grafted ZnO was deposited on a Si wafer cleaned by piranha solution (3:1 37% sulfuric acid and 30% hydrogen peroxide mixture; note: piranha solution is highly corrosive and exothermic when mixed with organic matter, proper safety precautions should be taken during handling), and subsequently dried at 70°C for 3 days before scanning with AFM. Figure 2.9a illustrates the height image of a $2 \mu\text{m} \times 2 \mu\text{m}$ area, respectively. The images revealed a uniform distribution of sparsely spaced nanoparticles that was conducive for particle analysis. Particle diameters from a $10 \mu\text{m} \times 10 \mu\text{m}$ area (not shown) were measured and plotted as a histogram in Figure 2.9b. A total of 150 nanoparticles was measured giving an average diameter of 33.8 ± 8.0 nm after tip convolution has been corrected for. Figure 2.9c illustrates a high resolution 3D image that reveals the hemispherical shape of the brush. The lateral dimensions of the particles were used to estimate brush height as it is known

that soft brushes can be compressed by the AFM tip, thus resulting in an underestimation of the brush height (11, 131). Brush height can be determined by subtracting the ZnO quantum dot radius (1.7 nm) from the measured nanoparticle radii. Thus the brush height is 17.3 nm, 22.0 nm and 15.3 nm as derived from the z-average, intensity-weighted distribution peak average and AFM diameters, respectively. We note that the z-average value is very close to the value obtained by AFM, providing further confirmation of the validity of the data. The theoretical stretched-out brush height is estimated by assuming an sp^3 bond angle of 109.5° between two consecutive C–C bonds (bond length = 0.154 nm) for a polymer chain fully extended in a line; the calculated values are 23.77 nm and 52.19 nm for a PMMA chain of $M_n = 9.5 \text{ kgmol}^{-1}$ and $M_w = 21 \text{ kgmol}^{-1}$, respectively. By this analysis, it is observed that the brush heights measured by both DLS and AFM are closer in value to the expected brush height of a fully extended chain with a molecular weight equivalent to M_n . Unfortunately, this does not allow us to conclude if tethering occurs mainly in the middle or the end of the chain due to the distribution of polymer chain lengths (we expect the AFM measured brush height tethered at the chain center in an ideal monodisperse brush to be half of the fully extended chain). However, the brush heights as measured by DLS are similar to the values reported by Dukes *et al.* (128) for polystyrene (which has a similar monomer size as PMMA) brushes of comparable M_w , suggesting that the brush is in the concentrated brush regime, which further implies that the brush is indeed densely packed and extended.

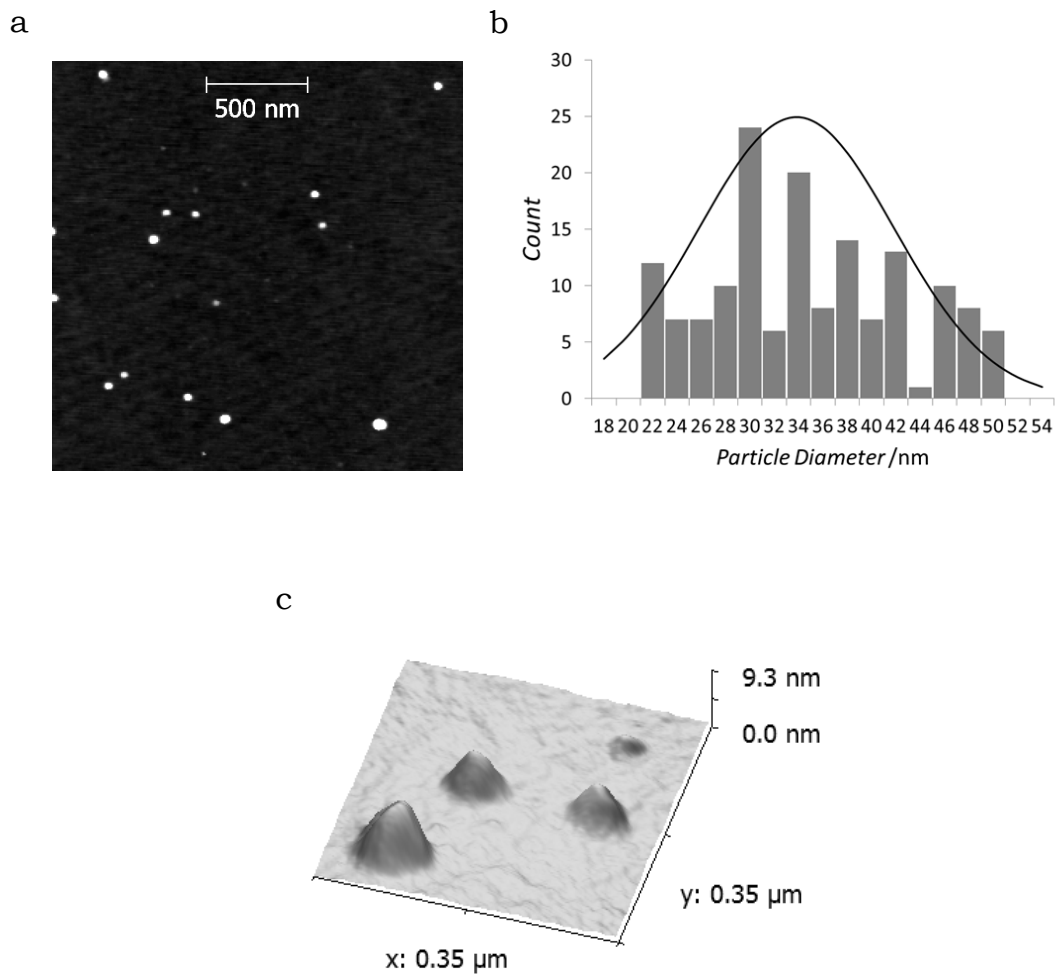


Figure 2.9 (a) AFM height image of a $2\ \mu\text{m} \times 2\ \mu\text{m}$ area of PMMA-grafted ZnO deposited on Si wafer. (b) Histogram of particle diameters measured from a total of 150 particles over a $10\ \mu\text{m} \times 10\ \mu\text{m}$ area (not shown) yielding an average of $33.8 \pm 8.0\ \text{nm}$. (c) High resolution 3D height profile of nanoparticles. Nanoparticles were dried at 70°C for 3 days before scanning.

2.7 Physics of Stable, Fine Nanoparticles Dispersion

Having established that a dense, extended brush was achieved, we can proceed to explain the stability of the nanoparticles. Although Leibler's analysis (23) is applicable to colloidal particles that are much larger than the unperturbed R_g of the brush, it ignores surface curvature effects that allow for a more open brush configuration similar to a star polymer (132), and hence performs poorly in explaining observations of stable dispersions of small nanoparticles when $P > N$ (14, 25). Surface curvature effects were discussed in detail by Trombly and Ganesan (28), who identified two parameters characterizing the surface curvature of the system; R/R_g , the ratio of the particle radius to unperturbed radius of gyration of the brush and H_b/R , the ratio of the brush height to particle radius. Simulation studies concluded that at high curvatures $R/R_g = 1$, matrix-brush interpenetration is greater, attractive potential between nanoparticles is decreased and polymer brush is compressed more deeply. Significantly, lower R/R_g values increase matrix-brush interpenetration even when the matrix chain length is larger than grafted chain length. These results also correlate with that at the limit of high curvature $H_b/R \gg 1$, where increased matrix-brush interpenetration is observed. It was also found that the effect of high graft density in inducing dewetting of the polymer brush is less important for highly curved nanoparticles. The overall effect of high curvature is the better dispersion of the nanoparticles. In the current brush-nanoparticle system, we find that $R/R_g = 0.6$ and H_b/R ranges from 10 to 22 depending on the particular brush height value employed, thus satisfying the high surface curvature criteria.

To date, little effort has been made in studying the impact of brush polydispersity on nanoparticle dispersion. However, it was found through simulation by Smith and Bedrov (133) that at $P/N = 14$, good dispersion of monodisperse brush tethered nanoparticle is still possible provided that brush density is low. It was suggested in the same study that in the case of high brush density, *a combination of long and very short brushes* would result in good nanoparticle dispersions. The long brushes would facilitate brush-matrix interpenetration, while the very short brushes would prevent direct contact between nanoparticles. These predictions are consistent with our observations as the broad PDI (~2.2) of our grafted PMMA includes a substantial fraction of long and very short polymer chains. We note that $P/N = 7$ for our polymer tethered nanoparticles, by contrast, poor dispersion occurs when P/N is greater than 4 in the polystyrene (PS) nanocomposites of 13.4 nm silica nanoparticles tethered by monodisperse brush ($M_n = 24 \text{ kgmol}^{-1}$, PDI = 1.3) dispersed in polydisperse matrix ($M_n = 140 \text{ kgmol}^{-1}$, PDI = 2) studied by Chevigny *et al.* (25).

Finally, it could be argued that the observed stability is a kinetic effect due to high shear during melt-blending, which can break up aggregates to form a more homogeneous dispersion—an effect absent in a nanocomposite prepared via solution methods. However, the nanoparticles remain finely dispersed even after prolonged annealing. Although we cannot rule out kinetic effects definitively in our experiments, a review of the results of Akcora *et al.* (26) who employed similar annealing steps in comparable nanocomposites resulted in complex anisotropic aggregates; in contrast to the extraordinary stability of our nanoparticles. Since any stabilization provided by the

kinetic effect would be lost after such a prolonged period in the melt phase, this comparison supports the assertion that the stability of our nanoparticles can be accounted for based on the aforementioned thermodynamic arguments alone.

2.8 Conclusions

We presented a method of preparing melt-processable nanoparticle–nanocomposites exhibiting tunable multifunctional properties as a result of their fine dispersion state. This method features several unique advantages that allow for the exploitation of useful functional properties that can be brought about only by the incorporation of inorganic nanoparticles into a polymer. The key findings can be summarized as follows:

- (1) The grafting of polymers onto inorganic nanoparticles is achieved *via* free radical copolymerization. This synthesis method presents several advantages over traditional surface-initiated polymerization techniques, which often rely on controlled polymerization techniques such as *RAFT* and *ATRP*. The free radical copolymerization approach can be applied to a wide range of free radical type monomers, while controlled polymerization techniques require a catalyst or initiator that works optimally only for specific monomers or inorganic nanoparticles. Furthermore, due to the affinity of silanes to inorganic materials in general, the present method can also be applied to most inorganic nanoparticles without the need to develop a specific catalyst or initiator for each monomer/inorganic nanoparticle combination. Thus, this approach is generally

applicable to diverse nanoparticle/polymer combinations as opposed to the specificity of surface-initiated techniques.

- (2) Although free radical copolymerization yields a wider molecular weight distribution in the grafted polymers, we have shown in this study that this is beneficial for dispersing nanoparticles. In fact, the stabilization effect is the result of a combination of wide molecular weight distribution and high nanoparticle surface curvature. An additional unexplored factor could be that tethering is located along the chain instead of being end-tethered, which cannot be confirmed at present but will be the focus of future studies. As a result of the effectiveness of these stabilization mechanisms, the requirement for a limited range of P/N ratios and optimal graft density is relaxed. This allows for a larger design window in the grafted polymer chain length and the amount of polymer grafted onto the nanoparticle in applications.
- (3) We demonstrated that the resultant nanocomposites exhibit concurrently finely tunable functional properties in refractive index, T_g and bandgap energy. Tunability in multiple functionalities in a melt-processed nanocomposite is highly desirable. In principle, additional functionalities can be introduced simply by incorporating different types of functional nanoparticles, hence expanding the possibilities of functional materials.
- (4) The ability of the nanocomposites to be melt-processable while maintaining the fine dispersion of nanoparticles is particularly attractive for manufacturers. This allows for nanoparticles to be utilized as additives which can be easily added to

a base polymer to create novel polymer nanocomposites. The inexpensive and high-throughput melt-blending process potentially allows for more high performance nanocomposites to appear in commercial applications. Some potential applications are optical components requiring tunable refractive index and/or T_g , photoresists with size- or concentration-dependent absorption, dielectric metamaterials, magnetic and piezoelectric-based smart materials, sensors and actuators.

CHAPTER III

GLASS TRANSITION TEMPERATURE CHANGES OF MELT-BLENDED POLYMER NANOCOMPOSITES CONTAINING FINELY DISPERSED ZINC OXIDE QUANTUM DOTS*

3.1 Introduction

A method to synthesize ZnO/poly(methyl methacrylate) (PMMA) hybrid materials that is melt-blendable has been developed. Such a material allows us to easily control the amount of nanofiller in a host polymer. Unlike commonly used techniques such as solvent casting (66, 134), the melt-blending process is a practical and widely used industrial technique for most commercial polymers. Other techniques, such as *in situ* polymerization of nanofillers (16, 135) induces gelation during synthesis, thereby complicating the study of glass transition behavior due to the presence of chemical crosslinks. It is shown that the glass transition of a PNC system of homogeneously dispersed zinc oxide (ZnO) quantum dots in PMMA exhibits a power law that supports the Long-Lequeux model. The primary goal of this chapter is to quantify the glass transition behavior of this hybrid material. The secondary goal is to demonstrate that the physical models of polymer thin films can be applied to a bulk, melt-blended PNC. By demonstrating that this is possible allows us to simplify the analysis of nanocomposites by applying the insights gained from the relatively long history of polymer thin film research.

*Reprinted by permission of the Royal Society of Chemistry from "Glass Transition Temperature Changes of Melt-Blended Polymer Nanocomposites containing Finely Dispersed ZnO Quantum Dots" by Minhao Wong *et al.* 2010, *Soft Matter*, 6, 4482-4490.
Copyright 2010, the Royal Society of Chemistry, Cambridge, UK. <http://pubs.rsc.org/en/Content/ArticleLanding/2010/SM/b927182a>

3.2 Methods and Materials

The details of the synthesis method of monodisperse ZnO quantum dots (QD) of 5 nm diameter and the resulting properties have been reported (101, 107). Using the grafting method described in Chapter II, sufficient quantities (>100g) of PMMA-grafted ZnO nanoparticles for melt-blending experiments have been produced. The master batches of grafted ZnO were melt-blended with PMMA at temperatures ranging 180°C to 200°C (Table 2.1).

3.2.1 Materials for Synthesis

N,N – dimethylformamide (DMF), methanol, and toluene were used as solvents. The initiator 2,2'-azobisisobutyronitrile (AIBN) and monomer methyl methacrylate (MMA) with 0.005% hydroquinone were used in the polymerization of PMMA. Zinc acetate dihydrate and potassium hydroxide were semiconductor grade chemicals. The silane coupling agent 3-(trimethoxysilyl)propyl methacrylate (TSMA) 98% was used in the modification of ZnO QDs. Poly(methyl methacrylate) (PMMA, Sumipex® Ex, Sumitomo Chemicals) was obtained, and the PMMA was analyzed by gel-permeation chromatography using a standard polystyrene reference. Number average molecular weight (M_n), weight average molecular weight (M_w) and polydispersity index were 80,000, 155,000 and 1.9375, respectively. MMA was purified through an activated alumina column to remove hydroquinone. All other chemicals were used as received.

3.2.2 Preparation of TSMA-ZnO Nanoparticles

The synthesis method of ZnO QDs has been previously reported by Sun *et al.* (101, 107). We use a modification of this method in the current experiment. 175.61 g of zinc

acetate dihydrate was dissolved in 1200 mL of methanol under stirring at 60°C, after which the solution was allowed to cool to 25°C. An alkali solution was prepared using 89.78 g of potassium hydroxide pellets, which were dissolved in 2800 mL of methanol under stirring and temperature was maintained at 25°C. The zinc acetate dihydrate solution was rapidly poured into the alkali solution while stirring. Solution turbidity was observed, which eventually cleared up within an hour, yielding a transparent solution. The reaction was allowed to continue for 1 hour, after which the solution was cooled to 0-5°C to halt further nanocrystal growth and aggregation. The solution thus prepared yielded 4000 mL of 0.2 M ZnO colloidal solution. 8.11 g of TSMA was dissolved in 154.11 g of methanol to produce a 5% TSMA/methanol solution. The ZnO colloidal solution prepared was brought to 25°C, after which the TSMA/methanol solution was added while stirring. The mixture was then heated to 60°C for 2 hours. This solution contained a mixture of potassium acetate and TSMA modified ZnO nanoparticles. To remove the potassium acetate, a solvent exchange step was carried out. The volume of the TSMA-ZnO mixture was reduced to one-fourth the original volume and 1000 mL of DMF was then added to the solution. This mixture was further evaporated until about 90% of the methanol was removed, resulting in precipitation of potassium acetate crystals. The precipitated mixture was subsequently filtered to remove the crystals. The amount of methanol lost was determined by measuring the weight loss from the solution. Evaporation was stopped when 570 g (excluding weight loss from the precipitation of potassium acetate) of the original weight of methanol was evaporated. Further filtration was performed to remove precipitates that appeared after evaporation. 955 g of the

TSMA-ZnO/DMF solution was obtained, and this solution was pale yellow and transparent.

3.2.3 Preparation of ZnO/PMMA Nanocomposites

The stock solution prepared above was used to prepare two master batches of ZnO/PMMA inorganic-organic hybrid material according to the recipe given in Table 2.2 **Experimental conditions for the grafting of PMMA to ZnO.**, where reactions 6 and 7 are identified as Batches 1 and 2, respectively.

Batch 1 –1286g of DMF, 164.8 g of MMA and 2 wt% (relative to MMA) of initiator AIBN were added to 354.6 g of TSMA-ZnO/DMF solution. The polymerization solution was purged with nitrogen followed by polymerization at 85°C for 5 hours under nitrogen atmosphere. After polymerization was completed, the solution was concentrated using a rotary evaporator at 50°C to 400 mL. The concentrated solution was slowly added to 2000 mL cold methanol and the precipitate was allowed to settle at the bottom of the beaker. The sediment was separated from the supernatant by decantation. The recovered sediment was redissolved in 200 mL of toluene to form a light yellow, transparent solution. The ZnO/PMMA hybrid/toluene solution was subsequently precipitated in cold methanol three more times following the same procedure. A white polymeric solid was obtained, which was then dried in a vacuum oven at 80°C for 10 hours. Free, ungrafted polymer produced during synthesis was removed by repeated precipitation from solution, and this was confirmed by observing the residual weight from thermal gravimetric analysis (TGA) of the solid collected from each precipitation. The residual weight did not change significantly (within 1%) after the fourth precipitation step.

Batch 2 – The recipe described in Table 2.2 was used and a procedure identical to Batch 1 was followed. Despite the nominally identical amounts of reagents used in Batch 2, the master batch obtained in the second synthesis contained a different ZnO content. We attribute this to the inhomogeneity that occurred during polymerization, where the thermal profile in solution could not be precisely controlled due to the size of the reactor, which might have caused different grafting rates on the ZnO surfaces.

3.2.4 Elemental Analysis

The ZnO and Si contents of the master batch and melt-blended samples were determined using Inductively Coupled Plasma Atomic Emission Spectroscopy (ICP-AES) (ICPS-8100, Shimadzu). Zinc content was first determined then multiplied by a factor of 1.245 (weight ratio of ZnO/Zn) to obtain ZnO content. Determination of Zn and Si content provided an indication of the amount of silane coupling agents attached to the ZnO surface. The weight ratio of Si/Zn = 0.0195 was essentially the same for each batch.

3.2.5 Transmission Electron Microscopy

Procedures for sample preparation and transmission electron microscopy are described in section 2.3.5.

3.2.6 Thermal Analysis

Dynamic mechanical analysis (DMA) was performed in the tensile mode using a dynamic viscoelastic analyzer (DVA-200, IT Keisoku Seigyō Corporation, Osaka, Japan). DMA samples were in the form of bars of 30 mm × 5 mm × 3 mm prepared by cutting injection molded samples with a precision saw (Buehler Isomet). Temperature was ramped from 300K to 433K (25 °C to 160°C) at 5 K per minute. Testing frequency

was 10Hz and the dynamic strain was set at 0.1 % to measure the dynamic modulus. Each data point was obtained by taking the average reading of three samples. Differential scanning calorimetry (DSC) was conducted under nitrogen flowing at a rate of 20 mL/min, and the heating rate was 20 K per minute. One thermal cycle involved ramping from 300K to 473 K (25 °C to 200°C) then air cooling to room temperature. Glass transition temperature, T_g was taken as the peak in the derivative plot of the DSC heating curve. The heating cycles were repeated until a consistent T_g value was obtained. This was typically achieved on the third or fourth cycle. Each data point was obtained by taking the average reading of two samples.

3.3 Transparent Nanocomposites Composing of Fine Dispersions of Nanoparticles

The methods described above yielded stable, uniform dispersions of ZnO, as evidenced by transmission electron microscopy (TEM) and UV-vis spectroscopy. The homogeneous dispersion of the ZnO QDs (QD) was apparent in the TEM images, as shown in Figure 2.5 (left column). TEM images of the nanocomposites at lower magnification showed that the ZnO QDs were homogeneously dispersed throughout the matrix, without any significant agglomeration. A few clusters of 4–10 QDs were observed in the nanocomposites with lower ZnO content when observed at higher magnification (inset images of Figure 2.5 (left column)). Photographs of the injection-molded ZnO nanocomposite bars typically showed excellent transparency (Figure 3.1). The results show that repeated thermal processing by melt-blending, injection and compression molding did not affect the dispersion quality of the QDs.

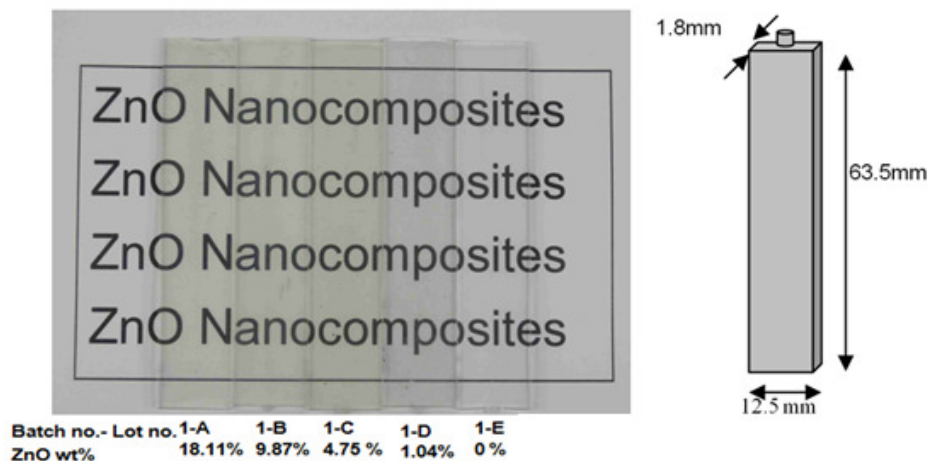


Figure 3.1 ZnO nanocomposite bars made by injection molding are shown in the photograph on the left, showing excellent transparency even after thermal processing. Dimensions of the bars are shown in the schematic on the right.

3.4 Linear Dependence of T_g on ZnO Concentration

Representative DMA plots are shown in Figure 3.2. Figure 3.2a shows the storage moduli and Figure 3.2b shows the loss moduli curves. Figure 3.2c shows the α -relaxation peaks, T_α for samples at different ZnO loadings. The storage moduli at 50°C are plotted against ZnO content in Figure 3.2d; error bars indicate standard deviation. Representative DSC curves are shown in Figure 3.3a shows the glass transition step in the normalized DSC curves for batch 1 and batch 2 samples. Figure 3.3b shows the derivative plots of the normalized DSC curves whereby the T_g s are read from the peak positions. The increase in specific heat capacity (ΔC_p) during glass transition was measured and plotted against ZnO weight content in Figure 3.3c.

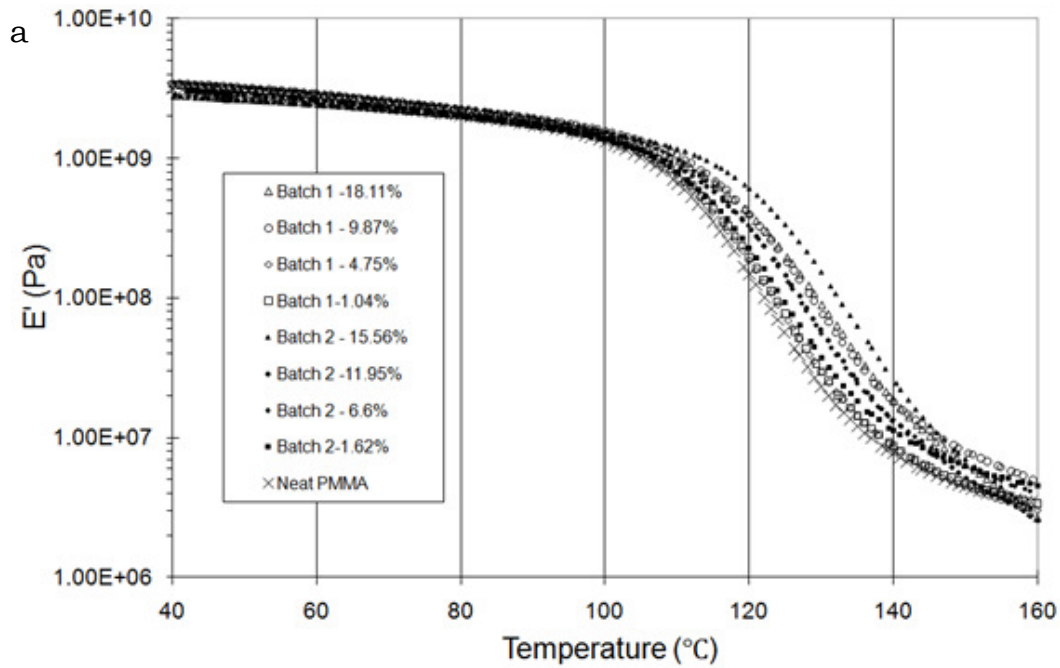
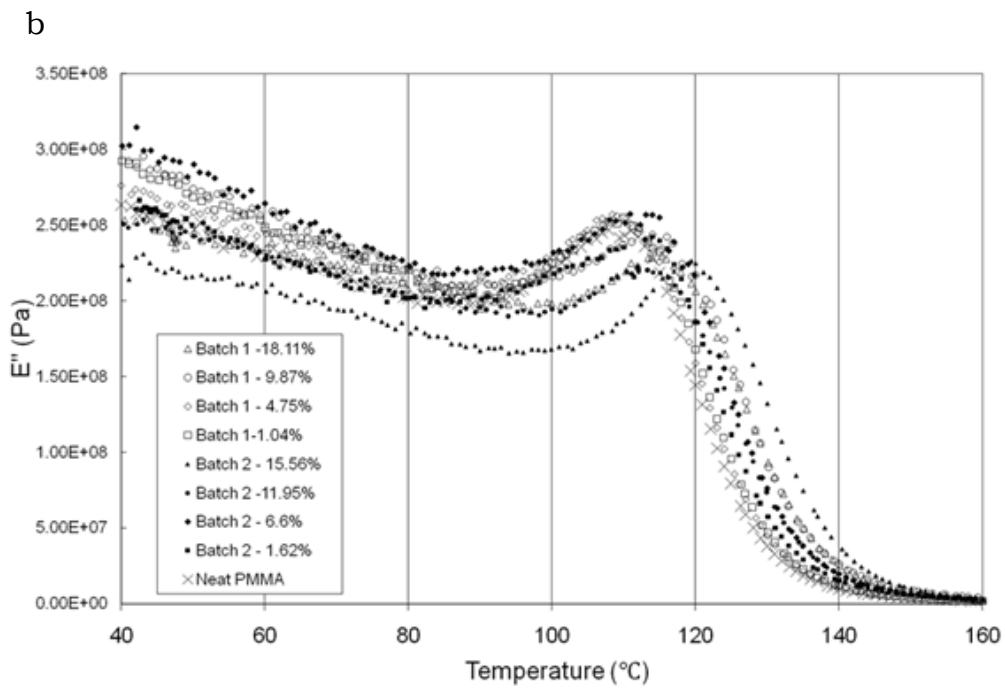
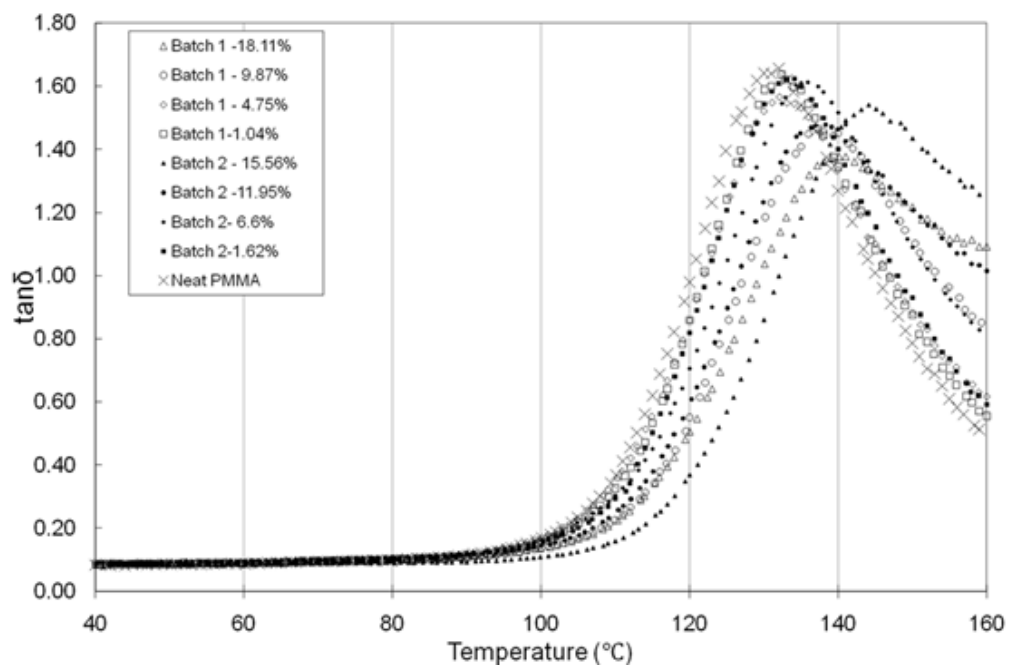


Figure 3.2 Representative DMA curves for different weight fractions of nanocomposite. (a) Storage moduli plots and (b) loss moduli plots shift right with ZnO content. (c) α -relaxation peaks clearly shift right with increasing ZnO content. (d) Storage moduli at 50°C of nanocomposite plotted against ZnO content.



c



d

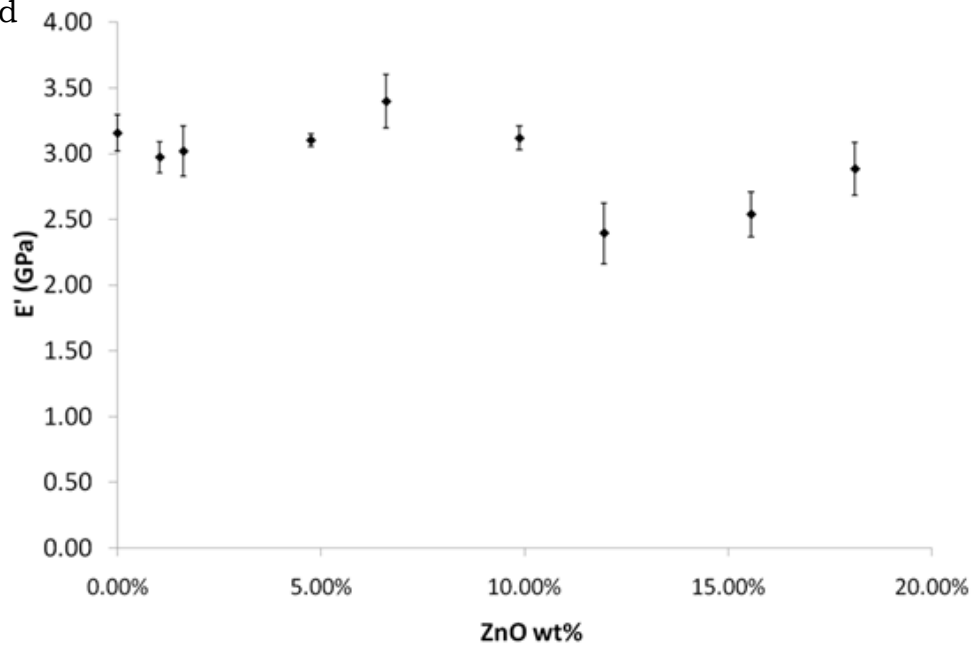
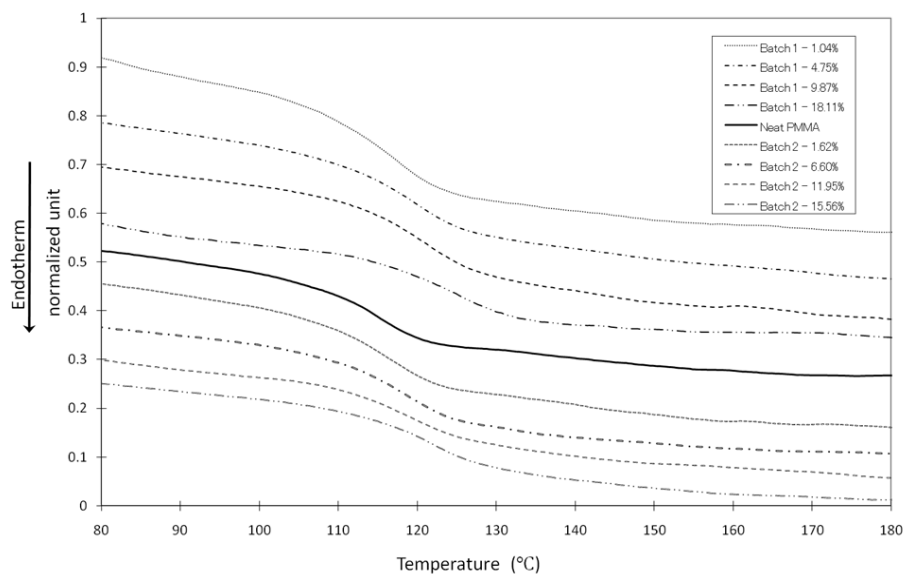


Figure 3.2 Continued.

a



b

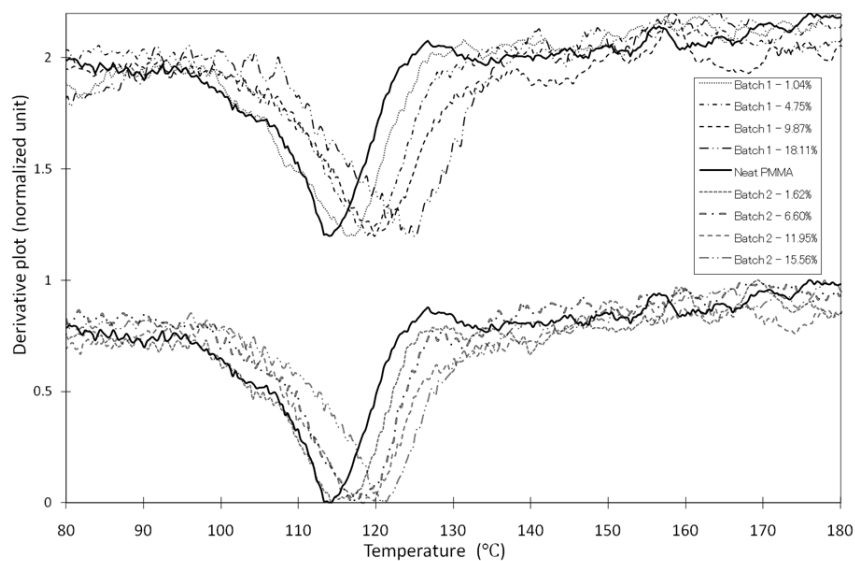


Figure 3.3 Representative normalized DSC curves for different weight fractions of nanocomposite. (a) Glass step of batch 1 samples (top) and batch 2 samples (bottom), DSC curves were normalized and offset vertically for clarity. (b) Derivative plots of normalized DSC curve of batch 1 samples (top) and batch 2 samples (bottom). Note: Peaks in the derivative plots shift right as ZnO content increases. (c) ΔC_p during glass transition decreases consistently with increasing filler content.

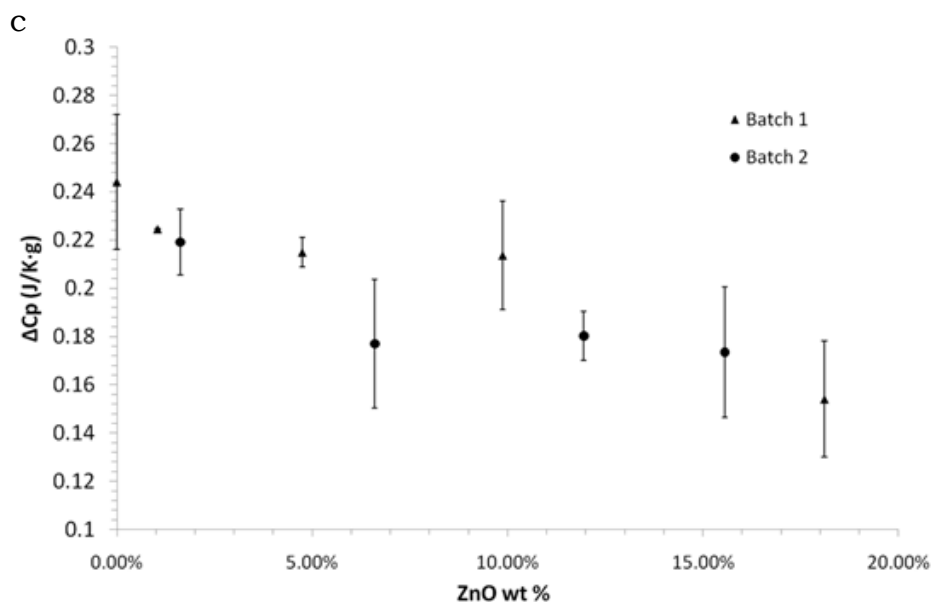


Figure 3.3 Continued.

We evaluated the initial plateau moduli from the DMA curves (Figure 3.2d) but were unable to find a clear relation with ZnO content. The presence of stiff inorganic fillers is expected to increase the elastic moduli of the nanocomposite. The fact that such an increase was not observed can be explained by the following reasons. Nanocomposites with ZnO weight content about 10% and above were highly brittle, which created difficulties in fabricating samples of uniform geometry and in loading the samples onto the test fixtures. Minute changes in sample gripping stress and sample position can cause significant errors in the measurement of moduli. In addition, polymer chains that were grafted onto ZnO QDs have a much lower molecular weight compared to the matrix polymer. As ZnO content increases, the lower molecular weight polymer contributes to lower the elastic modulus of the nanocomposite. By contrast, the loss modulus (E'') peaks (Figure 3.2b) and the α -relaxation peaks ($\tan \delta$ peaks) (Figure 3.2c)

show a consistent trend of increasing with ZnO content. A similar trend is seen when we analyze the glass steps of the DSC curves (Figure 3.3a) . The derivative plots (Figure 3.3b) clearly show the gradual shift of the peak positions to higher temperatures at increasing ZnO content. Strong interaction between inorganic filler and polymer matrix typically reduces the glass transition step (ΔC_p). This effect has been attributed to steric hindrance and restriction of mobility of the polymer chains adjacent to the filler surface (136-138). As expected, Figure 3.3c shows that ΔC_p decreases consistently with ZnO content.

Figure 3.4a shows that the T_g of the nanocomposites increases linearly with increasing ZnO weight fraction, w_{ZnO} . This trend was observed in both batches of nanocomposites and was consistently reproduced in DMA (both from E'' and $\tan \delta$ peaks or T_α) and DSC measurements. The T_α increase was as much as 11 K and the E'' peak increased by 9.15 K at 15.56 wt% when measured by DMA (Figure 3.2b-c), while DSC shows the greatest T_g increase was ~8.8 K at 18.11 wt% (Figure 3.4a and Figure 3.4b). In general, the T_g values measured by DSC showed less scatter than the values measured by DMA, and adhered better to the linear trend. It is also interesting to note that data from the $\tan \delta$ peaks conform to the DSC data much better than the E'' peaks (Figure 3.4a and Figure 3.5a). We note that the slopes of the DMA curves (both storage and loss moduli) near T_g show a more consistent profile than the height and position of the E'' peaks. The $\tan \delta$ peaks are closer to the inflection point of the slopes (139) and thus are reflective of this consistent trend. From a physical point of view, the E'' peak can be regarded as the dissipation term in the fluctuation dissipation theorem (FDT) (140),

whereas the $\tan \delta$ peak is not as well-understood in the physical sense. Despite this shortcoming, the analysis of this study will be based on the $\tan \delta$ peak due to its better consistency.

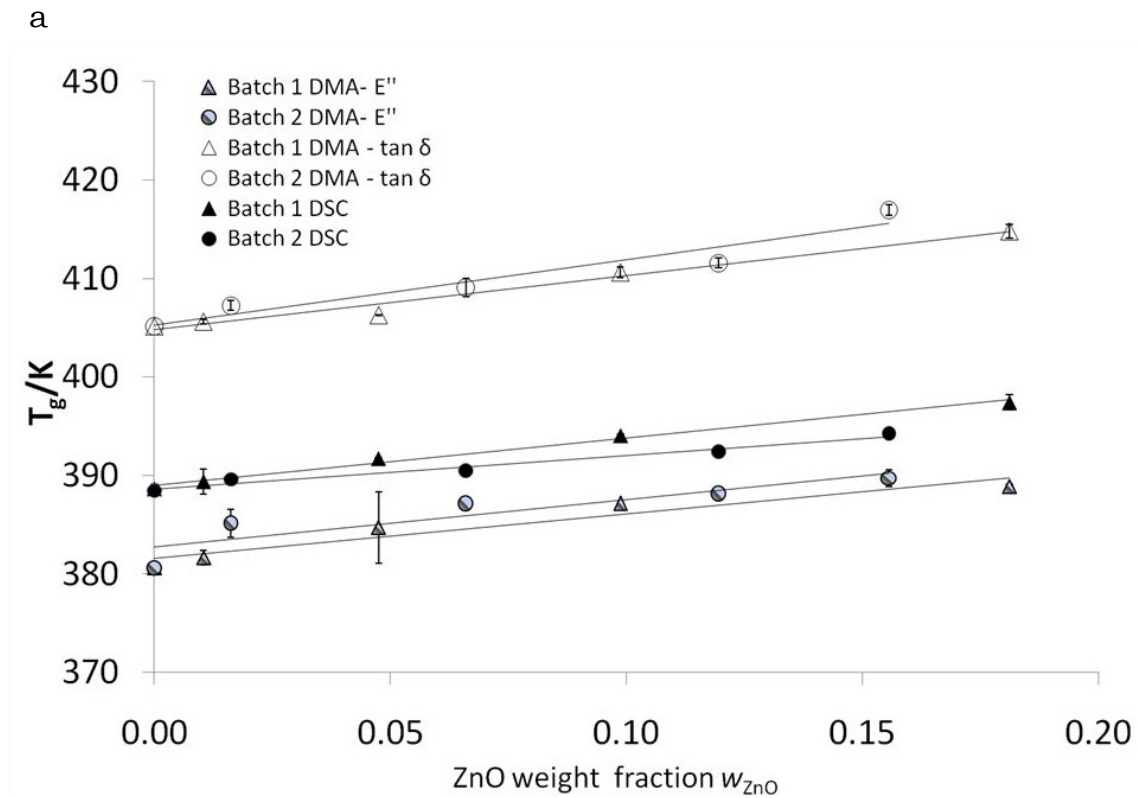


Figure 3.4 (a) Increasing T_g with ZnO weight fraction, w_{ZnO} . DMA data from E'' (half-filled symbols) and $\tan \delta$ peaks (open symbols) are presented. Error bars indicate standard deviation of each data point and are largely hidden in the DSC data (filled symbols) because they are smaller than the shapes representing the data points. (b) $T_g - T_{g \text{ bulk}}$ dependence on weight fraction w_{ZnO} shows linear dependence. Error bars indicate standard deviation of each data point.

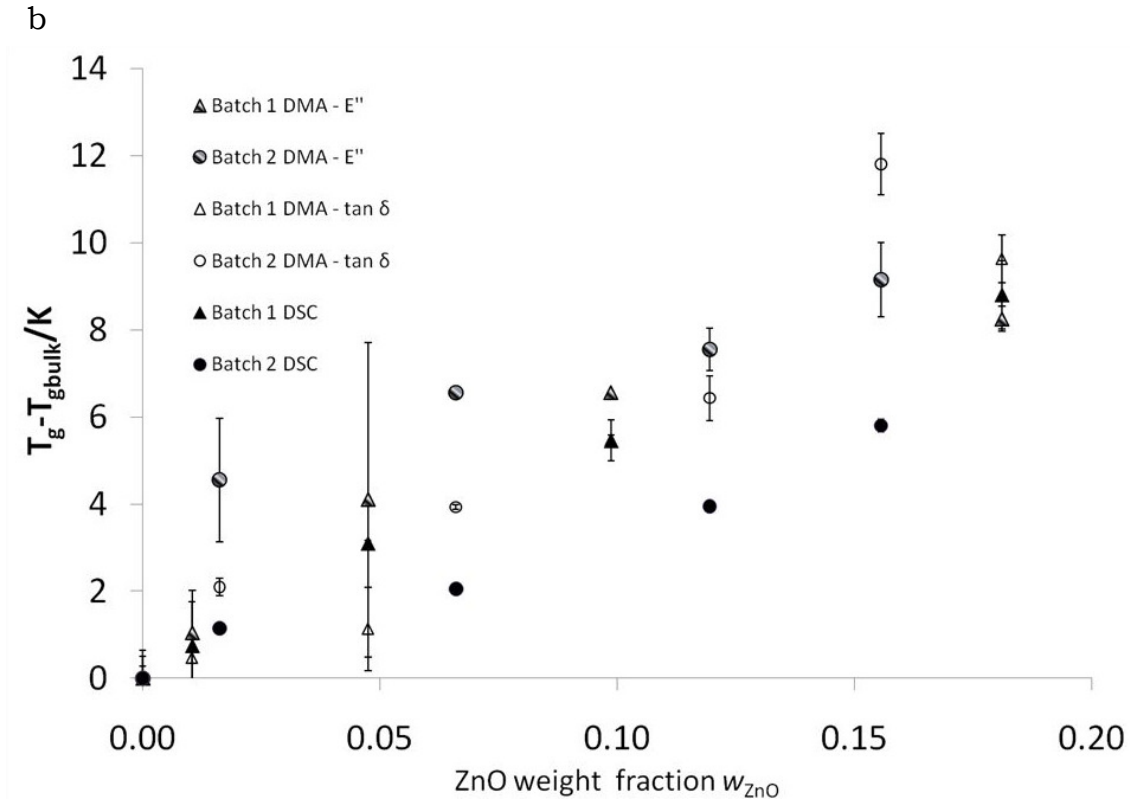


Figure 3.4 Continued.

3.5 A Quantitative Model for T_g Behavior in Nanocomposites

T_g increases have been reported for PMMA strongly adsorbed onto silica particles (141), and for silicate-epoxy nanocomposites (142). Earlier studies (143) showed that T_g saturated at ~ 10 wt % ZnO nanoparticles in polystyrene, which is not the case here. We attribute this to improved dispersion, which ensures that the entire surface area of the ZnO QDs is available for interaction with polymer chains, even at high loadings. Such a strong linear correlation between T_g and ZnO weight fraction was unexpected, given that previous studies of PNCs did not report such a dependence (65, 66). However, this can be rationally understood in terms of the physics of polymer thin films, discussed below.

Based on the theory of percolation of slow dynamic domains, Long and Lequeux (60) proposed that for thin films supported by strongly interacting surfaces, T_g and h_f , are related by

$$h_f = \frac{a^* \mu_2}{\theta} \left(\frac{2.5}{N_c^{\frac{1}{2} - \frac{1}{3\nu}}} \frac{T_{g,bulk}}{T_g - T_{g,bulk}} \right)^\nu \quad 3-1$$

where a^* is one monomer length, μ_2 and θ are adjustable parameters of the order unity, N_c is the characteristic number of monomers in the dynamic domain responsible for T_g behavior, $T_{g,bulk}$ is the T_g of the bulk polymer, and ν is an exponent required by 3D percolation, which is predicted to be 0.88. We derive a general form of Equation 3-1, giving:

$$\frac{T_g - T_{g,bulk}}{T_{g,bulk}} = \frac{\Delta T_g}{T_{g,bulk}} = B h_p^{-\frac{1}{\nu}} \quad 3-2$$

The parameter B is defined as $B \equiv (a^* \mu_2 / \theta)^{\nu} (2.5 / N_c^{1/2 - 1/\nu})$. By replacing h_f with h_p , the percolation exponent, ν can be obtained from the plot of $\Delta T_g / T_{g,bulk}$ against h_p . $T_{g,bulk}$ can be verified independently by measuring the T_g of the virgin polymer. To obtain h_p , we consider that the QDs are homogeneously and randomly dispersed. We can relate the interparticle distance h_p to the nanoparticle volume fraction ϕ and nanoparticle radius a , by the following equation, $h_p = 2a[(\phi_0/\phi)^{1/3} - 1]$ where $\phi_0 = 0.64$, is the maximum volume fraction of a random disordered particle system (120). The interparticle distance h_p derived from this equation is an average value based solely on weight content of the

nanoparticles in the nanocomposite. Despite the fact that some local clustering and agglomeration of nanoparticles was observed from the TEM images, the high level of transparency indicates minimal scattering by agglomerates. We assert that the agglomerated nanoparticles do not significantly affect our attempt to describe our results by a quantitative model. The rationale for this assertion is discussed later.

In accordance with Equation 3-2, $\Delta T_g / T_{g,bulk}$ was plotted against h_p in Figure 3.5a. Note that despite the large disparity of the linear graphs for DSC and DMA data shown in Figure 3.4a, the data sets in the plots of $\Delta T_g / T_{g,bulk}$ against h_p are convergent and appear to follow a power law. Curve fitting was performed on both data sets collected from DSC and DMA measurements, yielding values for $1/\nu$ of 1.572 and 1.809 for the DSC and DMA ($\tan \delta$) data, respectively. This in turn gave values of 0.64 and 0.55 for ν from the DSC and DMA ($\tan \delta$) data, respectively. To further validate the application of the Long-Lequeux model, we can extract $T_{g,bulk}$ values from the power law.

We can rearrange Equation 3-2 into the following forms,

$$T_g h_p^{\frac{1}{\nu}} = T_{g,bulk} h_p^{\frac{1}{\nu}} + B T_{g,bulk} \quad 3-3$$

$$T_g = T_{g,bulk} + \frac{B T_{g,bulk}}{h_p^{\frac{1}{\nu}}} \quad 3-4$$

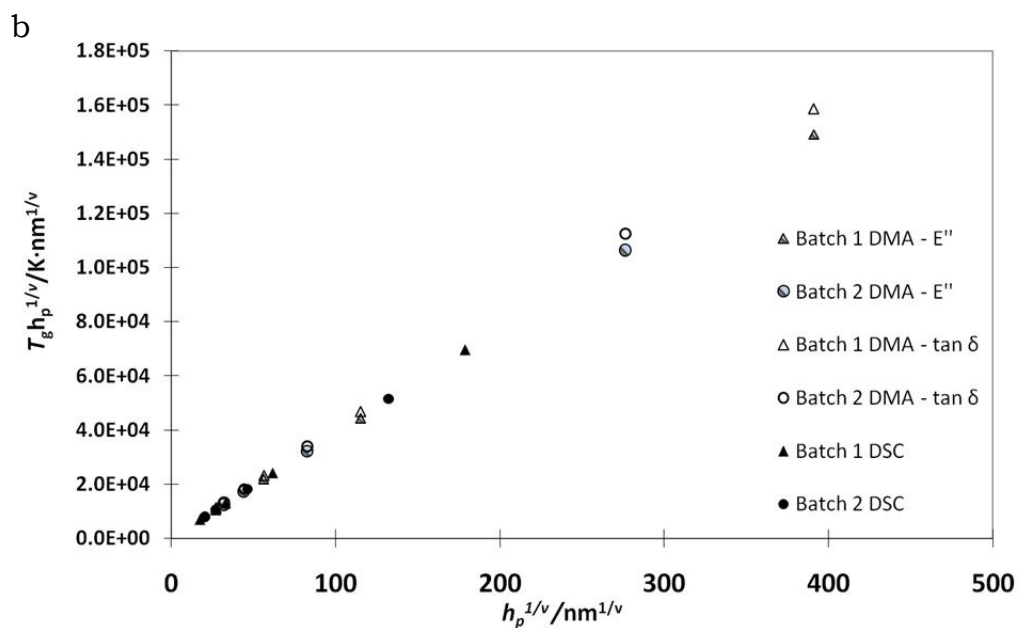
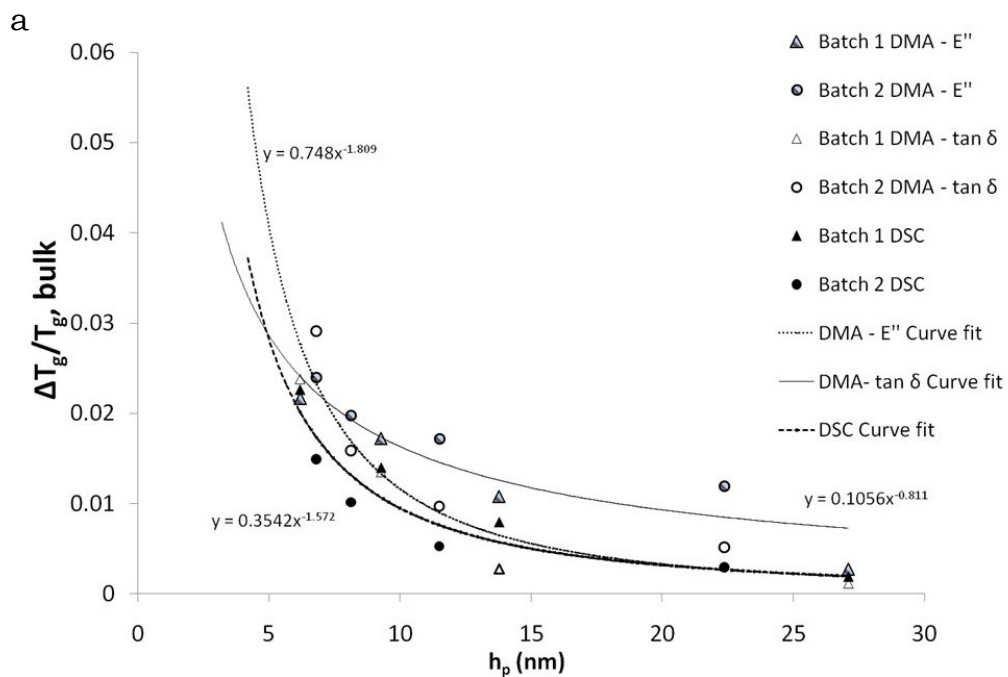


Figure 3.5 DMA data from E'' (half-filled symbols) and $\tan \delta$ peaks (open symbols) and DSC data (filled symbols) are presented. (a) The power law dependence of interparticle distance, h_p to T_g . Graphs of $\Delta T_g / T_{g, \text{bulk}}$ vs h_p are plotted to obtain the value of the exponent ν . (b) Graphs of $T_g h_p^{1/\nu}$ vs $h_p^{1/\nu}$ are plotted and the slope is read to obtain $T_{g, \text{bulk}}$. (c) T_g varies linearly to $h_p^{-1/\nu}$, verifying Equation 3-4 and reproduces the trend observed in Figure 3.4a. Inset graph shows the linear dependence of $h_p^{-1/\nu}$ to w_{ZnO} .

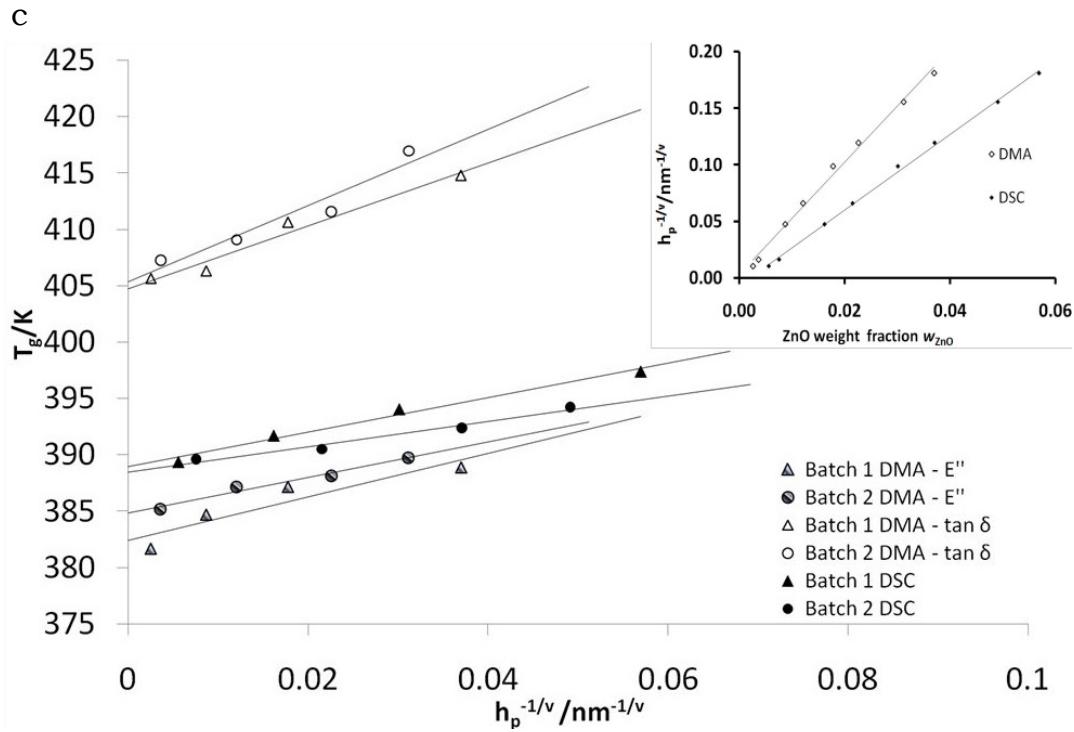


Figure 3.5 Continued.

The graphs of $T_g h_p^{1/\nu}$ against $h_p^{1/\nu}$ (Figure 3.5b) show the strong correlation of the data to a linear profile. These results confirm that T_g is following a power law of h_p . We note that $T_{g,bulk}$ values can be read from the slopes of the graphs. From the DSC data, $T_{g,bulk}$ was determined to be 388.4 K and 388.8 K for Batches 1 and 2, respectively. From the DMA data, $T_{\alpha,bulk}$ was taken as 404.9 K and 406.2 K for Batches 1 and 2, respectively. Alternatively, $T_{g,bulk}$ can be obtained by an extrapolation of $1/h_p^{1/\nu}$ to zero in the graph of T_g versus $1/h_p^{1/\nu}$. Figure 3.5c shows that T_g varies linearly with $1/h_p^{1/\nu}$. From the DSC data, $T_{g,bulk}$ was determined to be 389.0 K and 388.4 K for Batches 1 and 2, respectively. From the DMA data, $T_{\alpha,bulk}$ is taken as 404.7 K and 405.4 K for Batches

1 and 2, respectively. The bulk values extracted from both methods are consistent with the bulk values obtained from direct measurements by DSC and DMA (Table 3.1). The linear profile obtained in Figure 3.5c reproduces the profile shown earlier in Figure 3.4a. The plot of $1/h_p^{1/\nu}$ against w_{ZnO} (inset Figure 3.5c) shows a clearly linear dependence. In general, $1/h_p^{1/\nu}$ is not linearly dependent on w_{ZnO} ; however, within the range of weight fraction used here, a linear trend fits the data well. Thus, we conclude that the apparent linear dependence of T_g on weight fraction of nanofiller is consistent with the Long-Lequeux model.

	Measured values	Values derived via Equation 3-3	Values derived via Equation 3-4		
	$T_{\alpha,\text{bulk}}$ or $T_{g,\text{bulk}}/\text{K}$	$T_{\alpha,\text{bulk}}$ or $T_{g,\text{bulk}}/\text{K}$	A/nm	$T_{\alpha,\text{bulk}}$ or $T_{g,\text{bulk}}/\text{K}$	A/nm
Batch 1 DMA	405.2	404.9	0.77	404.7	0.81
Batch 2 DMA	405.2	406.2	0.81	405.4	0.90
Batch 1 DSC	388.5	388.4	0.61	389.0	0.55
Batch 2 DSC	388.5	388.8	0.41	388.4	0.45

Table 3.1 Comparison of $T_{g,\text{bulk}}$ and derived characteristic lengths

The agglomeration of QDs observed in TEM images casts requires re-examination of the assumption of random packing (*vide supra*) to calculate h_p . Nevertheless, the high transparency of the molded nanocomposites suggests that the agglomerates are few and sparsely dispersed. The lowest size limit of Mie scattering by colloidal inorganic nanoparticles is about 70 nm (144). Rayleigh scattering by ZnO nanoparticles in a transparent coating is low even for particles as large as 30 nm (145). The conditions for high transparency at high volume fraction exist when there is a uniform distribution of nanofillers and the nanofiller separation is less than $2a$ (145).

Closer inspection of the TEM images confirms that the largest clusters or agglomerates are 30–50 nm and the ZnO QDs remain separated by ~1 nm even at the most densely packed regions. There is also evidence to suggest that the ZnO QD interaction with polymer chains is significant even at distances greater than $2R_g$, beyond the distance required for polymer confinement (67-69). This phenomenon can be explained by the effect of transient interactions between surfaces and polymer chain segments, which retards the dynamics. The percolation of these local regions of slowed polymer chain segments determines the T_g of the system. These results suggest that the presence of aggregates in our model system do not influence our analysis as long as individual QDs remain dispersed and the size of the aggregates remain smaller than the critical distance where polymer dynamics is affected by the surface-polymer chain interactions. The successful application of the Long-Lequeux model to the ZnO/PMMA nanocomposites indicates that the model can be useful even in systems which show a distribution of interparticle distances. One possible explanation is that the overall T_g can be regarded as an ensemble average of the local T_g values of regions having different interparticle distances. This explanation allows the use of a geometrical average h_p to obtain the overall T_g for a highly uniform and well-dispersed nanocomposite with local variations.

Equation 3-4 can also be expressed as

$$T_g = T_{g,bulk} \left\{ 1 + \left(\frac{A}{h_p} \right)^\delta \right\} \quad 3-5$$

The exponent is defined as $\delta = 1/\nu = 1.14$, and A is related to B by $A^\delta = B$. Equation 3-5 is an analogue to the well-known equation for thin films with weakly adsorbing surfaces

(55). The parameter A can be defined as the characteristic length of the polymer and is related to the *cooperatively rearranging region* according to Adam and Gibbs (146). Dielectric spectroscopy studies of PS and PMMA (58, 61) yielded A values of 0.3–0.8 nm. The parameters $T_{g,bulk}$ and A derived from Equations 3-3 and 3-4 are listed in Table 3.1 for comparison. The characteristic length from our analysis fell within a range of 0.41–0.90 nm, which is consistent with the dielectric spectroscopy results and is similar to the Kuhn segments of PMMA (~0.9 nm) (147).

The Long-Lequeux model predicts that for a typical amorphous polymer like polystyrene (PS) or PMMA, a T_g increase of 50 – 60 K is expected for polymer films of several nanometers. This prediction is supported by experimental results of isotactic PMMA (148)(149), but is substantially greater than the increase observed in our data (~9 K at 6 nm). Our results more closely resemble those of other authors (55, 150). The wide variation of reported T_g increases can be explained by the configuration of adsorbed polymer layers on the inorganic surface, which strongly affects the observed T_g increase (151). For example, the ester groups of PMMA can form hydrogen bonds with the hydroxyl groups on the inorganic nanoparticle surface (141, 142), yielding configurations of trains, loops and tails (152). Formation of trains and loops requires multiple hydrogen bonds between the inorganic surface and a polymer chain. The ZnO QDs in the present study are covalently bonded to grafted-PMMA via silane molecules, which in turn interact with the polymer matrix via monomer-monomer attraction. Hydrogen bonding between the PMMA and ZnO surfaces is less likely due to the presence of a layer of silane molecules. Thus, we can consider the polymer configuration

on the ZnO surface to be purely of the tail type, which results in less constraint on polymer segmental motion compared to the scenarios described earlier and thus explains the lower T_g increase.

A salient feature of the Long-Lequeux model is the assumption of 3D percolation yielding the exponent value $\nu = 0.88$. Note that the values of ν measured here differ from the theoretical value. Multiple reasons were considered to explain the observed difference. The most probable reason was that polymer chains confined between nanoparticles do not percolate in 3D as assumed. Simulations have also shown that polymer thin films and PNCs can exhibit different characteristic ν values for the same percolation model (153). Even though this study was conducted using a 2D percolation model, the general conclusion is assumed to be applicable to a 3D system. Another possible reason stems from the fact that a distribution of interparticle distances exists in our model system. This distribution can affect the results in two ways. First, the estimation of h_p is imperfect and understandably affects the accuracy of our data. Second, different percolation modes may dominate at different interparticle distances. The behavior of our nanocomposite suggests the possibility of a combination of 2D and 3D modes of percolation, although systematic studies are required to support this assertion.

3.6 Conclusions

An inorganic/organic hybrid material has been synthesized that exhibits resistance to aggregation and segregation during repeated thermal treatments. We have exploited this unusual property to fabricate nanocomposites with well-controlled nanofiller contents

that show uniform dispersion of the nanofillers. Characterization of the T_g behavior of our nanocomposites reveals a surprising linear dependence of T_g on nanofiller content, unlike previous studies of similar nanocomposites. The ability to maintain good dispersion of the nanofillers at a wide range of nanofiller content facilitates this phenomenon. In addition, the absence of chemical crosslinks simplifies the analysis of T_g . This phenomenon has been rationalized using a physical model for polymer thin films.

We observed a power law dependence of T_g on interparticle distance and found that the measured characteristic length, A of the nanocomposites is consistent with known values. However, we also observed deviations from the model that can be explained by the unique characteristics of our nanocomposites. For example, a layer of organic silane covering each nanoparticle limited the interaction of polymer segments with the inorganic surface, resulting in a less than expected increase of T_g observed in our nanocomposites. The deviation of percolation exponent ν from theoretical predictions was attributed to intrinsic differences between PNCs and polymer thin films, the existence of a distribution of interparticle separations, and different percolation modes. These results demonstrate that T_g of a PNC can be controlled by simply adjusting the nanofiller content. According to a recent report, a remarkable increase of 30°C in T_g was observed (154) when 0.05 wt% of graphene sheets was mixed with PMMA. This shows that significant increase in T_g can be achieved under the proper conditions.

We have thus far presented the case that a quantitative model of polymer thin films can be applied to PNCs to explain its T_g behavior. However, this does not exclude

the possibility of other quantitative models that may also be equally successful in describing PNCs. It appears that with careful study, additional similarities between PNCs and polymer thin films may be discovered. It is thus not unreasonable to expect that further study into the underlying physics will lead to practical ways of engineering the T_g of nanocomposites. Our research provides a basis for the systematic study of such phenomena, with the ultimate goal of developing the capability to engineer T_g for all kinds of polymer nanocomposites.

CHAPTER IV

IRIDESCENCE OF α -ZrP NANOPATELETS IN ORGANIC SOLVENTS DUE TO LYOTROPIC MESOMORPHISM

4.1 Introduction

In this chapter, the observation of iridescence in oligomer-grafted α -ZrP ($\text{Zr}(\text{HPO}_4)_2 \cdot \text{H}_2\text{O}$) nanoplatelets with a diameter of 625 nm suspended in different polar aprotic solvents is described. The α -ZrP nanoplatelets were synthesized by a previously reported hydrothermal method (50). It is demonstrated that the color of the iridescence can be changed by simply adjusting the concentration of the suspended nanoplatelets. The observation of iridescence is attributed to the formation of lamellar phases with d -spacings of 140 to 240 nm under long range electrostatic repulsion in a low-ionic strength system aided by the presence of a brush layer grafted onto the nanoplatelets. Adjustable interlamellar distance of such a large magnitude has so far been exclusively observed in aqueous dispersions (37, 72-74, 155, 156).

4.2 Methods and Materials

4.2.1 *Materials for Synthesis*

Zirconyl chloride ($\text{ZrOCl}_2 \cdot 8\text{H}_2\text{O}$, 98%, Aldrich), phosphoric acid (85%, EM Science), and acetone (ACS grade, EMD) were used as received. A commercial polyoxyalkyleneamine, Jeffamine M1000 with a reported average molecular weight of 1000 gmol^{-1} (Huntsman Chemical) were used to exfoliate α -ZrP.

4.2.2 Preparation and Exfoliation of α -ZrP

A sample of 4.0 g $\text{ZrOCl}_2 \cdot 8\text{H}_2\text{O}$ was mixed with 40.0 mL 12.0 M H_3PO_4 and sealed into a polytetrafluoroethylene-lined pressure vessel and heated to 200°C for 24 h. After the reaction, the product was collected by centrifugation, followed by washing by deionized water and centrifugation two times. The product was collected and dried at 65°C for 24 h. The dried product was ground into fine powder with a mortar and pestle.

A typical exfoliation procedure is described here. A sample containing 0.5 g of ZrP was weighed and dispersed in 25 mL of acetone by sonication for 10 min. A 0.6 g mL^{-1} solution of M1000 in acetone was prepared. A volume of 17.7 mL of M1000 solution was added dropwise to the stirring α -ZrP dispersion. This dispersion was allowed to stir for 4 h. The dispersion was sonicated for 10 min followed by centrifugation at 10,000 rpm for 15 min. The sediment was removed leaving a clear suspension containing only exfoliated α -ZrP and excess polyoxyalkyleneamine. The clear suspension was centrifuged at 20,000 rpm for 3 h and the exfoliated α -ZrP was collected as a gel while the excess polyoxyalkyleneamine remained in the supernatant. The exfoliated α -ZrP was redispersed at different concentrations in various organic liquids.

4.2.3 UV-vis Spectroscopy

Reflectance spectroscopy was performed using a Shimadzu 3600 UV-vis-NIR spectrophotometer. The ZrP suspensions were transferred into a cuvette (25.4 mm \times 15.0 mm \times 1.3 mm, 2.0 mm optical path length) made from two thin rectangular glass plates (Fisher-Scientific) that were double-sealed by solvent-resistant epoxy (Permapoxy 5

min) and silicone (Loctite RTV587 Blue). White BaSO₄ powder was used as a standard for analyzing the reflectance of the samples.

4.2.4 Electron Microscopy

Transmission electron micrographs (TEM) were obtained on a JEOL JEM –1200Ex.

Field emission electron microscopy (FESEM) was performed by a JEOL JSM-7500F unit using the Gentle Beam-Lo mode.

4.2.5 Atomic Force Microscopy

Tapping-mode atomic force microscopy was carried out by a Bruker Dimension Icon AFM. The image was acquired in air using a MPP-21120-10 probe (Bruker; tip radius, nominal force constant and resonance frequency are 8 nm, 15°, 3 Nm⁻¹ and 75 kHz, respectively). Highly diluted solutions of nanoparticles were dropped onto a Si wafer cleaned previously by piranha solution (3:1 37% sulfuric acid and 30% hydrogen peroxide mixture; note: piranha solution is highly corrosive and exothermic when mixed with organic matter, proper safety precautions should be taken during handling). The samples were dried at room temperature before scanning.

4.2.6 Ultra Small-angle X-ray Scattering

The liquid crystalline structure of the samples was determined by small-angle x-ray scattering (SAXS), which was performed at the Japan Synchrotron Radiation Research Institute (JASRI) Spring-8 facility located in Hyogo, Japan. Measurement was taken at the BL03XU beam line (157) using an incident X-ray with a wavelength of 0.100 nm. Scattered X-rays were detected using an imaging plate and a 4152 mm sample-to-detector distance calibrated by the 001 diffraction peaks of silver behenate. The 2D

scattering patterns were recorded on imaging plates (Fuji Film Co.) and exposure time was 1.0 or 2.0 s. The scattering vector is defined by $q = (4\pi/\lambda) \sin \theta$, where λ is the wavelength of the X-rays, and 2θ is the angle between the incident X-ray beam and the scattered X-rays.

4.3 Oligomer-grafted α -ZrP Nanoplatelets

To achieve iridescence in non-aqueous solutions, we chose highly polar aprotic solvents to enable charge stabilization at the surface of the nanoplatelets. Charge separation is required for long range electrostatic repulsion which is negligible in nonpolar solvents without the mediation of surfactants (158). The experiments done by Kleshchanok *et al.* (38) suggests that this approach alone may not provide sufficient repulsion between nanoplatelets to ensure a large enough d -spacing for iridescence to appear. Essentially, a d -spacing larger than 125 nm (which was the reported value for lamellar solutions of nanoplatelets by Kleshchanok *et al.*) is required to produce iridescence. To remedy this problem, we selected charged oligomeric molecules to graft onto the surface of nanoplatelets. A sufficiently long oligomer will form dense, thick brushes on the nanoplatelets, increasing the effective thickness of the nanoplatelets and lowering the local dielectric constant. There are two possible effects which may result in a larger d -spacing. First, lowering the local dielectric constant can increase the Debye screening length κ^{-1} by reducing the concentration of free ions surrounding each nanoplatelet (Mechanism I Figure 4.1). This is shown explicitly according to the equation,

$$\kappa^{-1} = \frac{1}{\sqrt{4\pi Bn}}$$

5-1

B is the Bjerrum length given by $e^2/\epsilon kT$, where e is the electronic charge, k is the Boltzmann constant, T is the absolute temperature, ϵ is the dielectric constant of the solvent and n is the concentration of free ions in solution. This effect has been shown to increase interparticle distances between polystyrene spheres when the dielectric constant is lowered by adding organic solvents to deionized water (159). Second, free oligomers may be absorbed onto the brush layer, further increasing the thickness of the nanoplatelet and thus increasing d -spacing (mechanism II Figure 4.1).

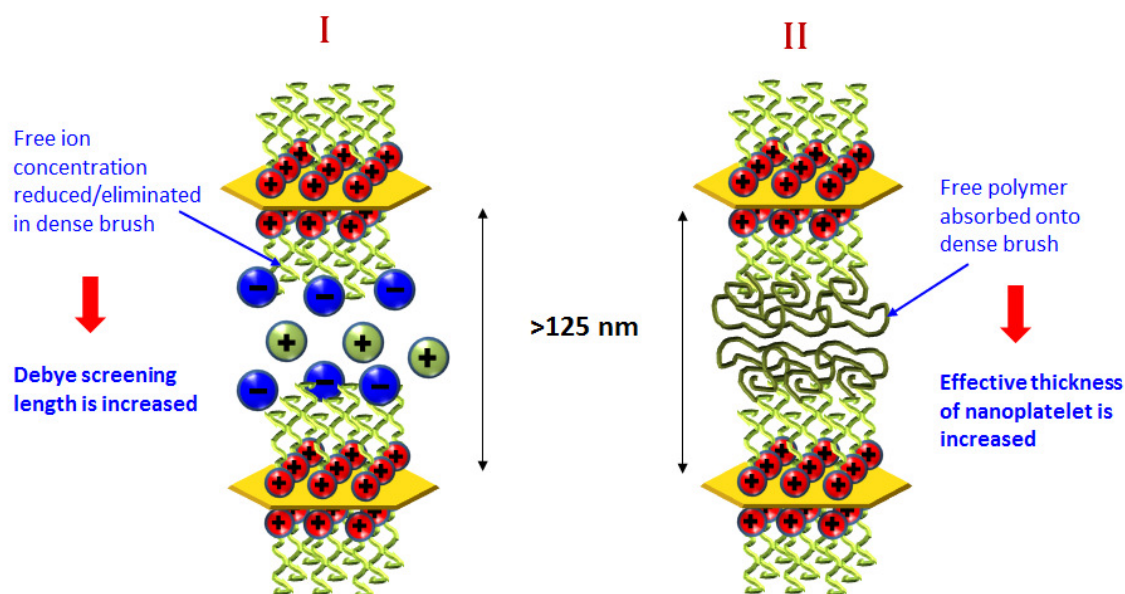


Figure 4.1 Two possible mechanisms to increase interlamellar spacing.

We estimate that for butyronitrile (refractive index $\eta = 1.384$), a d -spacing of around 145 nm is required for iridescence to occur in the violet wavelength ($\lambda_{max} = 400$ nm), according to the equation ($d = \lambda_{max} / 2\eta$) proposed by Platz *et al.* (72) α -ZrP

nanoplatelets synthesized through a hydrothermal method (50) yielded nanoplatelets with a majority of irregular hexagonal geometry. Exfoliation was carried out using a polyoxyalkyleneamine, Jeffamine M1000 (Huntsman Chemicals, MW~1000 gmol⁻¹, hereafter referred to as M1000). Polyoxyalkyleneamines have been shown to be effective in intercalating and exfoliating α -ZrP nanoplatelets (160) in highly polar aprotic solvents such as acetone. In addition, the primary amine terminal group provides a cationic charge to the nanoplatelet surface necessary for long range electrostatic repulsion. Grafting proceeds *via* cationic exchange of the primary amine group to the phosphate group on the α -ZrP nanoplatelets. The dielectric constant of M1000 is not known. Nevertheless, since it consists of mostly polyethylene glycol (PEG) segments (83% wt) with a minority of polypropylene glycol (PPG) segments (17% wt), a reasonably close assumption can be made by comparing an analogous PEG oligomer, which has a dielectric constant around 10 (161). This value is lower than the dielectric constants of the solvents used in this study which range from 20 to 37. A process of centrifugation and redispersion removed unexfoliated nanoplatelets and excess M1000. The hydrothermal method yielded irregular hexagonal nanoplatelets around 1 μ m in the experiments by Sun *et al*, which stands in contrast to the average size of 625 ± 283 nm reported here (Figure 4.2a & b). We attribute the size reduction to the fact that smaller nanoplatelets were preferentially exfoliated by M1000 while the larger nanoplatelets were removed through centrifugation.

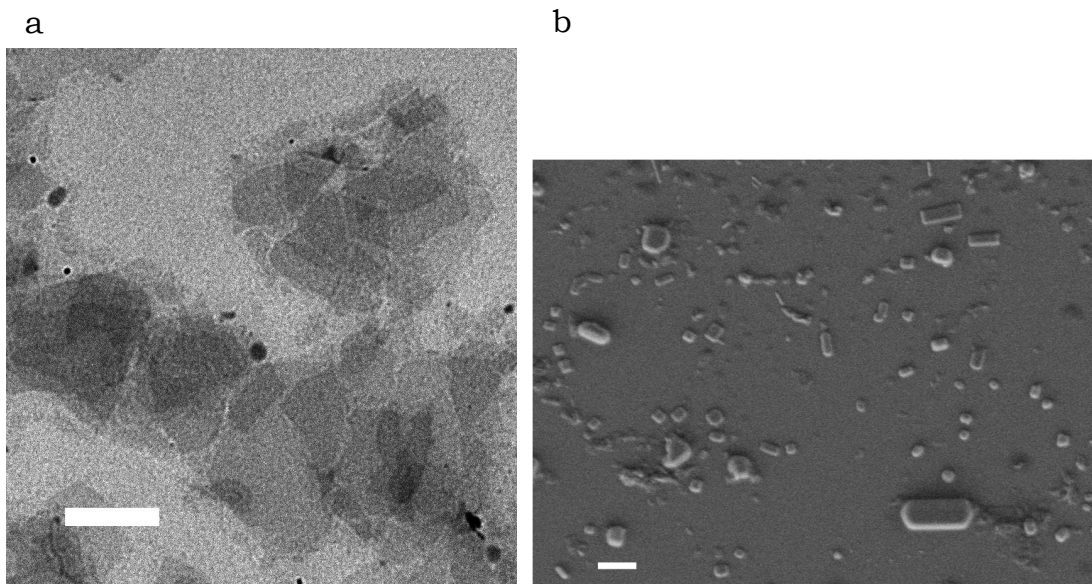


Figure 4.2 (a) Transmission electron micrograph of irregular hexagons of α -ZrP nanoplatelets. Average size is 625 ± 283 nm measured over 266 particles. Scale bar indicates $0.5 \mu\text{m}$. (b) Field emission scanning electron micrograph of α -ZrP nanoplatelets deposited on a silicon wafer. Scale bar indicates $1 \mu\text{m}$.

4.4 Iridescence of α -ZrP Nanoplatelets in Organic Solvents

A series of α -ZrP/butyronitrile (dielectric constant = 24.8) solutions were prepared at different concentrations. The reflectance spectra of these solutions display shifting sharp peaks representing colors changing from violet to red as the concentration of nanoplatelets was reduced (Figure 4.3a). Photographic images (Figure 4.3b) of the solutions enclosed in glass cells made in-house demonstrate the brilliant colors displayed by the suspended photonic crystals. Similar phenomena were observed in solutions of acetone (dielectric constant = 21.0), acetonitrile (dielectric constant = 36.6) and propionitrile (dielectric constant = 29.7). The lamellar structure of the solutions was confirmed by USAXS, shown in Figure 4.3c, where the d -spacing was reported as

130nm. Due to solvent loss during transportation of the solution to the synchrotron facility, this d -spacing does not reflect the true value of the solutions. ZrP concentration ranges from 0.40 to 1.46 wt%, resulting in a shift of reflectance peak λ_{max} from 658 to 332 nm (Figure 4.4a). ZrP d -spacing was approximated using the Platz equation (*vide supra*) and was found to exhibit a linear dependence to the reciprocal of nanoplatelet volume fraction, $1/\phi$ (Figure 4.4b). This result is typical of lamellar phases as $d = t/\phi$, where t is the thickness of nanoplatelets (41).

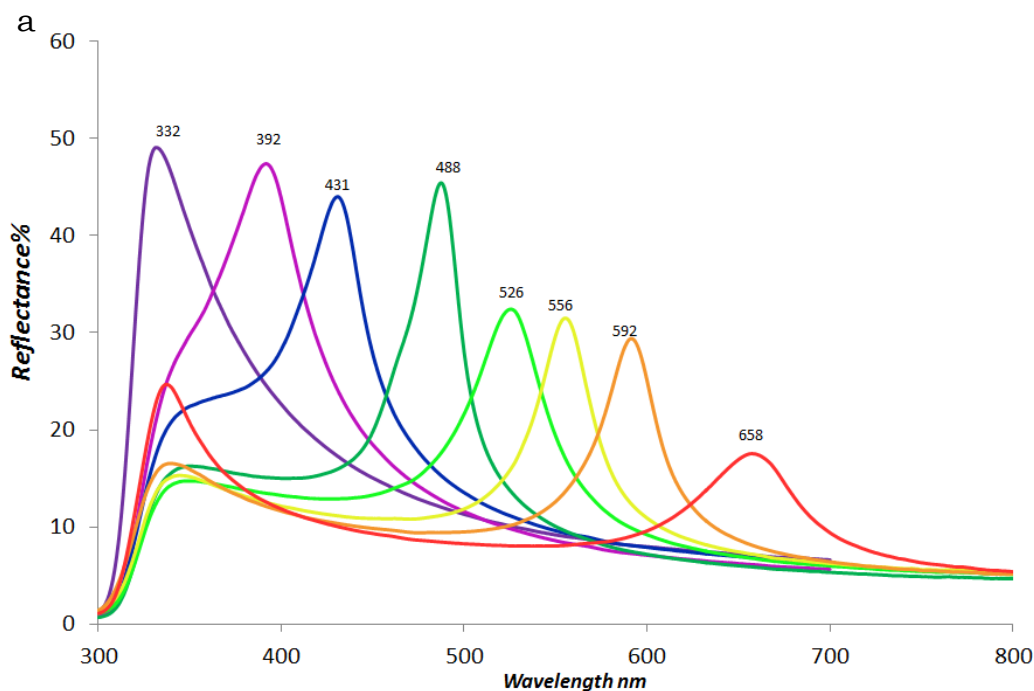


Figure 4.3 (a) Reflection spectra of 625 nm α -ZrP nanoplatelets in butyronitrile at various concentrations. Reflectance peak shifts from red to ultraviolet as concentration of nanoplatelets increases. (b) Photographic images of butyronitrile solutions containing α -ZrP nanoplatelets demonstrating colors shifting from violet to red as concentration decreases from left to right. (c) USAXS 2D diffractogram confirms the lamellar structure of the solutions, displaying a d -spacing of 130 nm.

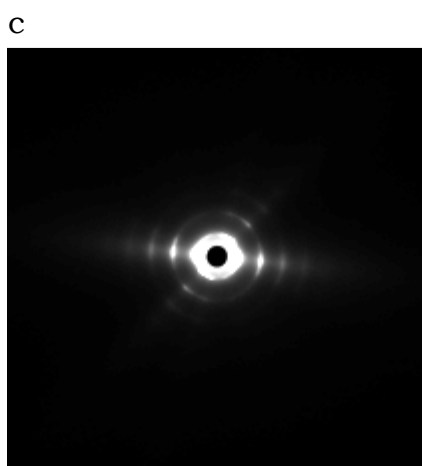
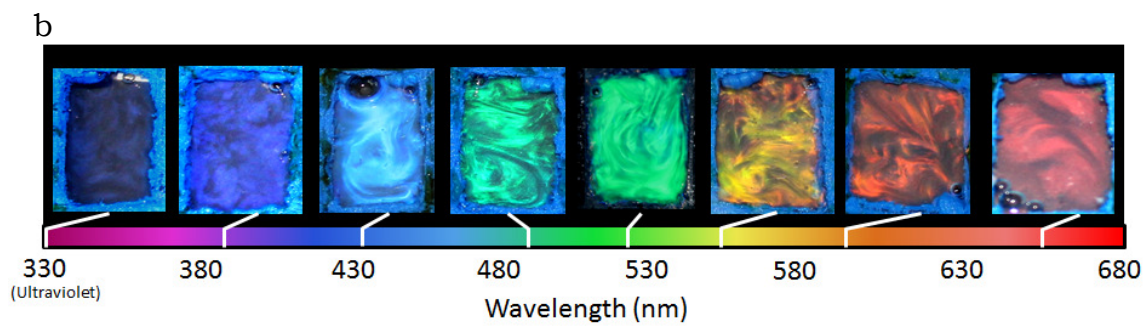


Figure 4.3 Continued.

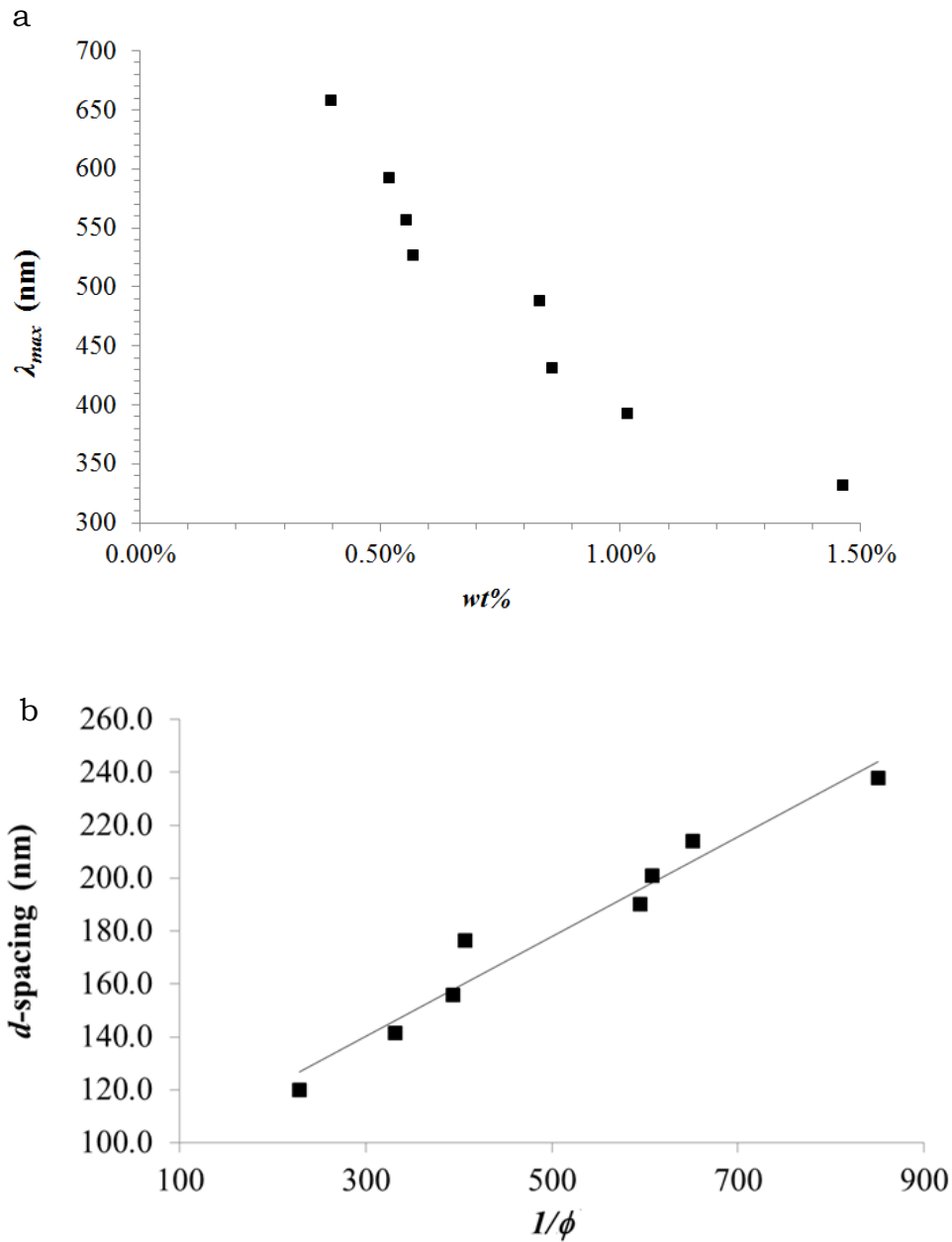


Figure 4.4 (a) Peak positions (λ_{max}) of reflectance spectra against ZrP wt%, demonstrating the dependence of iridescence color on ZrP concentration. (b) d -spacing shows a linear dependence on $1/\phi$, as expected from a lamellar phase in solution. d -spacing was calculated from $d = \lambda_{max}/2\eta$.

4.5 Lyotropic Mesomorphism of α -ZrP Nanoplatelets in Organic Solvents

The occurrence of lyotropic mesomorphism is confirmed by observing the solution under cross-polarized light. Under white light, an acetone solution of α -ZrP nanoplatelets displays a brilliant blue color (Figure 4.5a). Under cross-polarized light, the same solution displays birefringence fringes (Figure 4.5b) that coincide with the features seen under white light. Reflectance optical microscopy (Olympus BX 60) of a green α -ZrP/acetone solution reveals the presence of fine strands and globules which are the origin of iridescence (Figure 4.5c & d). These structures can range from 10 to 70 μm in length. However, the widths of these structures are fairly constant at 5 μm which suggests that the stacking of lamellae is responsible. Assuming that the d -spacing is 200 nm, we estimate that 25 layers of lamellae are stacked in each structure.

Atomic force microscopy (AFM) was performed on α -ZrP nanoplatelets that were deposited on a silicon wafer by slow evaporation at room temperature of a highly diluted α -ZrP/butyronitrile solution (~ 1 ppm). A thick coat of polymer was observed on a hexagonal nanoplatelet of 760 nm in size (Figure 4.6a). The phase image (Figure 4.6b) reveals a stiff phase at the base of the structure (thickness ~ 2 nm) which is attributed to the α -ZrP monolayer and a soft phase forming a coat (thickness ~ 70 nm) (Figure 4.6c & d). The measured thickness of the nanoplatelet is larger than a monolayer of α -ZrP crystal (thickness ~ 0.68 nm (36, 50, 162)). This can be explained by the presence of a stiffer, dense brush layer on top of the α -ZrP monolayer which significantly increases the thickness of the nanoplatelet. The AFM results appear to be consistent with the hypothesis that each nanoplatelet is covered by a dense brush layer followed by a loosely

packed absorbed polymer coat. Analysis of several nanoplatelets shows that all of them are covered by a soft polymer coat. The thickness of this coat shows considerable variability and a more complete statistical analysis in future studies is needed for an accurate assessment of polymer coat thickness.

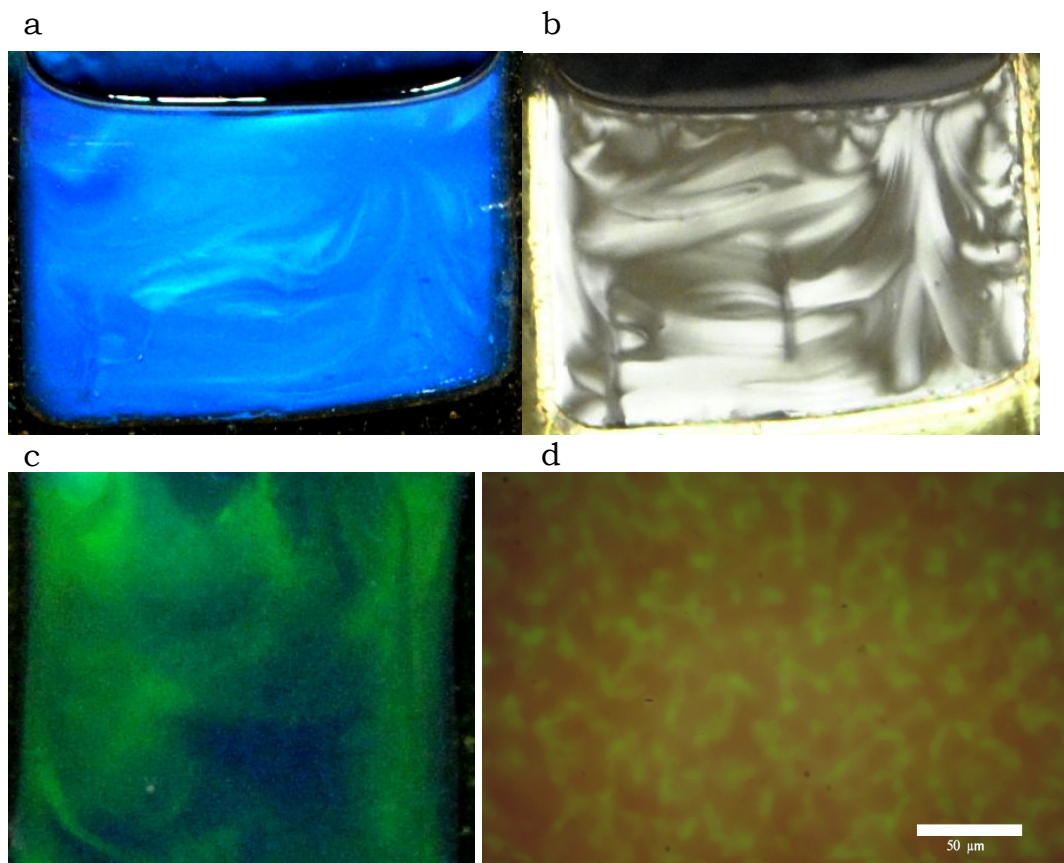


Figure 4.5 (a) Photograph of an acetone solution containing α -ZrP nanoplatelets enclosed in a glass cell under white light displays brilliant blue color. (b) Photograph of same solution under cross-polarized light revealing birefringent fringes that coincide with the features observed under normal light. The observation of birefringence is due to the presence smectic phases of nanoplatelets. (c) Photograph of an acetone solution containing α -ZrP nanoplatelets enclosed in a glass cell under white light displays a brilliant green color. (d) Reflectance optical microscopy reveals the origin of iridescence to be in the fine strands or globules suspended in the liquid. The iridescent strands or globules range from 10 μm to about 70 μm in length and about 5 μm in width.

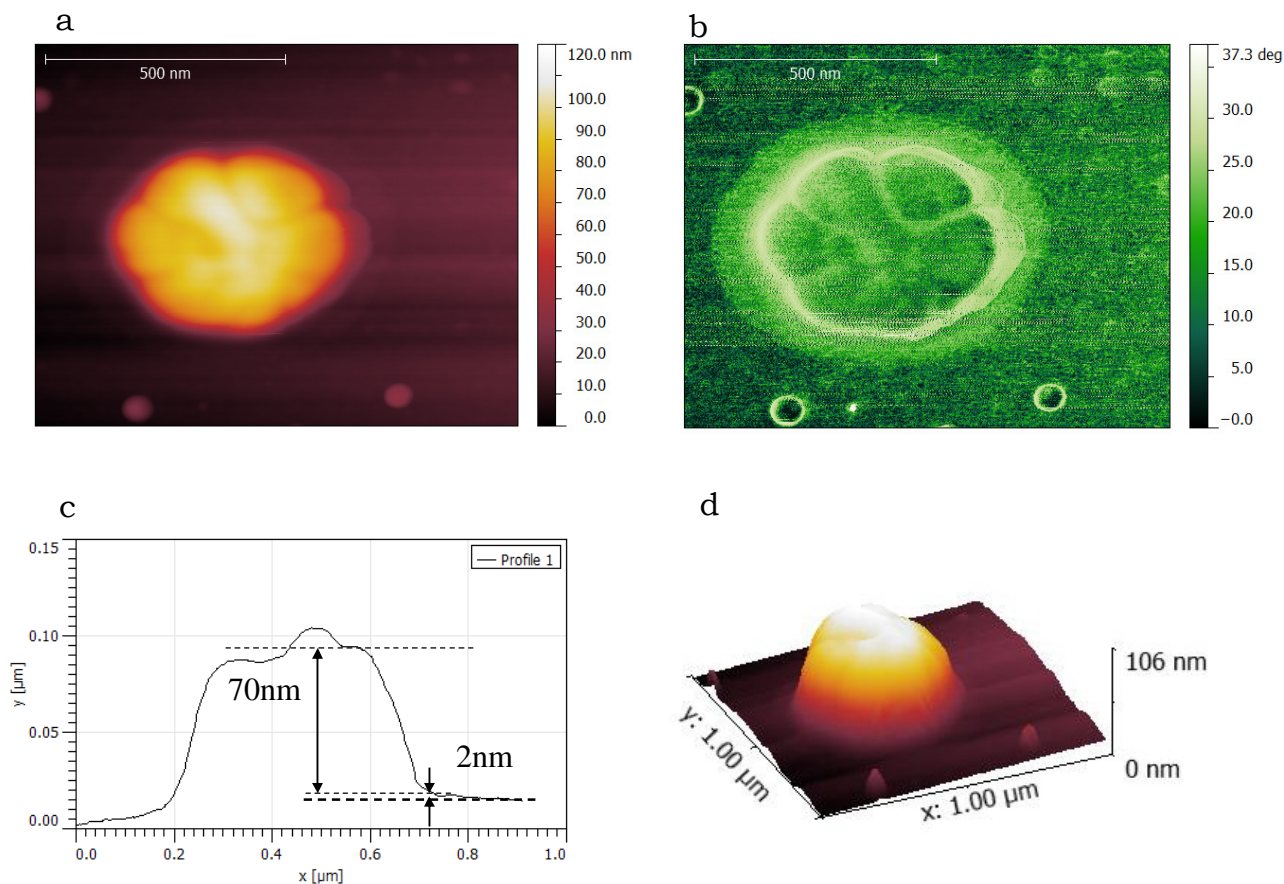


Figure 4.6 Atomic force micrographs of single ZrP nanoplatelet (~760 nm) on silicon wafer. (a) Height image shows a layer of polymer covering the nanoplatelet. (b) Phase image clearly shows the softer polymer lies on top of a stiffer hexagonal nanoplatelet which forms the base. (c) Profile of the nanoplatelet indicates the thickness of the polymer is 70 nm and the nanoplatelet is 3 nm. (d) 3D visualization of the polymer-coated nanoplatelet.

4.6 Conclusions

Our experiments show that it is possible to induce the formation of photonic crystals in polar aprotic solvents *via* lyotropic mesomorphism of nanoplatelets. Iridescence is observed due to Bragg reflections in the visible wavelengths by the lamellar phase of nanoplatelets. The expanded *d*-spacing of the lamellar phase beyond 125 nm allows for

the wavelength of the reflected light to be tuned simply by adjusting the concentration of the nanoplatelets. The grafting of charged oligomeric species on the nanoplatelet proves to be the key modification that allows for such large d -spacings in non-aqueous solvents. We propose that the oligomers act through two mechanisms, 1) the Debye screening length is extended as a result of lower free ion concentration surrounding each nanoplatelet due to the presence of a brush layer, and 2) the absorption of a thick polymer coat on the brush layer pushes the interlamellar distance further apart. Further study is required to clarify the relative importance of the two proposed mechanisms. As a concluding remark, this study demonstrates a new route to manipulating mesomorphic structures of 2D crystals in a non-aqueous environment.

CHAPTER V

SPRAY-COATABLE SMECTIC 2D CRYSTALS/EPOXY FILMS

5.1 Introduction

Liquid crystalline phases of 2D crystals are typically achieved via the electrostatic repulsion of the charges that exist on the surface of each nanoplatelet in aqueous solutions (37). The liquid crystalline order of such solutions can be preserved in solid state by freeze drying (163), a process which is not easily scalable for manufacturing, in addition to the fact that the solid films are unlikely to survive regular wear and tear. The seminal work of Lekkerkerker *et al.* (35, 81) showed that sterically stabilized nanoplatelets can also exhibit liquid crystalline phases. This discovery allows for the study of mesomorphic 2D crystals in organic solvents, which is in many ways more suitable for commercial processes. One crucial advantage is the ability to incorporate common organophilic polymers. Sterically stabilized nanoplatelets mixed with an appropriate pre-polymer or polymer preserves the mesomorphic structure of the nanoplatelets after the solvent is removed. A mixture of oligomer-grafted nanoplatelet/polymer in a solution can be delivered through a spray-coating method to form a continuous film on the substrate (Figure 5.1a & b). Subsequent drying and removal of solvent induces self-assembly of smectic phase in the film (Figure 5.1c). The film can be further stabilized by curing to form permanent mesoscale structures encased in a robust coat of epoxy (Figure 5.1d). This fast, simple process of delivering nanoplatelets to a substrate allows the final film to retain the liquid crystalline order of

the 2D crystals. The usefulness of the resultant mesomorphic 2D crystal films is demonstrated by measuring the oxygen transmission rate of polyimide films coated with the smectic 2D crystal/epoxy nanocomposite, where permeability is significantly reduced compared to the neat epoxy film. The effectiveness of the films is attributed to the fact that any small gas molecule is forced to traverse a tortuous path to reach the other side of the film, as the nanoplatelets are essentially impenetrable. This concept is illustrated in Figure 5.1e, where the nanoplatelets self-assemble into smectic layers with regular interlayer distance d , and a probable path of a gas molecule is traced by a black arrowed line.

In general, the concept of nanoplatelets sterically stabilized by oligomers in combination with a pre-polymer or polymer to fix the mesomorphic structure in the solid state is applicable to 2D crystals, and possibly 1D rigid rods. Using the spray-coating technique allows for fast, efficient application of functional coatings under ambient conditions onto a substrate potentially makes this a very attractive method to create multilayer functional coatings reminiscent of hierarchical structures commonly observed in biology (164, 165). This technology is relevant to creating functional coatings with properties including thermal and electrical conductivity, flame retardancy, gas barrier membrane, corrosion protection or catalytic coatings.

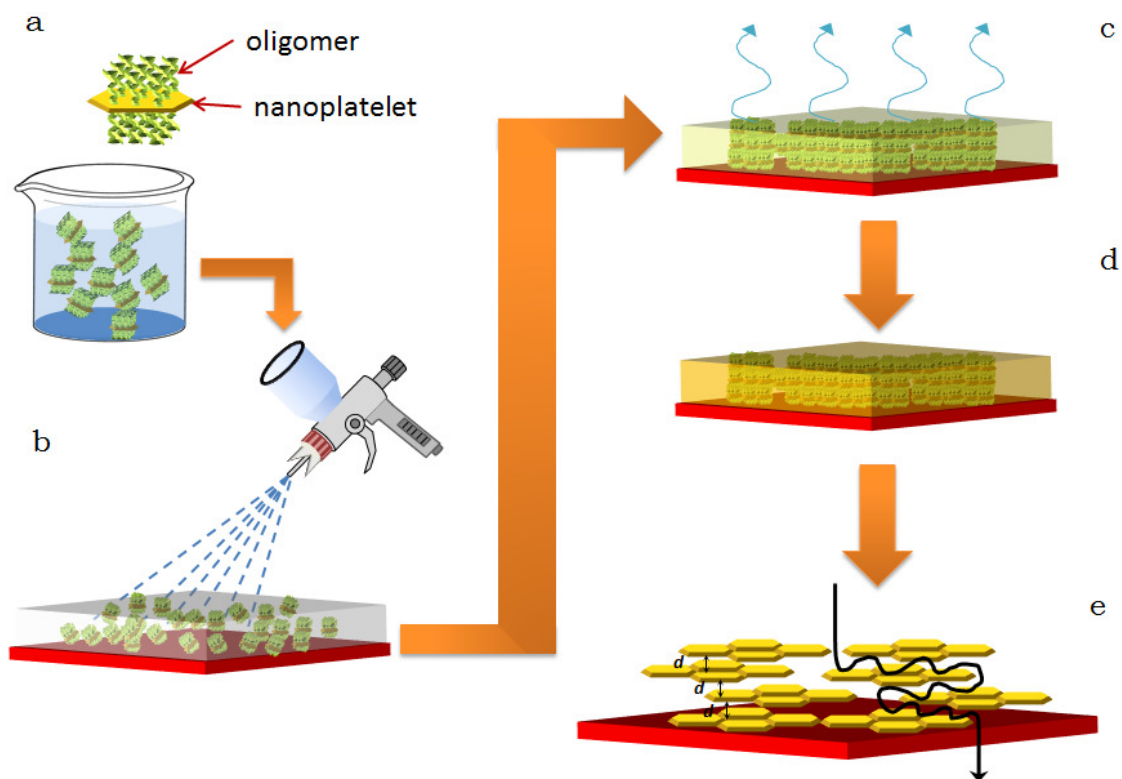


Figure 5.1 Process of spray-coating smectic 2D crystals /epoxy films. (a) Oligomer-grafted nanoplatelets is dispersed in a solution with epoxy pre-polymers and curing agent. (b) Solution is sprayed onto a polyimide or glass substrate. (c) Coated substrate is dried, nanoplatelets self-assemble into smectic phases as solvent is evaporated. (d) Smectic 2D crystals/epoxy film is cured, forming a robust coat. (e) Oligomer and epoxy omitted from schematic for clarity. Schematic illustrates the concept of a tortuous path that a gas molecule has to traverse through a smectic arrangement of nanoplatelets aligned parallel to a substrate to arrive at the other side of the barrier film. The interlayer distance d is constant between each layer. The black arrowed line traces a probable diffusion path of a gas molecule.

5.2 Methods and Materials

5.2.1 *Materials for Synthesis*

Zirconyl chloride ($\text{ZrOCl}_2 \cdot 8\text{H}_2\text{O}$, 98%, Aldrich), phosphoric acid (85%, EM Science), and acetone (ACS grade, EMD) were used as received. A commercial polyoxyalkyleneamine, Jeffamine M1000 with a reported average molecular weight of 1000 was received as a gift from Huntsman Chemical. Bisphenol F epoxy (Epon 862) and Epikure W curing agent were purchased from Momentive.

5.2.2 *Preparation and Exfoliation α -ZrP*

This procedure produces nanoplatelets of nominal size 100 nm. A sample of 20.0 g $\text{ZrOCl}_2 \cdot 8\text{H}_2\text{O}$ was refluxed with 200.0 mL 3.0 M H_3PO_4 in a Pyrex glass flask at 100 °C for 24 h. After the reaction, the products were washed and collected by centrifugation three times. Then, the α -ZrP was dried at 65 °C for 24 h. The dried α -ZrP was ground with a mortar and pestle into fine powder.

Exfoliation was carried out using M1000. A sample containing 0.5 g of α -ZrP was weighed and dispersed in 25 mL of acetone by sonication for 30 min. A 0.6 gmL^{-1} solution of M1000 in acetone was prepared. A volume of 2.77 mL of M1000 solution was added dropwise to the stirring α -ZrP dispersion. This dispersion was allowed to stir for 4 h. The dispersion was sonicated for 60 min followed by centrifugation at 10,000 rpm for 30 min in PTFE tubes (Nalgene Oakridge, Thermo Scientific). The sediment was removed leaving a clear suspension containing only exfoliated α -ZrP and excess polyoxyalkyleneamine. The clear suspension was centrifuged at 20,000 rpm for 2 h (Sorvall Evolution RC, Thermo Scientific) and the exfoliated α -ZrP was collected as a

gel while the excess polyoxyalkyleneamine remained in the supernatant. The exfoliated α -ZrP was redispersed in 25 mL of acetone.

5.2.3 Preparation of α -ZrP/Epoxy Bulk Nanocomposites

Bisphenol F epoxy was dissolved in 12 mL acetone and added dropwise to the stirring exfoliated α -ZrP dispersion. The dispersion was allowed to stir for 4 h and the solvent was removed in a rotary evaporator at an elevated temperature forming a dark yellow, clear, viscous liquid. Curing agent W (26.4 phr) was added to the α -ZrP/epoxy liquid, heated to 80°C and mixed in a rotary evaporator. The liquid was poured into a vertical glass mold and cured at 80°C 100 min, 120°C 120 min and 177°C 120 min.

5.2.4 Preparation of α -ZrP/Epoxy Solutions

This procedure yields a nanocomposite with 10 wt% α -ZrP. 2.33g of Bisphenol F epoxy (EPON 862, Momentive) was dissolved in 5 mL of acetone to form a clear solution. The epoxy solution was added dropwise to the stirring dispersion containing 0.5 g of α -ZrP. This dispersion was allowed to stir for 4 h. The solution was concentrated to obtain a 20 wt% solution. 0.62 g of curing agent W (Epikure W, Momentive) was added to the solution and homogenized by stirring.

5.2.5 Spray-Coating of α -ZrP/Epoxy onto Substrates

The α -ZrP/Epoxy solution was loaded into an airbrush style spray-gun (Master Airbrush G444-SET, needle nozzle 0.5 mm and Royal Mini Air Compressors, TC-20B, flow rate 23L/min) and sprayed onto a substrate of polyimide (PI) film (Apical, Kaneka) with a thickness of 25 μ m. The solution was sprayed manually multiple times onto the substrate to achieve the desired film thickness. The spray-coated PI film was dried in an oven at

40°C for an hour. The nanocomposite was cured at 120°C 2 h, 177°C 4 h and 200°C 4 h. The thicknesses of the cured nanocomposite coats were controlled to be at 7.0 ± 1.0 μm . The thicknesses of the spray-coated films were measured using a dial gauge (Mitutoyo) where an average of six readings was taken.

5.2.6 Evaluation of Oxygen Transmission Rate

Oxygen transmission rate (OTR) of the films was evaluated using a MOCON OX-TRAN 2/21 in accordance to ASTM D3985. A total of four spray-coated films were evaluated for OTR at relative humidities of 0%, 50% and 90% at 23°C for 4.4 vol% α -ZrP/epoxy coating. At all other concentrations, OTR was evaluated at relative humidity of 50% at 23°C with two films for each concentration.

5.2.7 Optical Microscopy

Cross-sections of coated films were prepared by mounting cut films onto glass microslides by clear epoxy (Permapoxy 5 min) and polished with abrasive paper to a smooth finish with a thickness of about 50 μm . Transmission optical microscopy and cross-polarized microscopy were performed using an Olympus B60.

5.2.8 Rheology

The rheology of smectic epoxy liquid was measured using an Ares-G2 rheometer (TA Instruments) using a 50.0 mm, 0.02 rad cone and plate fixture made of stainless steel.

5.2.9 Thermogravimetric Analysis

The mass fraction of α -ZrP in epoxy was determined by thermogravimetric analysis (TGA) using a TA instruments Q500. The samples were heated to 900°C in air at a heating rate of 20°C per min and held at 900°C for 60 min. The solid residue that

remains is zirconium pyrophosphate (ZrP_2O_7), which can be converted to the equivalent α -ZrP mass fraction via stoichiometric calculations. Mass fraction is converted to volume fraction $v_i = m_i/\rho_i / \sum m_i/\rho_i$, where m_i and ρ_i are the mass fraction and density of each component, respectively, in the mixture or nanocomposite.

5.2.10 Atomic Force Microscopy

Tapping-mode atomic force microscopy was carried out by a Bruker Dimension Icon AFM. The image was acquired in air using a MPP-21120-10 probe (Bruker; tip radius, nominal force constant and resonance frequency are 8 nm, 15°, 3 Nm^{-1} and 75 kHz, respectively). Highly diluted solutions of nanoparticles were dropped onto a Si wafer cleaned previously by piranha solution (3:1 37% sulfuric acid and 30% hydrogen peroxide mixture; note: piranha solution is highly corrosive and exothermic when mixed with organic matter, proper safety precautions should be taken during handling). The samples were diluted to 1 ppm in butyronitrile, dropped onto the cleaned Si wafer and dried at room temperature before scanning.

5.2.11 Transmission Electron Microscopy and Tomography

Transmission electron micrographs (TEM) were obtained on a JEOL JEM -1200 Ex. Ultrathin sections were prepared using a Reichert-Jung Ultracut E microtome. TEM tomography (TEM-T) experiments were carried out with a JEM2200FS (JEOL, Ltd., Japan) equipped with a eucentric specimen stage and an in-column electron energy loss spectrometer, which allowed only elastically scattered electrons to produce each projection. The acceleration voltage was 200 kV. Dual-axis electron tomography was used to obtain accurate 3D images from the anisotropic structure (166). In TEM-T, a

series of tilted transmitted images (projections) are taken and is used to reconstruct tomograms on the basis of computerized tomography (CT). The tomograms are then stacked to generate a 3D reconstructed image.

5.2.12 Wide-angle X-ray Scattering

Wide-angle x-ray scattering experiments were performed on a Bruker D8-Focus Bragg-Brentano x-ray powder diffractometer at the Texas A&M University X-ray diffraction laboratory (Cu K $_{\alpha}$ radiation, $\lambda = 1.54056 \text{ \AA}$).

5.2.13 Grazing-incidence and Small-angle X-ray Scattering

Grazing-incidence small-angle x-ray scattering (GISAXS) experiments were performed on a Rigaku S-Max 3000 unit at the University of Houston. Data was collected at a grazing incidence angle of 0.05 degrees (Cu K $_{\alpha}$ radiation, $\lambda = 1.54056 \text{ \AA}$). Small-angle x-ray scattering (SAXS) experiments was performed at the Japan Synchrotron Radiation Research Institute (JASRI) Spring-8 facility located in Hyogo, Japan. Measurement was taken at the BL40-B2 beam line (157) using an incident X-ray with a wavelength of 0.07 nm. Scattered X-rays were detected using an imaging plate and a 2237 mm sample-to-detector distance calibrated by the peaks of collagen. The scattering vector is defined by $q = (4\pi/\lambda) \sin \theta$, where λ is the wavelength of the X-rays, and 2θ is the angle between the incident X-ray beam and the scattered X-rays.

5.3 Oligomer-grafted α -ZrP Nanoplatelets

α -Zirconium phosphate ($\text{Zr}(\text{HPO}_4)_2 \cdot \text{H}_2\text{O}$) has a layered crystalline structure and functions as an ion exchanger (167). It is studied as a potential material for use as

catalysts (168) , drug delivery agents (169), proton conductors (170) and nanofillers (171) among other uses. The ability of α -ZrP to undergo cationic exchange with amines makes it a convenient material for the manufacture of 2D crystals with large aspect ratios (50). α -ZrP serves as a model for other materials that also exist as layered crystalline structures which are amenable to manipulation through colloidal methods. α -ZrP nanoplatelets with average size 100 ± 51 nm (Figure 5.2a) were synthesized via a hydrothermal method according to Sun *et al.* (50). The aspect ratios $\alpha = D/t$, where D is the diameter and t the thickness, of these nanoplatelets are nominally 147, assuming $t = 0.68$ nm (see below).

The oligomers used in this study are monoamine polyoxyalkyleneamines. Monoamine polyoxyalkyleneamines have been shown to be effective in intercalating and exfoliating α -ZrP nanoplatelets in highly polar aprotic solvents such as acetone (160). In addition, the single primary amine terminal group provides a cationic charge to the nanoplatelet surface necessary for long range electrostatic repulsion in solution. Modification proceeds *via* cationic exchange of the single primary amine group to the phosphate group on the α -ZrP nanoplatelets. Polyoxyalkyleneamines were selected due to their affinity to epoxy pre-polymers, where they are commonly used to modify viscosity of epoxy pre-polymers and glass transition temperature and Young's modulus of the cured epoxy. A range of molecular weights of polyoxyalkyleneamine are available commercially. In this study, polyoxyalkyleneamine of weight-average molecular weight about 1000 (Jeffamine M1000, Huntsman Chemical) were selected, which was expected to allow liquid crystalline phases of the nanoplatelets to manifest easily based on

previous reports (35, 81). Atomic force microscopy performed on α -ZrP nanoplatelets grafted with oligomers dried from solution at room temperature (see Method) is shown to be covered by a layer of soft material (Figure 5.2b & c). This soft layer is as thick as 10 nm which is too large to be due to a monolayer of oligomer, suggesting that a significant amount of free oligomer is absorbed onto the nanoplatelet. The thickness of the nanoplatelet lies in the range of 0.5~0.7 nm, in close agreement with the expected value of 0.68 nm from crystallography studies (162).

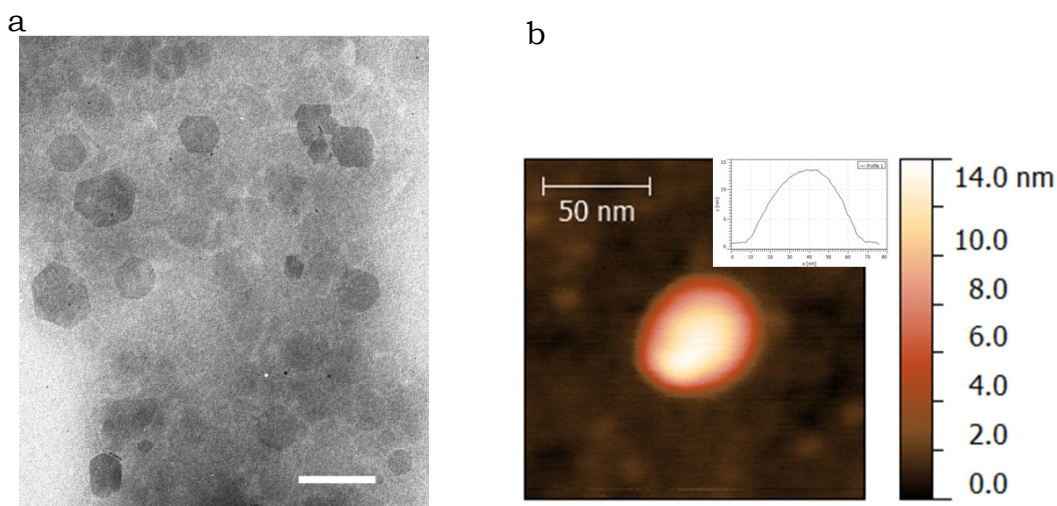
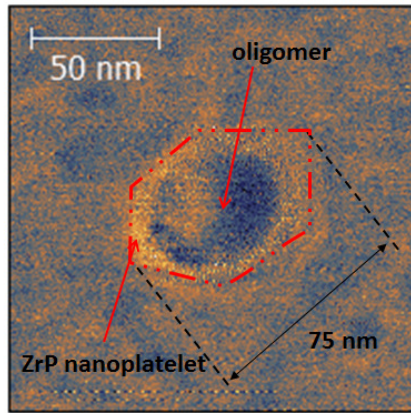


Figure 5.2 (a) Transmission electron microscopy of α -ZrP nanoplatelets with average size of 100 ± 51 nm. Values are obtained by measuring 200 particles from TEM images. Scale bar represents 100 nm. (b) and (c) Atomic force micrograph of oligomer-grafted nanoplatelets. (b) Height image shows a nanoparticle with a hemispherical shape of 10 nm in height (inset, height profile of nanoparticle). (c) Phase image of the same nanoparticle reveals a stiffer phase in the shape of a hexagon at the base, width of 75 nm, which is attributed to the α -ZrP nanoplatelet and a softer hemispherical coat attributed to the oligomer in the center. (d) and (e) Photographic images of spray coated films. (d) Comparison of polyimide film (top, thickness 25 μm) and polyimide film spray-coated with smectic α -ZrP/epoxy film (bottom, thickness 8 μm) demonstrates a uniform, transparent coating. (e) A bent film spray-coated with smectic α -ZrP/epoxy film demonstrating flexibility of coating.

c



d



e



Figure 5.2 Continued.

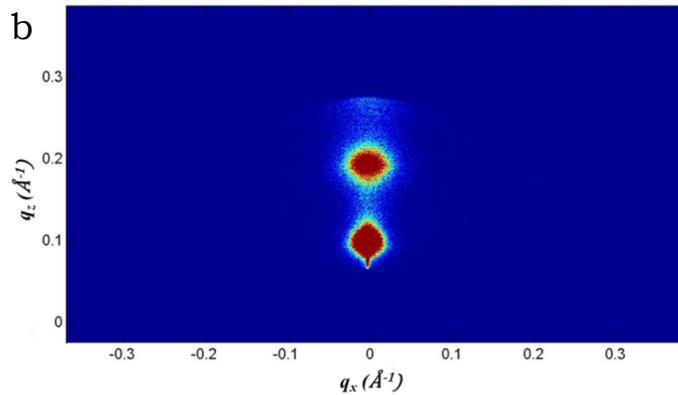
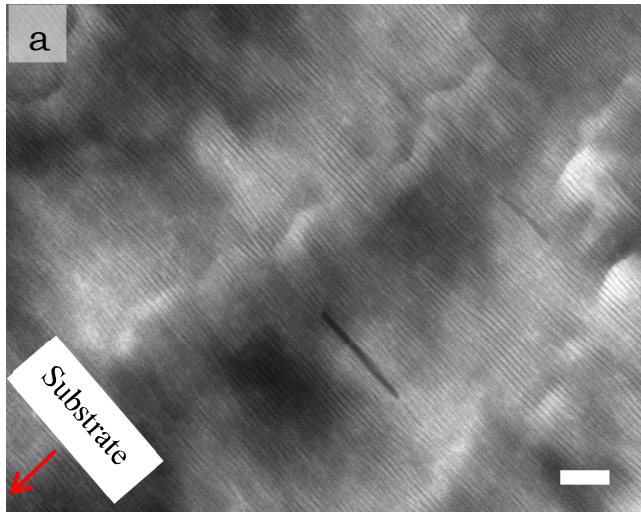


Figure 5.3 Evidence of smectic phase in spray-coated film. (a) Electron micrographs of smectic 2D crystal films (4.4 vol%). TEM of spray-coated film shows uniformly aligned nanoplalelets with d -spacing of 5 – 8 nm. Orientation of substrate is indicated by white box, red arrow indicates direction of substrate, scale bar denotes 50 nm. (b) – (c) Grazing-incidence small-angle x-ray diffractograms of nanocomposite film on a polyimide substrate. (b) 2D diffractogram, diffractions peaks appearing only in the q_z -axis, proving nanoplalelets are aligned parallel to the substrate. (c) 1D diffractogram, showing the first and second order peaks of smectic phase, d -spacing = 6.3 nm in agreement with TEM results. (d) Wide-angle x-ray diffractogram of film indicates presence of only higher order diffraction peaks (indicated by arrows, second to fifth order) from smectic α -ZrP and a broad amorphous peak, confirming that nanoplalelets are fully exfoliated. The combined data from GISAXS and WAXS confirms the lamellar structure of the nanoplalelet in the coating as $q_1 : q_2/q_1 : q_3/q_1 : q_4/q_1 : q_5/q_1 = 1 : 2 : 3 : 4 : 5$.

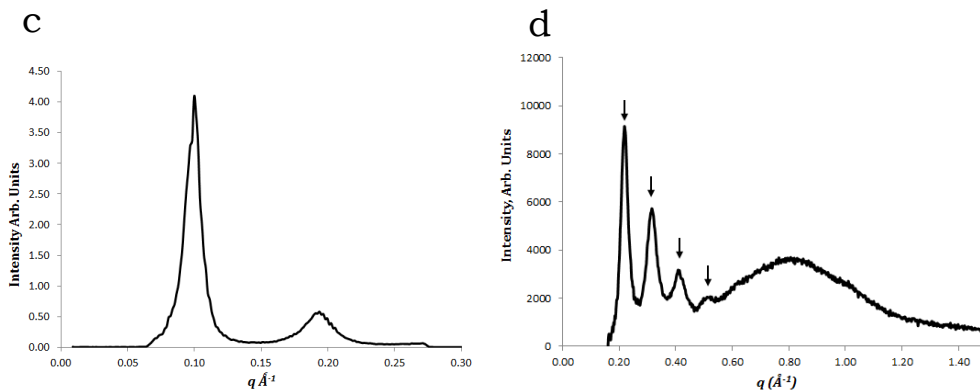


Figure 5.3 Continued.

5.4 Spray-coated α -ZrP/Epoxy Films

Spray-coated smectic α -ZrP/epoxy films were prepared on both polyimide (thickness 25 μ m Apical, Kaneka) and glass substrates (thickness 1mm, VWR). Thickness of the smectic films were controlled to 7 \pm 1 nm. The spray-coated polyimide films remained highly transparent and flexible after fully cured (Figure 5.2d & e).

Transmission electron microscopy shows that the mesomorphic nanoplatelets are uniformly aligned parallel to the substrate (Figure 5.3a). d -spacing was found to range from 5 – 8 nm. Grazing-incidence small-angle x-ray scattering (GISAXS) is a powerful tool suitable for probing the mesoscale structures of films or coatings (172, 173). The alignment of 2D crystals can be determined by observing the location of the interference peaks on the x - z plane of the 2D diffractogram. Lamellar structures that are aligned parallel to the substrate will display Bragg peaks in the vertical axis (q_z -axis), conversely, peaks appearing in the horizontal plane (q_x -axis) indicate a perpendicular alignment to the substrate (174) and curved features indicate an intermediate orientation. GISAXS studies of a 4.4 vol% smectic α -ZrP/epoxy spray-coated polyimide film

displayed the first and second order Bragg peaks characteristic of a lamellar phase exclusively in the q_z -axis indicating that the nanoplatelets are aligned parallel to the substrate (Figure 5.3b). Interlamellar distance was found to be 6.3 nm from the 1D diffractogram (Figure 5.3c), in close agreement with TEM results. Wide-angle x-ray scattering (WAXS) detected a broad amorphous peak; in addition to multiple higher order (up to the fifth order) Bragg peaks from the smectic phase, which indicates a high level of mesoscale order (Figure 5.3d). The absence of the characteristic peaks of stacked α -ZrP confirms that the nanoplatelets are fully exfoliated.

Optical microscopy reveals the occurrence of voids about 3 μm in diameter in a 4.4 vol% α -ZrP/epoxy coating (Figure 5.4a), which remarkably does not deter its gas barrier property (see below). This is explained by the fact that the voids do not form continuous pores through the thickness of the film. The occurrence of voids is found to be substrate dependent, as evidenced by the void-free coating formed on glass substrate (Figure 5.4c). The formation of voids is a result of the poorer spreading capability of α -ZrP/epoxy over polyimide. Polarized optical microscopy (POM) of the films coated on polyimide reveals a featureless black image except at the fringes of the voids where birefringence is observed (Figure 5.4b), while films coated on a glass substrate (not shown) display a completely featureless black image due to the complete absence of voids. This suggests that the optical axis of the nanoplatelets is aligned perpendicular to the direction of observation ($I75$), in agreement with the GISAXS results. Conversely, cross-sections of α -ZrP/epoxy films coated on polyimide and glass substrate (Figure 5.4d

& e) display strong birefringence which is consistent with nanoplatelets being aligned parallel to the substrate.

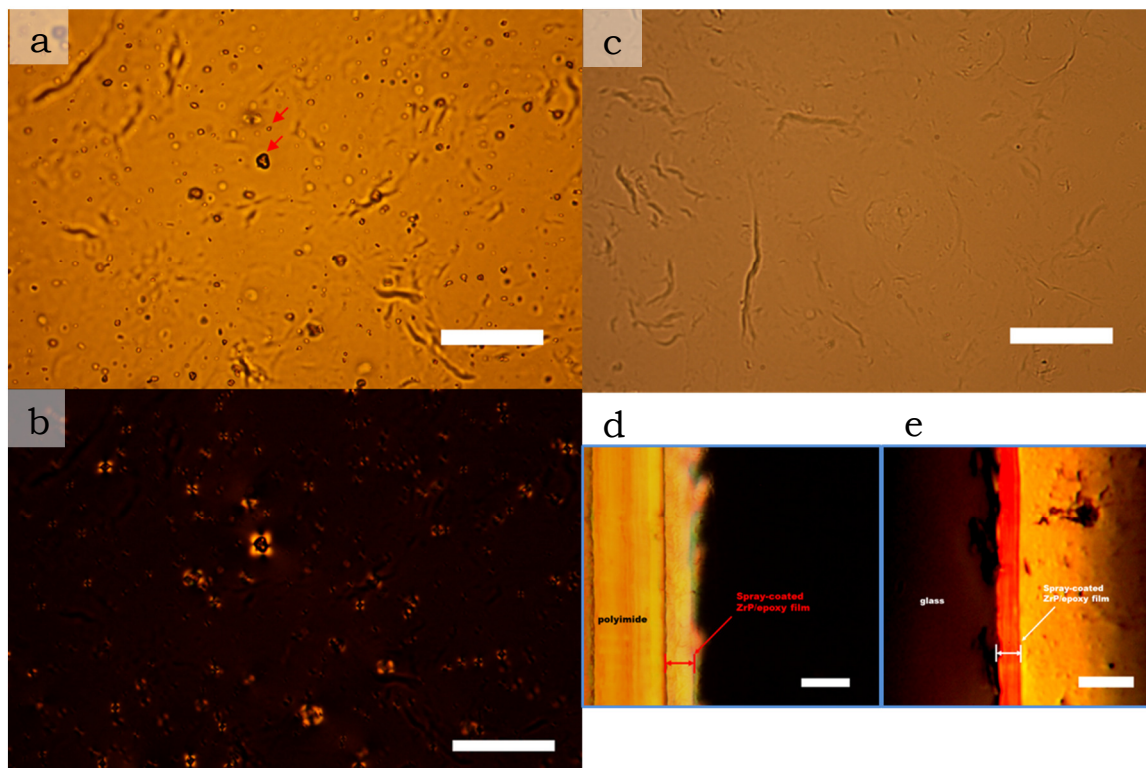


Figure 5.4 Optical microscopy of smectic (4.4 vol%) α -ZrP/epoxy films. (a) Transmission optical micrographs of smectic 2D crystal films on polyimide, voids are present (indicated by red arrows) throughout the film, however, this does not deter the gas barrier properties of the films (see below). (b) Polarized optical microscopy (POM) of the same area as a, except for the birefringent fringes of voids, film is black and featureless, suggesting that the optical axis of the nanoplatelets is aligned perpendicular to the direction of observation. (c) smectic 2D crystal films on glass, films are void free, suggesting that void formation is substrate dependent. Scale bars for a – c represents 50 μm . (d) POM of cross-sections of smectic 2D crystal films (thickness 13 μm) on polyimide (thickness 25 μm). Coating display strong birefringence indicating optical axis of the nanoplatelets is aligned parallel to the direction of observation, scale bar represents 20 μm . (e) POM of cross-sections of smectic 2D crystal films (thickness 4 μm) on glass (thickness 1 mm). Coating display strong birefringence, confirming previous observation, scale bar represents 10 μm .

5.5 Gas Barrier Properties of Spray-coated α -ZrP/Epoxy Films

The reduction of oxygen transmission rate of spray-coated smectic α -ZrP/epoxy films is significant. Compared to the bare polyimide films, a ten-fold reduction is achieved for $7 \pm 1 \mu\text{m}$ thick 4.4 vol% α -ZrP. As a reference, a similar reduction is achieved for $127 \pm 15 \mu\text{m}$ thick neat epoxy coats. Permeability of the spray-coated film can be obtained using the ideal laminate equation (176), the laminate permeability $P_{ILT} = (\phi_c/P_c + \phi_s/P_s)^{-1}$, where ϕ_c and ϕ_s are the volume fractions of coat and substrate, respectively. P_c and P_s are the permeabilities of coat and substrate, respectively. The permeability of the smectic α -ZrP/epoxy coated films exhibits more than twenty-fold reduction compared to polyimide and epoxy (Figure 5.5a). At relative humidity (RH) 0%, permeability of polyimide, epoxy and smectic α -ZrP/epoxy is 7.74, 5.89 and 0.26 cc mm/ m² day atm, respectively. At RH 50%, permeability of polyimide, epoxy (P_0) and smectic α -ZrP/epoxy (P) is 4.23, 3.60 and 0.15 cc mm/ m² day atm, respectively. At RH 90%, permeability of polyimide, epoxy and smectic α -ZrP/epoxy is 3.42, 3.15 and 0.15 cc mm/ m² day atm, respectively. Variability in permeability at low and high humidity levels remains consistently low, around ~ 0.1 cc mm/ m² day atm. In terms of relative permeability P/P_0 , the values are constant at around 0.04 \sim 0.05 at different humidity levels (Figure 5.5b). Permeability of bare and coated polyimide films is reduced in the presence of moisture. This is a well-known behavior of polyimide, which is explained by water molecules occupying Langmuir sites making them unavailable to oxygen molecules and competition in diffusion between water and oxygen molecules (177, 178). The behavior of these spray-coated films is the reverse of gas barrier films made by the *LbL* method.

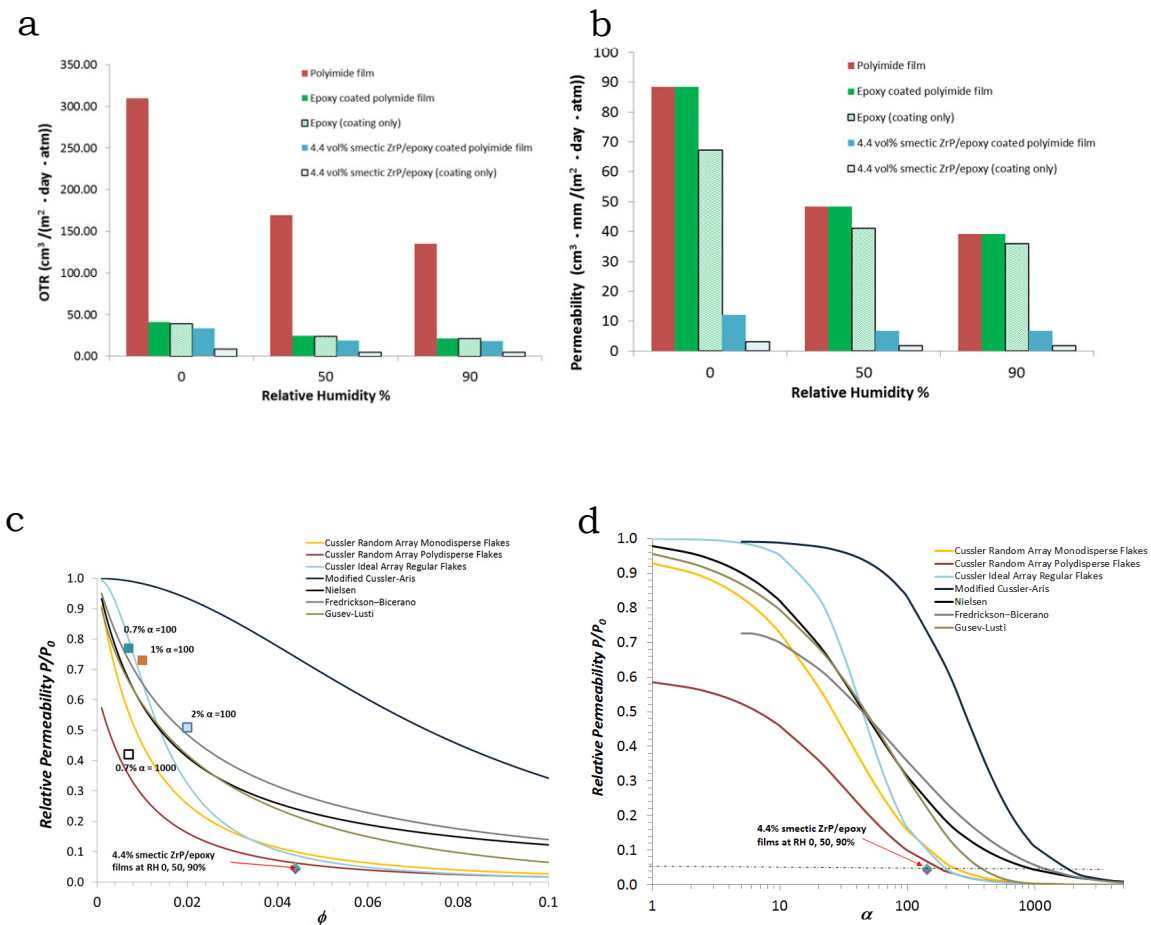


Figure 5.5 Gas barrier property of films. (a) Oxygen transmission rate (OTR) of films tested at three humidity levels. Epoxy was coated by a bar-coater onto polyimide films. OTR of smectic α -ZrP/epoxy coated films (thickness $7 \pm 1 \mu\text{m}$) exhibits a ten-fold reduction compared to polyimide, a similar reduction is achieved by epoxy only at a much larger thickness ($127 \pm 15 \mu\text{m}$). (b) Permeability of films tested at three humidity levels. Permeability of individual component was derived according to ideal laminate theory (see text). Permeability of smectic α -ZrP/epoxy coated films exhibits over twenty-fold reduction compared to polyimide and neat epoxy. Variability in permeability at low and high humidity levels remains consistently low. (c) Relative permeability plotted for comparison against previous experimental data from Sun et al. (squares) (179) and different models of permeability of barrier membranes. Relative permeability of smectic α -ZrP/epoxy films (diamonds) is constant at different humidity levels and all curves were plotted for nanoplatelets of aspect ratio $\alpha = 147$ (84, 85, 87, 88). (d) Comparison of experimental relative permeability for 4.4 vol% smectic α -ZrP/epoxy films with expected aspect ratios based on different models. All models predict a higher aspect ratio than actual value.

Models of the gas barrier effect of polymer filled with plate-like or flake-like inorganic particles have been proposed and studied for many years (84, 87, 88). Most of these models assume the plates are oriented perpendicular to the direction of gas flow and make predictions on the relative permeability as a function of ϕ and α (see Table 1.1). The data collected here were compared with the predictions of the models listed in Table 1.1 and it is apparent that all of them overestimate the relative permeability compared to experimental data (Figure 5.5c). The predictions of the models as a function of aspect ratio were plotted for $\phi = 0.044$ and compared with actual data (Figure 5.5d). Depending on the specific model, the predicted aspect ratio can range from 200 to 2000. Apparently, none of the models satisfactorily predicts the present data, although Cussler's model for random arrays of polydisperse flakes comes much closer than the others (86). The failure of the models can probably be understood as a consequence of individual dispersion of plates being explicitly assumed—an assumption which is invalidated when strong overlapping results in the case of a highly ordered arrangement of smectic α -ZrP nanoplatelets. We can thus view the superior performance of the present films as a result of an effective increase in aspect ratio due to the highly ordered mesoscale structure.

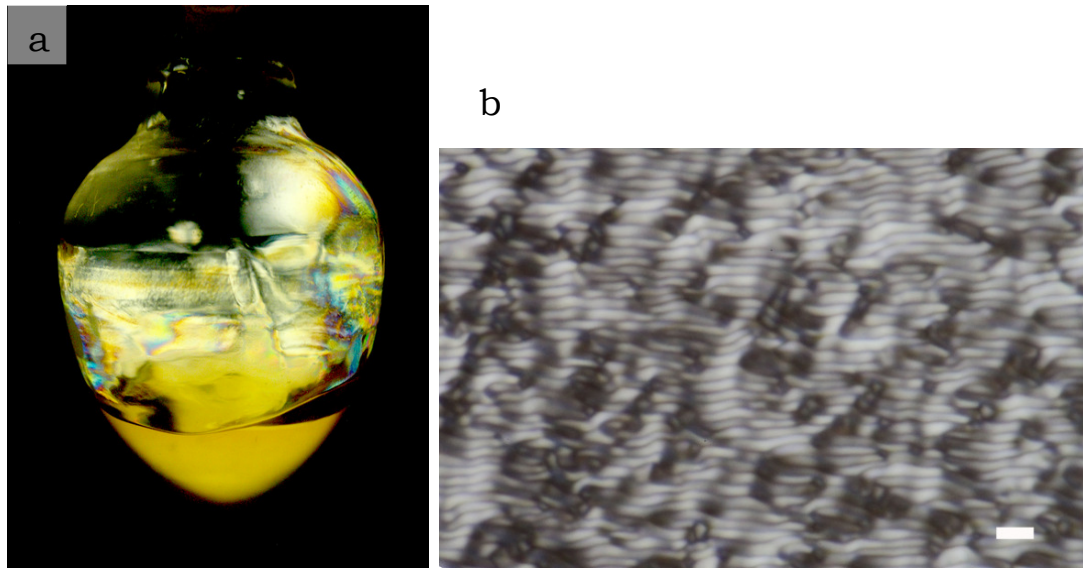


Figure 5.6 Smectic (4.0 vol%) α -ZrP/epoxy liquid. (a) Polarized optical microscopy (POM) of smectic α -ZrP/epoxy liquid show birefringence, strong interference colors can be observed in the thin films adhering to the glass wall. (b) Observation via POM of a drop of smectic liquid sandwiched between two glass plates show the banded structure texture, scale bar denotes 10 μm . (c) SAXS 2D diffractogram of the smectic liquid showing strong orientation of the smectic phase. (d) SAXS 1D diffractogram confirms the lamellar structure of the α -ZrP/epoxy liquid as $q_1 : q_2/q_1 : q_3/q_1 : q_4/q_1 = 1 : 2 : 3 : 4$. d -spacing was found to be 17.1 nm. (e) Rheology of smectic liquid at 25°C, viscosity and magnitude of first normal stress difference $|N_1|$ are plotted against shear rate. Viscosity of the smectic liquid showed more than three orders of magnitude in reduction at high shear rates. The first normal stress difference N_1 shows a hump at shear rates 10^{-3} to 1 s^{-1} , possibly an indication of shear flow generated by rotation of nanoplatelets. (f) Schematic showing the evolution of banded structure. Nanoplatelets rotate (R) while a shear flow (S) is generated in response to the shear applied globally. Dashed arrows indicate direction of shear flow, small arrows indicate direction of rotation, red arrows indicate direction of global applied shear, blue and yellow nanoplatelets indicate position before and after shear is applied, respectively.

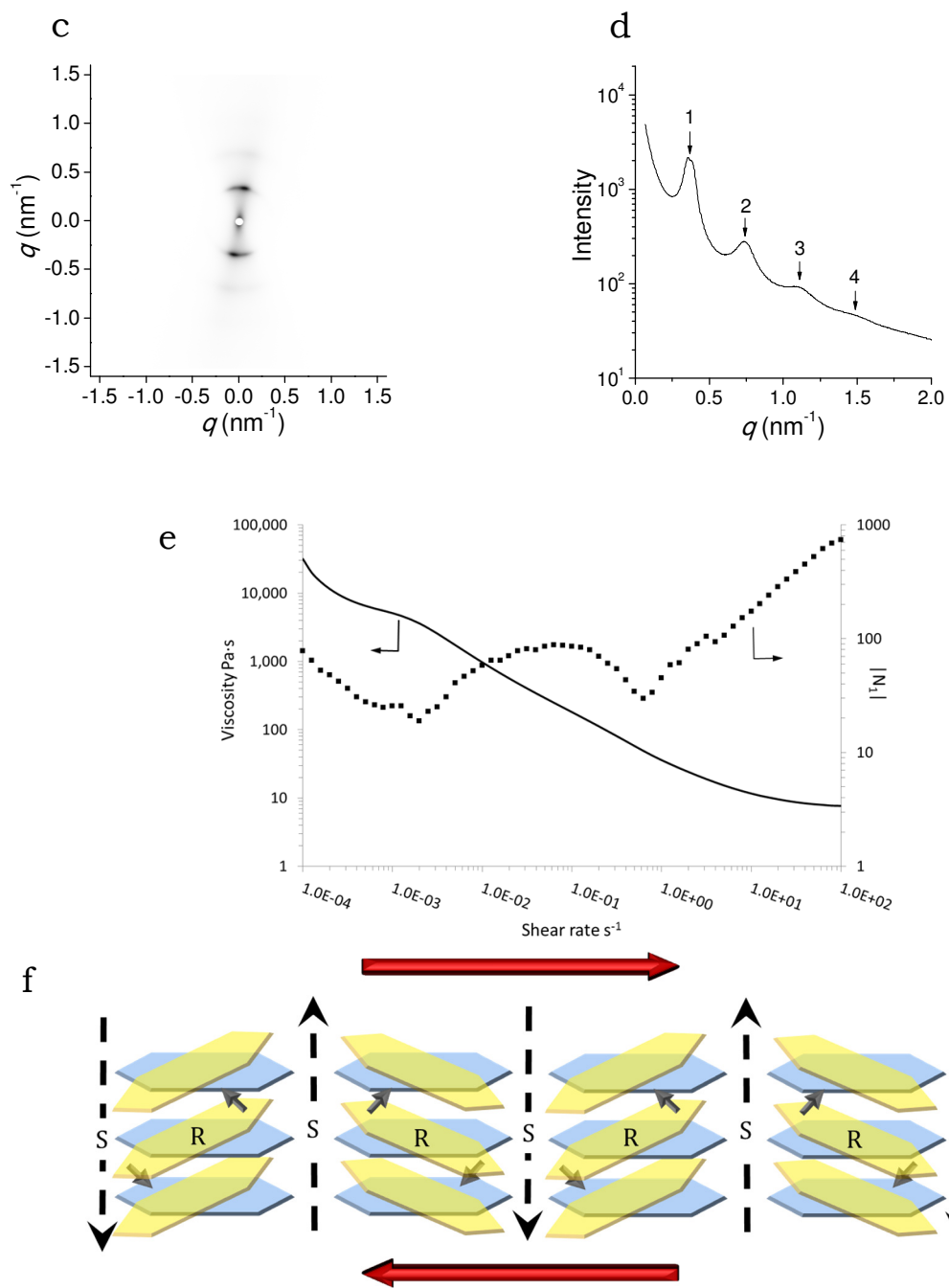


Figure 5.6 Continued.

5.6 Self-assembly Mechanism of Smectic α -ZrP/Epoxy Films

The self-assembly mechanism of smectic α -ZrP nanoplatelets is different from the self-assembly of colloidal particles at the liquid-air interface (173, 180, 181) and at the liquid-liquid interface (172). The presence of a significant amount of epoxy pre-polymer precludes the usual driving forces at the liquid-air interface to act effectively on the nanoplatelets. Instead, the sterically stabilized nanoplatelets are thermodynamically driven to form liquid crystalline phases in epoxy according to Onsager's theory (35, 182, 183). The removal of solvent allows the nanoplatelets to conform to the substrate, thus serving only a secondary role in directing the assembly of the smectic phase. Bulk liquid of sterically stabilized α -ZrP ($\phi = 0.040$) in epoxy was prepared, yielding a highly viscous liquid showing birefringence when observed between crossed-polarizers (Figure 5.6a), as expected with the presence of liquid crystallinity. When sandwiched between two glass plates, the liquid can be induced to display band-like structures (Figure 5.6b) that are superficially similar to the Grandjean textures associated with the twisted-grain-boundary (TGB) phase (184), a chiral smectic A phase which has also been shown to occur in graphene oxide nanosheets (41). However, it is believed that these banded structures are instead the result of local rotation of nanoplatelets (vide infra). SAXS diffractograms of the smectic liquid exhibit strong orientation (Figure 5.6c) and peaks characteristic of the lamellar structure, with d -spacing found to be 17.1 nm (Figure 5.6d). The smectic liquid displays a dramatic shear thinning behavior (Figure 5.6e), where viscosity can be reduced by more than 3 orders of magnitude to ~ 7 Pa·s, (neat epoxy ~ 5 Pa·s) at 25°C under high shear rates ($\sim 10^2$ s⁻¹). Similar shear thinning behavior has

previously been observed in aqueous liquid crystals of graphene oxide (163) and is attributed to the alignment of nanoplatelets to the flow direction. Normal forces in liquids are a measure of stored elastic energy during flow and are particularly sensitive to the presence of particles. The first normal stress difference N_I is defined as $(\tau_{11} - \tau_{22})$, where τ_{ii} are the normal stresses acting along the flow (185), shows a hump at shear rates 10^{-3} to 1 s^{-1} . This feature is possibly a result of the response of the liquid crystal to globally applied shear. Liquid-crystalline polymers are known to form banded structures under shear (186) similar to that observed in Figure 5.6b. The evolution of this banded structure is explained by the local rotation of nanoplatelets rotating to preserve local order while the global order relaxes (Figure 5.6f). A shear flow is generated in the direction normal to the shear direction while the liquid crystal relaxes. This shear flow will generate a force in the same direction of the flow, which is detected as an increase in N_I .

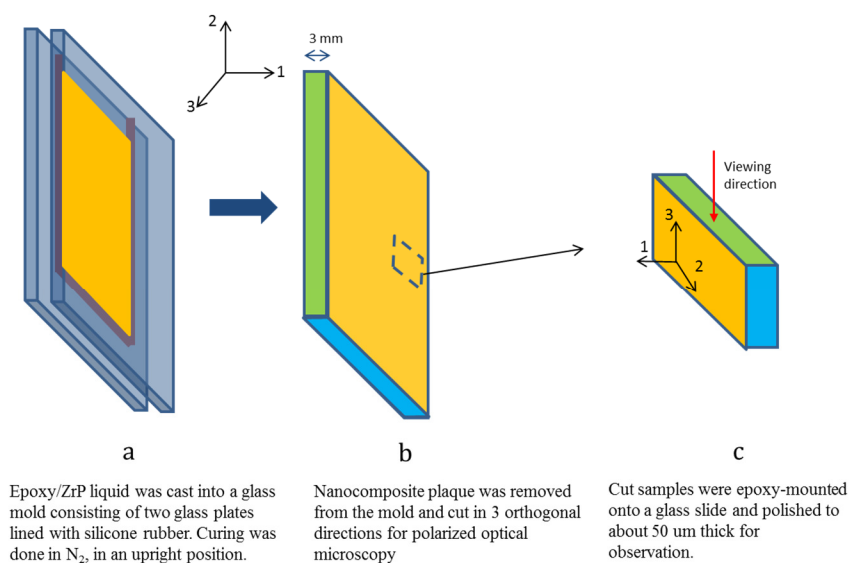


Figure 5.7 Molding process for α -ZrP/epoxy bulk nanocomposites.

The dramatic shear thinning property of the smectic liquid allows for it to be cast into an upright glass mold (prepared according to the process shown in Figure 5.7) and cured, forming a bulk nanocomposite plate. A section of the nanocomposite, taken in the direction parallel to the flow direction of the epoxy, was cut and polished. Polarized optical microscopy of this section reveals a skin-core morphology, with the skin showing high uniformity in color and the core showing a complex fingerprint texture (Figure 5.8a). The fingerprint texture has been associated with chiral smectic *A* phase in graphene oxide nanosheets (41). The orientation of the optical axis of the nanoplatelets was confirmed to be parallel to the sample stage by insertion of a retardation plate in the optical pathway and observing the change in interference colors (Figure 5.8b to f). This in turn confirms that the nanoplatelets in the skin region are oriented uniformly parallel to the glass mold that it was in contact with during casting, illustrating the substrate effect on aligning the nanoplatelets. SAXS confirms the lamellar structure of the nanoplatelets and a slight decrease in *d*-spacing to be 15.2 nm (Figure 5.8g & h), consistent with the shrinking of the polymer during curing. The smectic arrangement of the nanocomposite was imaged by TEM (Figure 5.9a), revealing long-range orientational and positional order of the nanoplatelets. Defect structures in the aligned nanoplatelets were observed by TEM tomography (TEM-T). Misaligned nanoplatelets were found to be the origin of zones of disordered nanoplatelets with larger inter-sheet spacing than the surrounding aligned nanoplatelets (Figure 5.9b). A full 3D TEM-T reconstruction of the nanocomposite confirms that the alignment of the nanoplatelets extends throughout the bulk of the material (Figure 5.9c). The direct transmission

electron imaging of defect structures at the mesogen level in liquid crystals is expected to contribute to the study of the evolution of such defect structures.

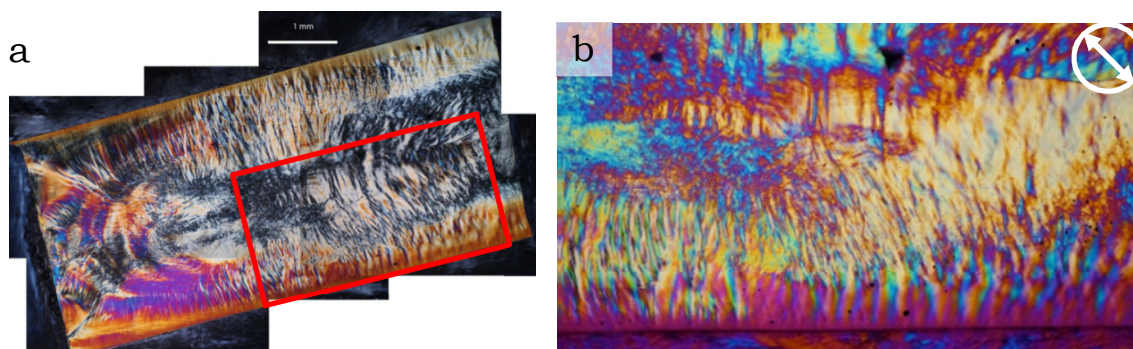


Figure 5.8 Smectic (4.4 vol%) α -ZrP/epoxy nanocomposite. (a) Composite image of the polarized optical microscopy (POM) of a section of smectic α -ZrP/epoxy nanocomposite observed in the direction parallel to the glass mold and perpendicular to the flow direction of the epoxy, scale bar denotes 1 mm. The difference in texture in the skin and core is apparent, with the skin showing high uniformity in color and the core showing a complex fingerprint texture. (b) – (f) Observation via POM with a retardation plate of $\Gamma=530$ nm inserted in the optical pathway, oriented in the north-east direction (indicated by the circle and double arrow located upper right corner). The region under observation is demarcated by the red box in **a**. The sample was oriented at the angles (b) 0° , (c) -20° , (d) -45° , (e) 20° and (f) 45° . The fingerprint texture seen in the figures are very similar to those associated with chiral liquid crystals of nanoplatelets (41). In (d) the observed region shows a bright yellow color, especially in the skin region, indicating relatively high birefringence and subtractive retardation. On the other hand, in (f) the same region shows a dark yellow-green color, indicating low birefringence and additive retardation. These results demonstrate that the optical axis of the sample aligns parallel to the sample stage on average (187). The POM results are consistent with nanoplatelets in the skin region being aligned parallel to the glass mold. (g) SAXS 2D diffractogram of the nanocomposite showing strong orientation of the smectic phase. (h) SAXS 1D diffractogram confirms the lamellar structure of the α -ZrP/epoxy nanocomposite as $q_1 : q_2/q_1 : q_3/q_1 : q_4/q_1 = 1 : 2 : 3 : 4$. d -spacing was found to be 15.2 nm.

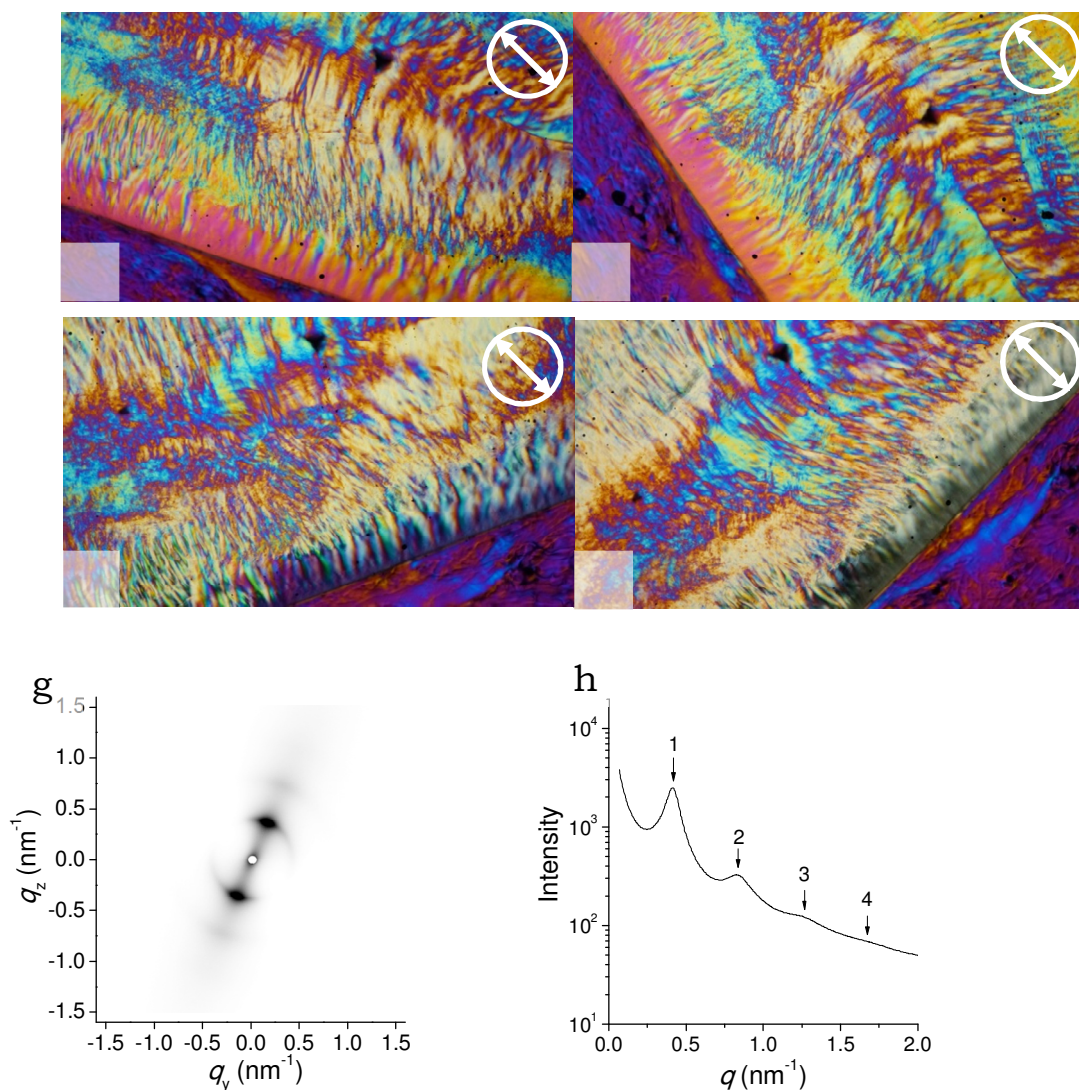


Figure 5.8 Continued.

Combined, the above results demonstrate the occurrence of smectic phase of the nanoplatelets in epoxy and the capacity of the nanoplatelets to be aligned in the epoxy liquid, supporting the assertion that liquid crystal formation is independent of solvent drying. The appearance of the smectic phase in the bulk epoxy liquid occurs at a lower volume fraction ($\phi = 0.040$) than an aqueous dispersion of α -ZrP ($\phi = 0.059$) (36). The large difference in d -spacings of bulk liquid (17.1 nm) and spray-coated films (6.3 nm)

suggest the considerable flowability of the epoxy liquid and the stability of the smectic phase. The d -spacing relation for lamellar structure $\phi = t/d$ predicts $\phi = 0.040$ for $d = 17.1$ nm and $t = 0.68$ nm, in perfect agreement with experimental results, suggesting that the nanoplatelets in the bulk liquid is a homogeneous dispersion. In comparison, the smaller d -spacing in spray-coated films is most likely a result of phase separation into nanoplatelet-rich phase ($\phi = t/d = 0.68/6.3 = 0.108$) and epoxy-rich phase. The most parsimonious explanation for these observations is that as the solvent is removed, the sterically stabilized nanoplatelets initially assemble into smectic phase with a small d -spacing (i.e. at high ϕ), likely aided by shear generated during solvent evaporation. The d -spacing in this initial smectic phase is likely a function of the chain length of the oligomer. In the bulk liquid, the shear thinning behavior of the epoxy liquid under high shear rates and elevated temperatures allows homogenization to occur and the epoxy to swell into the inter-layer space, expanding d -spacings (resulting in low ϕ) without disrupting the smectic phase. The flow of the bulk liquid during mechanical mixing likely further aligns the nanoplatelets and preserves the smectic phase.

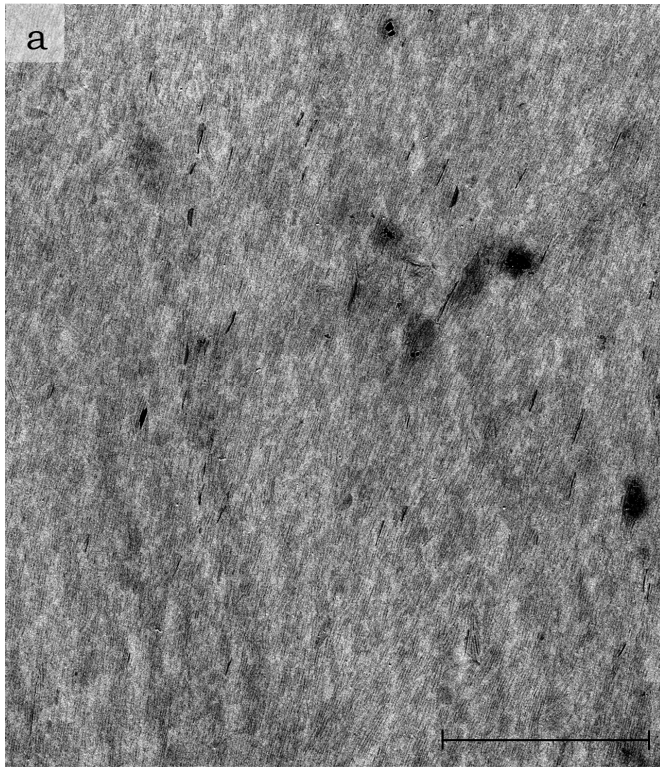


Figure 5.9 Transmission electron microscopy of smectic (4.4 vol%) α -ZrP/epoxy nanocomposite. (a) Large area transmission electron micrograph of the nanocomposite showing the long-range orientational and positional order of α -ZrP nanoplatelets, scale bar denotes 1 μm . The inter-sheet spacing was found to be 9–16 nm, in close agreement with the SAXS result of 15.1 nm. (b) – (f), TEM tomography of α -ZrP/epoxy nanocomposite. (b) to (e) A series of reconstructed tomograms of the nanocomposite, the scale bar denotes 50 nm. Misaligned nanoplatelets forms a core (red dashed circles) that disturbs the orderly arrangement of surrounding nanoplatelets, originating zones of high disorder with larger inter-sheet spacing (enclosed by red dashed lines), size of the zone of disorder progressively shrinks as the alignment of core is restored. (f) A 3D reconstruction of the nanocomposite showing the extent of alignment of the nanoplatelets. The 3D reconstruction also confirms that the orientational and positional order persists throughout the bulk of the nanocomposite.

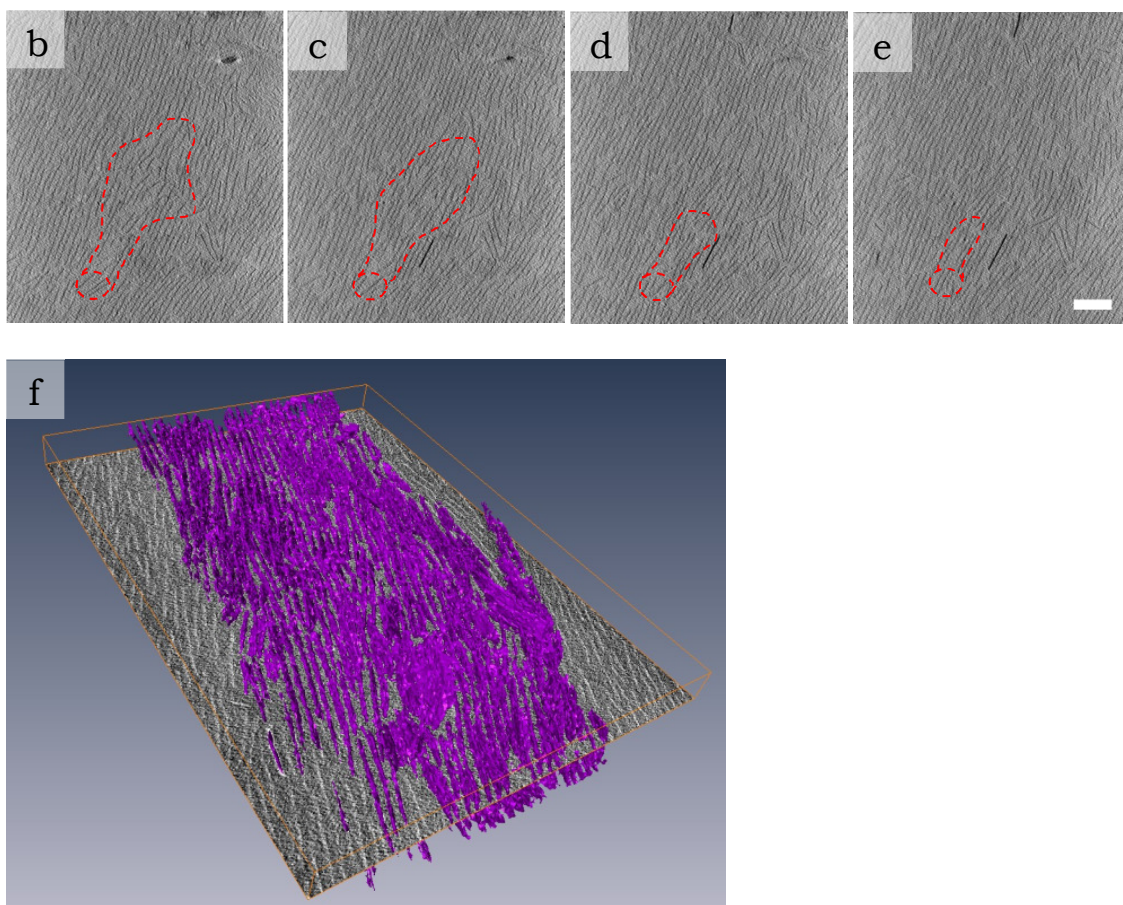


Figure 5.9 Continued.

5.7 Conclusions

Spray-coatable smectic 2D crystals/epoxy films represent an improvement in the practical, large-scale manufacturing and performance of gas barrier films; however, the significance extends beyond that. The stability of the smectic phase in epoxy, at lower than expected volume fractions, hint at possible broader application of this technology in the manufacture of bulk liquid crystalline materials. The ease of inducing the formation of exotic chiral phases also promises to expand the opportunities in studying such

phases, as is the ability to directly image the liquid crystals at the mesogen level. The rheology of the smectic epoxy liquid is favorable to large-scale manufacturing of bulk and fiber materials. Due to the wide selection of functional 2D crystal materials that can be incorporated into polymer matrices to yield mechanically robust and flexible form factors, this technology promises to be of interest to fields as diverse as electronics, catalysts, environmental, composite materials and others. This technology is expected to be particularly useful in making highly selective separation membranes, where smectic zeolite nanosheets can efficiently select the species that permeate through the membranes (188).

CHAPTER VI

CONCLUSIONS

It was shown in Chapters II and III that oligomer-grafted spherical nanoparticles can form fine and stable dispersions in polymer matrices. A high through-put processing technique of producing these nanocomposites is achievable as a result of the excellent melt-blendability of the oligomer-grafted nanoparticles. The grafting of the oligomers to the nanoparticles was accomplished via conventional radical polymerization that produced polydisperse brushes. It was shown that brush polydispersity enhances the stability of the nanoparticles. The high transparency of the nanocomposites reflects the uniform dispersion with little or no aggregation of nanoparticles. Glass transition temperature, refractive index and the energy bandgap were tunable as a linear function of ZnO quantum dots concentration. A glass transition model of thin polymer films was found to be applicable to the nanocomposites of this work, suggesting the underlying physics governing glass transition behavior in both kinds of materials are the same. We have thus successfully demonstrated that the grafting of oligomers onto nanoparticles led to creation of a multifunctional nanocomposite while achieved through practical methods.

In Chapter IV, large ZrP nanoplatelets tethered with polyoxyalkyleneamine dispersed in highly polar aprotic solvents self-assembles into lamellar structures. The interlamellar distance was 130 nm and larger, as a result, Bragg reflection in the visible wavelengths were observed. It is proposed that the tethered oligomers form a brush layer

that increased the repulsion between lamellae from the increased Debye screening length and repulsion between oligomer layers. The organic solutions of ZrP nanoplatelets exhibit brilliant iridescence, with colors that are tunable by adjusting the concentration of nanoplatelets. This novel route of manipulating 2D crystals in organic solvents potentially allows easier integration into manufacturing processes.

In Chapter V, it was shown that oligomer-tethered ZrP nanoplatelets homogenized in epoxy can be spray-coated onto a substrate to form smectic phase films. The smectic phase exhibit both orientational and positional order which remained stable under temperatures required to cure the epoxy. The nanoplatelets were aligned parallel to the substrate, which was verified by GISAXS, TEM and polarized optical microscopy. Furthermore, polyimide films spray-coated with smectic ZrP/epoxy films demonstrated over twenty fold reduction in permeability of oxygen at low and high humidity levels. Unlike previous methods of assembling nanostructures due to surface-driven mechanisms, the self-assembly mechanism of these films originates from the tendency of the nanoplatelets to organize into high ordered smectic phases as concentration increases following the behavior predicted by Onsager's theory. This was proven by showing that bulk α -ZrP/epoxy liquids also show clear evidence of liquid crystalline phases independent of the solvent removal process. This technology provides a simple and efficient way to achieve large-scale ordering of all types of 2D crystals that are amenable to colloidal modification. It is expected to become an important technique towards expanding the possibilities of unique and novel applications using 2D crystals of different materials.

The means by which nanoparticles can influence the functional properties of the nanocomposite or dispersion can be classified as follows:

- a. The nanoparticles impart properties that are intrinsic to the material that the nanoparticle is made of, which we refer to as an *intrinsic* effect. The UV absorption property of ZnO QDs is an example of this.
- b. The nanoparticles exert an effect on the polymer matrix leading to a change in functional property, which we refer to as an *extrinsic* effect. The glass transition behavior of ZnO/PMMA nanocomposite is an example of this.
- c. Functional properties arise as a result of assembled structures of the nanoparticles. This is termed as a *structural* effect. The iridescence of α -ZrP solutions is an example of this.

In practice, combinations of any of the three effects mentioned above can occur simultaneously. In the case of the gas barrier property of smectic α -ZrP/epoxy films, a combination of intrinsic and structural effects results in a synergistic, huge reduction of oxygen permeability in the films. This classification serves as a good way to understand the multitude ways that functional properties can arise with the incorporation of nanoparticles into an organic or polymeric media. In conclusion, the opportunities of creating useful new functional materials via the use of oligomers are indeed numerous and very promising. Through the successful examples given in the preceding chapters, we have shown that the ability to control the dispersion and organization of nanoparticles is critical to realizing this potential.

CHAPTER VII

FUTURE RESEARCH

7.1 Structured Nanoparticles in Melt-processable Polymers

As we have shown in the examples of iridescent α -ZrP solutions and smectic α -ZrP/epoxy films, asymmetrical arrangements of nanoparticles can result in the emergence of interesting properties. The realization of such structures in melt-processable polymers promises to greatly improve the ease of manufacturing such materials. To a certain degree, similar materials are already in existence in liquid crystalline polymers and carbon nanotube/polymer nanocomposites. However, a general method to prepare structured nanoparticle/polymer nanocomposites is yet to be developed. A few possible directions towards this goal are suggested in the following.

The stability, diffusion properties of oligomer-grafted nanoparticles in polymer as a function of nanoparticle geometry, *i.e.* 2D crystals, nanorods, nanotubes etc., and brush character, *i.e.* brush length, polydispersity, chemical structure etc., warrants further studies. Understanding these phenomena should allow better control of the organization and assembly of nanoparticles under melt-processing conditions. The realization of these goals may allow self-healing (189) and dramatic improvements in overall properties to emerge (45).

7.2 Phase Behavior and Preparation of Smectic α -ZrP/Epoxy

Understanding the phase behavior of smectic α -ZrP/epoxy is a critical issue that has direct implications on the prediction and control of the properties of the material. The phase transitions from isotropic to nematic to smectic phases are expected to be determined by a multitude of parameters including nanoplatelet concentration, aspect ratio and possibly oligomer size. Preliminary results not included in this dissertation suggest that interlamellar distance is dependent on the substrate. The presence of voids in α -ZrP/epoxy on polyimide films may have adversely affected the gas barrier property resulting in a measured permeability that is higher than its true value. These two examples point to the fact that even when the smectic phase is formed, there are subtle differences arising from the preparation method of the film. Clearly, there is a need to improve on film preparation to avoid these issues. Clarification of these phenomena is expected to be critical to the improvement of gas barrier properties.

7.3 Control and Stabilization of Photonic Structures of 2D Crystals

Perhaps the most important issue to realizing a practical application for the photonic crystals described in Chapter IV is in the stabilization of the photonic structures formed. The evaporation of the solvent will eventually lead to the collapse of the photonic structures and render it useless. To overcome this problem a way to “fix” the structure once it forms is required. This is most likely to be achieved by either introducing functionalities on the surface of the 2D crystals to form permanent bonds or inserting a polymer between the interlamellar spaces to stabilize the structure. Fortunately, the fact

that the photonic structures can be prepared in organic solvents allows a wide selection of compounds to be available for these purposes.

7.4 Exploring Novel Functional Properties with Different Form Factors

The methods described in this dissertation are general enough to be applicable to a broad range of materials. Exploring novel functional properties by selecting materials from this “library of materials” is therefore a natural extension of this work. Some worthy examples are suggested as follows:

- a. Electrically conductive materials such as graphene, metal nanoparticles and nanorods for electrically conductive inks, polymers, coats etc.
- b. Semiconductor materials such as metal oxides, metal chalcogenides in the form of 2D crystals for device applications.
- c. Magnetic materials that include iron, nickel and cobalt etc, in the form of nanoparticles, nanorods and 2D crystals for smart materials.
- d. Selectively permeable materials such as graphene oxide, zeolite nanosheets which can be spray-coated to form a uniform membrane that separate out the desired molecules from a mixture at high efficiencies.

Furthermore, the manufacturing methods described in this dissertation are flexible enough to allow different form factors to be prepared. For example, the ZnO/PMMA nanocomposites can be extruded into fibers or injection-molded into the final form. Similarly, the smectic α -ZrP/epoxy solutions can be converted into the form of fibrils through a coagulation bath or electrospaying. By coupling these techniques with the

materials suggested above, we can conceive of many different possible products engineered for a wide variety of applications.

REFERENCES

1. R. D. Tilton, T. Saigal, H. C. Dong, K. Matyjaszewski, Pickering emulsions stabilized by nanoparticles with thermally responsive grafted polymer brushes. *Langmuir* **26**, 15200 (2010).
2. K. Ohno, K. Koh, Y. Tsujii, T. Fukuda, Fabrication of ordered arrays of gold nanoparticles coated with high-density polymer brushes. *Angew. Chem. Int. Ed.* **42**, 2751 (2003).
3. M. K. Corbierre, N. S. Cameron, R. B. Lennox, Polymer-stabilized gold nanoparticles with high grafting densities. *Langmuir* **20**, 2867 (2004).
4. M. A. C. Stuart *et al.*, Emerging applications of stimuli-responsive polymer materials. *Nat. Mater.* **9**, 101 (2010).
5. D. Wang, E. W. Edwards, M. Chanana, H. Mohwald, Stimuli-responsive reversible transport of nanoparticles across water/oil interfaces. *Angew. Chem. Int. Ed.* **47**, 320 (2008).
6. B. P. Binks, R. Murakami, S. P. Armes, S. Fujii, Temperature-induced inversion of nanoparticle-stabilized emulsions. *Angew. Chem. Int. Ed.* **44**, 4795 (2005).
7. M. Motornov *et al.*, Stimuli-responsive colloidal systems from mixed brush-coated nanoparticles. *Adv. Funct. Mater.* **17**, 2307 (2007).
8. B. P. Binks, R. Murakami, S. P. Armes, S. Fujii, Effects of pH and salt concentration on oil-in-water emulsions stabilized solely by nanocomposite microgel particles. *Langmuir* **22**, 2050 (2006).

9. E. Katz *et al.*, "Chemical transformers" from nanoparticle ensembles operated with logic. *Nano Lett.* **8**, 2993 (2008).
10. Y. Q. Rao, S. Chen, Molecular composites comprising TiO₂ and their optical properties. *Macromolecules* **41**, 4838 (2008).
11. J. Pyun, S. Jia, T. Kowalewski, G. D. Patterson, K. Matyjaszewski, Synthesis and characterization of organic/inorganic hybrid nanoparticles: kinetics of surface-initiated atom transfer radical polymerization and morphology of hybrid nanoparticle ultrathin films. *Macromolecules* **36**, 5094 (2003).
12. D. A. Savin, J. Pyun, G. D. Patterson, T. Kowalewski, K. Matyjaszewski, Synthesis and characterization of silica-graft-polystyrene hybrid nanoparticles: effect of constraint on the glass-transition temperature of spherical polymer brushes. *J. Polym. Sci., Part B: Polym. Phys.* **40**, 2667 (2002).
13. B. Gu, A. Sen, Synthesis of aluminum oxide/gradient copolymer composites by atom transfer radical polymerization. *Macromolecules* **35**, 8913 (2002).
14. C. Xu, K. Ohno, V. Ladmiral, R. J. Composto, Dispersion of polymer-grafted magnetic nanoparticles in homopolymers and block copolymers. *Polymer* **49**, 3568 (2008).
15. M. M. Demir *et al.*, Optical properties of composites of PMMA and surface-modified zincite nanoparticles. *Macromolecules* **40**, 1089 (2007).
16. M. M. Demir, M. Memesa, P. Castignolles, G. Wegner, PMMA/zinc oxide nanocomposites prepared by in-situ bulk polymerization. *Macromol. Rapid Commun.* **27**, 763 (2006).

17. S. I. Yoo, B. H. Sohn, W. C. Zin, S. J. An, G. C. Yi, Self-assembled arrays of zinc oxide nanoparticles from monolayer films of diblock copolymer micelles. *Chem. Commun.*, **40**, 2850 (2004).
18. R. K. Čapek, M. Weber, A. Eychmüller, Alternative incorporation procedure of quantum dots in polymer microspheres. *Chem. Mater.* **22**, 4912 (2010).
19. L. Meli, A. Arceo, P. F. Green, Control of the entropic interactions and phase behavior of athermal nanoparticle/homopolymer thin film mixtures. *Soft Matter* **5**, 533 (2009).
20. P. G. Degennes, Conformations of polymers attached to an interface. *Macromolecules* **13**, 1069 (1980).
21. P. G. Ferreira, A. Ajdari, L. Leibler, Scaling law for entropic effects at interfaces between grafted Layers and polymer melts. *Macromolecules* **31**, 3994 (1998).
22. R. Hasegawa, Y. Aoki, M. Doi, Optimum graft density for dispersing particles in polymer melts. *Macromolecules* **29**, 6656 (1996).
23. I. Borukhov, L. Leibler, Enthalpic stabilization of brush-coated particles in a polymer melt. *Macromolecules* **35**, 5171 (2002).
24. A. Bansal *et al.*, Controlling the thermomechanical properties of polymer nanocomposites by tailoring the polymer–particle interface. *J. Polym. Sci., Part B: Polym. Phys.* **44**, 2944 (2006).
25. C. Chevigny *et al.*, Polymer-grafted-nanoparticles nanocomposites: dispersion, grafted chain conformation, and rheological behavior. *Macromolecules* **44**, 122 (2011).

26. P. Akcora *et al.*, Anisotropic self-assembly of spherical polymer-grafted nanoparticles. *Nat. Mater.* **8**, 354 (2009).
27. F. Lo Verso, S. A. Egorov, A. Milchev, K. Binder, Spherical polymer brushes under good solvent conditions: molecular dynamics results compared to density functional theory. *J. Chem. Phys.* **133**, (2010).
28. D. M. Trombly, V. Ganesan, Curvature effects upon interactions of polymer-grafted nanoparticles in chemically identical polymer matrices. *J. Chem. Phys.* **133**, (2010).
29. R. C. Salvarezza *et al.*, Edward-Wilkinson behavior of crystal surfaces grown by sedimentation of SiO₂ nanospheres. *Phys. Rev. Lett.* **77**, 4572 (1996).
30. M. Holgado *et al.*, Electrophoretic deposition to control artificial opal growth. *Langmuir* **15**, 4701 (1999).
31. P. Jiang, J. F. Bertone, K. S. Hwang, V. L. Colvin, Single-crystal colloidal multilayers of controlled thickness. *Chem. Mater.* **11**, 2132 (1999).
32. A. van Blaaderen, R. Ruel, P. Wiltzius, Template-directed colloidal crystallization. *Nature* **385**, 321 (1997).
33. L. Hong, A. Cacciuto, E. Luijten, S. Granick, Clusters of amphiphilic colloidal spheres. *Langmuir* **24**, 621 (2008).
34. S. Jiang *et al.*, Janus particle synthesis and assembly. *Adv. Mater.* **22**, 1060 (2010).

35. F. M. van der Kooij, H. N. W. Lekkerkerker, Formation of nematic liquid crystals in suspensions of hard colloidal platelets. *J. Phys. Chem. B* **102**, 7829 (1998).
36. D. Z. Sun, H. J. Sue, Z. D. Cheng, Y. Martinez-Raton, E. Velasco, Stable smectic phase in suspensions of polydisperse colloidal platelets with identical thickness. *Phys. Rev. E* **80**, (2009).
37. J.-C. P. Gabriel *et al.*, Swollen liquid-crystalline lamellar phase based on extended solid-like sheets. *Nature* **413**, 504 (2001).
38. D. Kleshchanok, P. Holmqvist, J.-M. Meijer, H. N. W. Lekkerkerker, Lyotropic smectic B phase formed in suspensions of charged colloidal platelets. *J. Am. Chem. Soc.* **134**, 5985 (2012).
39. J. E. G. J. Wijnhoven, D. D. van't Zand, D. van der Beek, H. N. W. Lekkerkerker, Sedimentation and phase transitions of colloidal gibbsite platelets. *Langmuir* **21**, 10422 (2005).
40. A. A. Verhoeff, H. N. W. Lekkerkerker, Direct observation of columnar liquid crystal droplets. *Soft Matter* **8**, 4865 (2012).
41. Z. Xu, C. Gao, Graphene chiral liquid crystals and macroscopic assembled fibres. *Nat. Commun.* **2**, 571 (2011).
42. S. Yoshihara, T. Ezaki, M. Nakamura, J. Watanabe, K. Matsumoto, Enhanced thermal conductivity of thermoplastics by lamellar crystal alignment of polymer matrices. *Macromol. Chem. Phys.* **213**, 2213 (2012).

43. V. Davis *et al.*, True solutions of single-walled carbon nanotubes for assembly into macroscopic materials. *Nat. Nanotechnol.* **4**, 830 (2009).
44. L. Ericson *et al.*, Macroscopic, neat, single-walled carbon nanotube fibers. *Science* **305**, 1447 (2004).
45. N. Behabtu *et al.*, Strong, light, multifunctional fibers of carbon nanotubes with ultrahigh conductivity. *Science* **339**, 182 (2013).
46. A. Geim, K. Novoselov, The rise of graphene. *Nat. Mater.* **6**, 183 (2007).
47. K. S. Novoselov *et al.*, Electric field effect in atomically thin carbon films. *Science* **306**, 666 (2004).
48. R. Mas-Balleste, C. Gomez-Navarro, J. Gomez-Herrero, F. Zamora, 2D materials: to graphene and beyond. *Nanoscale* **3**, 20 (2011).
49. M. Osada, T. Sasaki, Exfoliated oxide nanosheets: new solution to nanoelectronics. *J. Mater. Chem.* **19**, 2503 (2009).
50. L. Sun, W. J. Boo, H.-J. Sue, A. Clearfield, Preparation of \square -zirconium phosphate nanoplatelets with wide variations in aspect ratios. *New J. Chem.* **31**, 39 (2007).
51. J. Coleman *et al.*, Two-dimensional nanosheets produced by liquid exfoliation of layered materials. *Science* **331**, 568 (2011).
52. A. H. C. Neto, K. Novoselov, Two-dimensional crystals: beyond graphene. *Mater. Express* **1**, 10 (2011).
53. L. Onsager, The effects of shape on the interaction of colloidal particles. *Ann. N.Y. Acad. Sci.* **51**, 627 (1949).

54. Y. Grohens, M. Brogly, C. Labbe, M. O. David, J. Schultz, Glass transition of stereoregular poly(methyl methacrylate) at interfaces. *Langmuir* **14**, 2929 (1998).
55. J. L. Keddie, R. A. L. Jones, R. A. Cory, Interface and surface effects on the glass-transition temperature in thin polymer-films. *Faraday Discuss.*, 219 (1994).
56. G. B. DeMaggio *et al.*, Interface and surface effects on the glass transition in thin polystyrene films. *Phys. Rev. Lett.* **78**, 1524 (1997).
57. C. J. Ellison, J. M. Torkelson, The distribution of glass-transition temperatures in nanoscopically confined glass formers. *Nat. Mater.* **2**, 695 (2003).
58. K. Fukao, Y. Miyamoto, Glass transitions and dynamics in thin polymer films: Dielectric relaxation of thin films of polystyrene. *Phys. Rev. E* **61**, 1743 (2000).
59. J. A. Forrest, J. Mattsson, Reductions of the glass transition temperature in thin polymer films: probing the length scale of cooperative dynamics. *Phys. Rev. E* **61**, R53 (2000).
60. D. Long, F. Lequeux, Heterogeneous dynamics at the glass transition in van der Waals liquids, in the bulk and in thin films. *Eur. Phys. J. E* **4**, 371 (2001).
61. L. Hartmann, W. Gorbatschow, J. Hauwede, F. Kremer, Molecular dynamics in thin films of isotactic poly(methyl methacrylate). *Eur. Phys. J. E* **8**, 145 (2002).
62. J. S. Sharp, J. A. Forrest, Dielectric and ellipsometric studies of the dynamics in thin films of isotactic poly(methylmethacrylate) with one free surface. *Phys. Rev. E* **67**, 031805 (2003).
63. S. Herminghaus, K. Jacobs, R. Seemann, The glass transition of thin polymer films: some questions, and a possible answer. *Eur. Phys. J. E* **5**, 531 (2001).

64. K. L. Ngai, Mobility in thin polymer films ranging from local segmental motion, Rouse modes to whole chain motion: a coupling model consideration. *Eur. Phys. J. E* **8**, 225 (2002).
65. P. Rittigstein, R. D. Priestley, L. J. Broadbelt, J. M. Torkelson, Model polymer nanocomposites provide an understanding of confinement effects in real nanocomposites. *Nat. Mater.* **6**, 278 (2007).
66. A. Bansal *et al.*, Quantitative equivalence between polymer nanocomposites and thin polymer films. *Nat. Mater.* **4**, 693 (2005).
67. J. M. Kropka, K. W. Putz, V. Pryamitsyn, V. Ganesan, P. F. Green, Origin of dynamical properties in PMMA-C₆₀ nanocomposites. *Macromolecules* **40**, 5424 (2007).
68. H. Oh, P. F. Green, Polymer chain dynamics and glass transition in athermal polymer/nanoparticle mixtures. *Nat. Mater.* **8**, 139 (2009).
69. J. M. Kropka, V. G. Sakai, P. F. Green, Local polymer dynamics in polymer-C₆₀ mixtures. *Nano Lett.* **8**, 1061 (2008).
70. L. M. Mähger, E. J. Denton, N. J. Marshall, R. T. Hanlon, Mechanisms and behavioural functions of structural coloration in cephalopods. *J. R. Soc. Interface* **6**, S149 (2009).
71. R. M. Kramer, W. J. Crookes-Goodson, R. R. Naik, The self-organizing properties of squid reflectin protein. *Nat. Mater.* **6**, 533 (2007).
72. G. Platz, C. Thunig, H. Hoffmann, Iridescent phases in aminoxide surfactant solutions. *Progr Colloid Polym Sci* **83**, 167 (1990).

73. H. Hoffmann, Fascinating phenomena in surfactant chemistry. *Adv. Mater.* **6**, 116 (1994).
74. N. Satoh, K. Tsujii, Iridescent solutions resulting from periodic structure of bilayer membranes. *J. Phys. Chem.* **91**, 6629 (1987).
75. Early lights. *Nat. Mater.* **11**, 995 (2012).
76. E. Yablonovitch, Inhibited spontaneous emission in solid-state physics and electronics. *Phys. Rev. Lett.* **58**, 2059 (1987).
77. S. John, Strong localization of photons in certain disordered dielectric superlattices. *Phys. Rev. Lett.* **58**, 2486 (1987).
78. G. S. Roberts, R. Sanchez, R. Kemp, T. Wood, P. Bartlett, Electrostatic charging of nonpolar colloids by reverse micelles. *Langmuir* **24**, 6530 (2008).
79. J. Ge, L. He, J. Goebel, Y. Yin, Assembly of magnetically tunable photonic crystals in nonpolar solvents. *J. Am. Chem. Soc.* **131**, 3484 (2009).
80. M. C. D. Mourad, A. V. Petukhov, G. J. Vroege, H. N. W. Lekkerkerker, Lyotropic hexagonal columnar liquid crystals of large colloidal gibbsite platelets. *Langmuir* **26**, 14182 (2010).
81. F. M. van der Kooij, K. Kassapidou, H. N. W. Lekkerkerker, Liquid crystal phase transitions in suspensions of polydisperse plate-like particles. *Nature* **406**, 868 (2000).
82. J. A. C. Veerman, D. Frenkel, Phase behavior of disklike hard-core mesogens. *Phys. Rev. A* **45**, 5632 (1992).

83. D. van der Beek, H. N. W. Lekkerkerker, Liquid crystal phases of charged colloidal platelets. *Langmuir* **20**, 8582 (2004).
84. L. E. Nielsen, Models for the permeability of filled polymer systems. *J. Macromol. Sci., Part A: Chemistry* **1**, 929 (1967).
85. E. L. Cussler, S. E. Hughes, W. J. Ward Iii, R. Aris, Barrier membranes. *J. Membrane Sci.* **38**, 161 (1988).
86. N. K. Lape, E. E. Nuxoll, E. L. Cussler, Polydisperse flakes in barrier films. *J. Membrane Sci.* **236**, 29 (2004).
87. G. H. Fredrickson, J. Bicerano, Barrier properties of oriented disk composites. *J. Chem. Phys.* **110**, 2181 (1999).
88. A. A. Gusev, H. R. Lusti, Rational design of nanocomposites for barrier applications. *Adv. Mater.* **13**, 1641 (2001).
89. P. C. LeBaron, Z. Wang, T. J. Pinnavaia, Polymer-layered silicate nanocomposites: an overview. *Appl. Clay Sci.* **15**, 11 (1999).
90. P. B. Messersmith, E. P. Giannelis, Synthesis and barrier properties of poly(ϵ -caprolactone)-layered silicate nanocomposites. *J. Polym. Sci., Part A: Polym. Chem.* **33**, 1047 (1995).
91. K. Yano, A. Usuki, A. Okada, Synthesis and properties of polyimide-clay hybrid films. *J. Polym. Sci., Part A: Polym. Chem.* **35**, 2289 (1997).
92. K. S. Triantafyllidis, P. C. LeBaron, I. Park, T. J. Pinnavaia, Epoxy-clay fabric film composites with unprecedented oxygen-barrier properties. *Chem. Mater.* **18**, 4393 (2006).

93. W.-S. Jang, I. Rawson, J. C. Grunlan, Layer-by-layer assembly of thin film oxygen barrier. *Thin Solid Films* **516**, 4819 (2008).
94. M. A. Priolo, D. Gamboa, K. M. Holder, J. C. Grunlan, Super gas barrier of transparent polymer–clay multilayer ultrathin films. *Nano Lett.* **10**, 4970 (2010).
95. J. Lutkenhaus *et al.*, Anisotropic structure and transport in self-assembled layered polymer-clay nanocomposites. *Langmuir* **23**, 8515 (2007).
96. K. C. Krogman, J. L. Lowery, N. S. Zacharia, G. C. Rutledge, P. T. Hammond, Spraying asymmetry into functional membranes layer-by-layer. *Nat. Mater.* **8**, 512 (2009).
97. Y.-C. Li *et al.*, Flame retardant behavior of polyelectrolyte–clay thin film assemblies on cotton fabric. *ACS Nano* **4**, 3325 (2010).
98. A. Izquierdo, S. S. Ono, J. C. Voegel, P. Schaaf, G. Decher, Dipping versus spraying: exploring the deposition conditions for speeding up layer-by-layer assembly. *Langmuir* **21**, 7558 (2005).
99. Y. Kojima *et al.*, Mechanical-properties of nylon 6-clay hybrid. *J. Mater. Res.* **8**, 1185 (1993).
100. A. Usuki *et al.*, Synthesis of nylon 6-clay hybrid. *J. Mater. Res.* **8**, 1179 (1993).
101. D. Z. Sun *et al.*, Purification and stabilization of colloidal ZnO nanoparticles in methanol. *J. Sol-Gel Sci. Technol.* **43**, 237 (2007).
102. M. E. Mackay *et al.*, General strategies for nanoparticle dispersion. *Science* **311**, 1740 (2006).

103. M. Wong, R. Tsuji, S. Nutt, H. J. Sue, Glass transition temperature changes of melt-blended polymer nanocomposites containing finely dispersed ZnO quantum dots. *Soft Matter* **6**, 4482 (2010).
104. C. Merckle, J. Blümel, Bifunctional phosphines immobilized on inorganic oxides. *Chem. Mater.* **13**, 3617 (2001).
105. B. Rohe, W. S. Veeman, M. Tausch, Synthesis and photocatalytic activity of silane-coated and UV-modified nanoscale zinc oxide. *Nanotechnology* **17**, 277 (2006).
106. M. Kotecha, W. Veeman, B. Rohe, M. Tausch, NMR investigations of silane-coated nano-sized ZnO particles. *Microporous Mesoporous Mater.* **95**, 66 (2006).
107. D. Sun, H.-J. Sue, N. Miyatake, Optical properties of ZnO quantum dots in epoxy with controlled dispersion. *J. Phys. Chem. C* **112**, 16002 (2008).
108. C. L. Huang, T. Tassone, K. Woodberry, D. Sunday, D. L. Green, Impact of ATRP initiator spacer length on grafting poly(methyl methacrylate) from silica nanoparticles. *Langmuir* **25**, 13351 (2009).
109. X. W. Fan, L. J. Lin, P. B. Messersmith, Surface-initiated polymerization from TiO₂ nanoparticle surfaces through a biomimetic initiator: A new route toward polymer-matrix nanocomposites. *Compos. Sci. Technol.* **66**, 1198 (2006).
110. C. Li, J. Han, C. Y. Ryu, B. C. Benicewicz, A versatile method to prepare RAFT agent anchored substrates and the preparation of PMMA grafted nanoparticles. *Macromolecules* **39**, 3175 (2006).

111. W. Ma, H. Otsuka, A. Takahara, Poly(methyl methacrylate) grafted imogolite nanotubes prepared through surface-initiated ARGET ATRP. *Chem. Commun.* **47**, 5813 (2011).
112. S. Li *et al.*, Characterization of poly(2-hydroxyethyl methacrylate-silica) hybrid materials with different silica contents. *Polymer* **48**, 3982 (2007).
113. R. Palkovits *et al.*, Polymerization of w/o microemulsions for the preparation of transparent SiO₂/PMMA nanocomposites. *Langmuir* **21**, 6048 (2005).
114. Y. Q. Hu, S. X. Zhou, L. M. Wu, Surface mechanical properties of transparent poly(methyl methacrylate)/zirconia nanocomposites prepared by in situ bulk polymerization. *Polymer* **50**, 3609 (2009).
115. J.-Z. Zheng, X.-P. Zhou, X.-L. Xie, Y.-W. Mai, Silica hybrid particles with nanometre polymer shells and their influence on the toughening of polypropylene. *Nanoscale* **2**, 2269 (2010).
116. J. Y. Lee, Q. L. Zhang, T. Emrick, A. J. Crosby, Nanoparticle alignment and repulsion during failure of glassy polymer nanocomposites. *Macromolecules* **39**, 7392 (2006).
117. S. Gupta, Q. L. Zhang, T. Emrick, A. C. Balazs, T. P. Russell, Entropy-driven segregation of nanoparticles to cracks in multilayered composite polymer structures. *Nat. Mater.* **5**, 229 (2006).
118. D. Sun, W. N. Everett, M. Wong, H.-J. Sue, N. Miyatake, Tuning of the dispersion of ligand-free ZnO quantum dots in polymer matrices with exfoliated nanoplatelets. *Macromolecules* **42**, 1665 (2009).

119. M. V. Artemyev, A. I. Bibik, L. I. Gurinovich, S. V. Gaponenko, U. Woggon, Evolution from individual to collective electron states in a dense quantum dot ensemble. *Phys. Rev. B* **60**, 1504 (1999).
120. R. D. Kamien, A. J. Liu, Why is random close packing reproducible? *Phys. Rev. Lett.* **99**, 155501 (2007).
121. H. Döllefeld, H. Weller, A. Eychmüller, Semiconductor nanocrystal assemblies: Experimental pitfalls and a simple model of particle-particle interaction. *J. Phys. Chem. B* **106**, 5604 (2002).
122. A. Arceo, L. Meli, P. F. Green, Glass transition of polymer-nanocrystal thin film mixtures: role of entropically directed forces on nanocrystal distribution. *Nano Lett.* **8**, 2271 (2008).
123. H. C. Wong, A. Sanz, J. F. Douglas, J. T. Cabral, Glass formation and stability of polystyrene-fullerene nanocomposites. *J. Mol. Liq.* **153**, 79 (2010).
124. M. Born, E. Wolf, in *Principles of Optics : Electromagnetic Theory of Propagation, Interference and Diffraction of Light*. (Cambridge Univ. Press, Cambridge ; New York, ed. 7th expanded, 1999), pp. 89-94.
125. T. C. Choy, *Effective Medium Theory : Principles and Applications*. International series of monographs on physics (Clarendon Press, New York, Oxford [England] , 1999).
126. D. R. Lide, *CRC Handbook of Chemistry and Physics*. (CRC Press, Boca Raton, FL, ed. 79th, 1999).

127. Q. Chen, M. R. Lin, J. E. Lee, Q. M. Zhang, S. Yin, Nanocomposites with very large electro-optic effect and widely tunable refractive index. *Appl. Phys. Lett.* **89**, 141121 (2006).
128. D. Dukes *et al.*, Conformational transitions of spherical polymer brushes: synthesis, characterization, and theory. *Macromolecules* **43**, 1564 (2010).
129. Y. Tamai, T. Konishi, Y. Einaga, M. Fujii, H. Yamakawa, Mean-square radius of gyration of oligo(methyl methacrylate)s and poly(methyl methacrylate)s in dilute-solutions. *Macromolecules* **23**, 4067 (1990).
130. W. J. Brittain, S. Minko, A structural definition of polymer brushes. *J. Polym. Sci., Part A: Polym. Chem.* **45**, 3505 (2007).
131. J. Pyun, T. Kowalewski, K. Matyjaszewski, in *Polymer Brushes*. (Wiley-VCH Verlag GmbH & Co. KGaA, Weinheim [Germany], 2005), pp. 51-68.
132. J. J. Xu, F. Qiu, H. D. Zhang, Y. L. Yang, Morphology and interactions of polymer brush-coated spheres in a polymer matrix. *J. Polym. Sci., Part B: Polym. Phys.* **44**, 2811 (2006).
133. G. D. Smith, D. Bedrov, Dispersing nanoparticles in a polymer matrix: are long, dense polymer tethers really necessary? *Langmuir* **25**, 11239 (2009).
134. H. Oh, P. F. Green, Polymer chain dynamics and glass transition in athermal polymer/nanoparticle mixtures. *Nat Mater* **8**, 139 (2009).
135. S. Li *et al.*, Bulk synthesis of transparent and homogeneous polymeric hybrid materials with ZnO quantum dots and PMMA. *Adv. Mater.* **19**, 4347 (2007).

136. W. J. Seo *et al.*, Synthesis and properties of polyurethane/clay nanocomposite by clay modified with polymeric methane diisocyanate. *J. Appl. Polym. Sci.* **101**, 2879 (2006).
137. J. Typek, N. Guskos, A. Szymczyk, D. Petridis, FMR and DISC study of maghemite nanoparticles in PMMA polymer matrix. *J. Non-Cryst. Solids* **354**, 4256 (2008).
138. J. Xu, K. M. Razeeb, S. Roy, Thermal properties of single walled carbon nanotube-silicone nanocomposites. *J. Polym. Sci., Part B: Polym. Phys.* **46**, 1845 (2008).
139. J. D. P. Menczel, R. Bruce, Eds., *Thermal Analysis of Polymers : Fundamentals and Applications* (Wiley, Hoboken N.J. 2009).
140. E.-J. Donth, *Relaxation and Thermodynamics in Polymers: Glass Transition*. (Akademie Verlag, Berlin, ed. Reprint Edition: 1st 1992), pp. 355.
141. F. D. Blum, E. N. Young, G. Smith, O. C. Sitton, Thermal analysis of adsorbed poly(methyl methacrylate) on silica. *Langmuir* **22**, 4741 (2006).
142. H. B. Lu, S. Nutt, Restricted relaxation in polymer nanocomposites near the glass transition. *Macromolecules* **36**, 4010 (2003).
143. C. C. M. Ma, Y. J. Chen, H. C. Kuan, Polystyrene nanocomposite materials - preparation, mechanical, electrical and thermal properties, and morphology. *J. Appl. Polym. Sci.* **100**, 508 (2006).
144. S. M. Scholz, R. Vacassy, J. Dutta, H. Hofmann, M. Akinc, Mie scattering effects from monodispersed ZnS nanospheres. *J. Appl. Phys.* **83**, 7860 (1998).

145. T. Tsuzuki, Abnormal transmittance of refractive-index-modified ZnO/organic hybrid films. *Macromol. Mater. Eng.* **293**, 109 (2008).
146. G. Adam, J. H. Gibbs, On temperature dependence of cooperative relaxation properties in glass-forming liquids. *J. Chem. Phys.* **43**, 139 (1965).
147. L. H. Sperling, *Introduction to Physical Polymer Science* (Wiley-Interscience, New York, ed. 3rd, 2001).
148. Ref [61] reported T_g shifts that support the Long-Lequeux model, however a recent update to Ref [61] published in A. Serghei, L. Hartmann and F. Kremer, *J. of Non-Cryst. Solids* **353**, 4330-4333 (2007) reports no T_g shifts and corrects the earlier report due to an error in data analysis.
149. Y. Grohens, L. Hamon, G. Reiter, A. Soldera, Y. Holl, Some relevant parameters affecting the glass transition of supported ultra-thin polymer films. *Eur. Phys. J. E* **8**, 217 (2002).
150. R. Priestley, M. K. Mundra, N. J. Barnett, L. J. Broadbelt, J. M. Torkelson, Effects of nanoscale confinement and interfaces on the glass transition temperatures of a series of poly(n-methacrylate) films. *Aust. J. Chem.* **60**, 765 (2007).
151. C. E. Porter, F. D. Blum, Thermal characterization of PMMA thin films using modulated differential scanning calorimetry. *Macromolecules* **33**, 7016 (2000).
152. G. J. Fleer, *Polymers at Interfaces* (Chapman & Hall, London ; New York, ed. 2, 1998).

153. J. M. Kropka, V. Pryamitsyn, V. Ganesan, Relation between glass transition temperatures in polymer nanocomposites and polymer thin films. *Phys. Rev. Lett.* **101**, 075702 (2008).
154. T. Ramanathan *et al.*, Functionalized graphene sheets for polymer nanocomposites. *Nat. Nanotechnol.* **3**, 327 (2008).
155. C. Thunig, H. Hoffmann, G. Platz, P. Bothorel, in *Trends in Colloid and Interface Science III: vol 79 of Progress in Colloid and Polymer Science*. E. Dufourc, Ed. (Springer Berlin / Heidelberg, 1989), pp. 297-307.
156. M. A. Haque, T. Kurokawa, J. P. Gong, Anisotropic hydrogel based on bilayers: color, strength, toughness, and fatigue resistance. *Soft Matter* **8**, 8008 (2012).
157. H. Masunaga *et al.*, Multipurpose soft-material SAXS/WAXS/GISAXS beamline at SPring-8. *Polym. J.* **43**, 471 (2011).
158. M. F. Hsu, E. R. Dufresne, D. A. Weitz, Charge stabilization in nonpolar solvents. *Langmuir* **21**, 4881 (2005).
159. T. Okubo, Extraordinary behavior in the structural properties of colloidal macroions in deionized suspension and the importance of the Debye screening length. *Acc. Chem. Res.* **21**, 281 (1988).
160. L. Sun, W. J. Boo, R. L. Browning, H.-J. Sue, A. Clearfield, Effect of crystallinity on the intercalation of monoamine in α -zirconium phosphate layer structure. *Chem. Mater.* **17**, 5606 (2005).

161. N. Koizumi, T. Hanai, Dielectric properties of polyethylene glycols: dielectric relaxation in solid state (special issue on polymer chemistry, I). *Bull. Inst. Chem. Res., Kyoto Univ.* **42**, 115 (1964).
162. H.-N. Kim, S. W. Keller, T. E. Mallouk, J. Schmitt, G. Decher, Characterization of zirconium phosphate/polycation thin films grown by sequential adsorption reactions. *Chem. Mater.* **9**, 1414 (1997).
163. Z. Xu, C. Gao, Aqueous liquid crystals of graphene oxide. *ACS Nano* **5**, 2908 (2011).
164. P. Fratzl, Biomimetic materials research: what can we really learn from nature's structural materials? *J. R. Soc. Interface* **4**, 637 (2007).
165. D. E. Horacio, E. R. Jee, B. Francois, J. B. Markus, Merger of structure and material in nacre and bone – perspectives on de novo biomimetic materials. *Prog. Mater Sci.* **54**, (2009).
166. H. Sugimori, T. Nishi, H. Jinnai, Dual-axis electron tomography for three-dimensional observations of polymeric nanostructures. *Macromolecules* **38**, 10226 (2005).
167. A. Clearfield, G. D. Smith, Crystallography and structure of α -zirconium bis(monohydrogen orthophosphate) monohydrate. *Inorg. Chem.* **8**, 431 (1969).
168. A. Clearfield, D. S. Thakur, Zirconium and titanium phosphates as catalysts: a review. *Appl. Catal.* **26**, 1 (1986).
169. A. Díaz *et al.*, Nanoencapsulation of insulin into zirconium phosphate for oral delivery applications. *Biomacromolecules* **11**, 2465 (2010).

170. G. Alberti, M. Casciola, Composite membranes for medium-temperature PEM fuel cells. *Annu. Rev. Mater. Res.* **33**, 129 (2003).
171. W. J. Boo *et al.*, Morphology and mechanical behavior of exfoliated epoxy/ α -zirconium phosphate nanocomposites. *Compos. Sci. Technol.* **67**, 262 (2007).
172. T. Paik, D.-K. Ko, T. R. Gordon, V. Doan-Nguyen, C. B. Murray, Studies of liquid crystalline self-assembly of GdF_3 nanoplates by in-plane, out-of-plane SAXS. *ACS Nano* **5**, 8322 (2011).
173. A. Saunders, A. Ghezelbash, D.-M. Smilgies, M. Sigman, B. Korgel, Columnar self-assembly of colloidal nanodisks. *Nano Lett.* **6**, 2959 (2006).
174. P. Busch, D. Posselt, D. M. Smilgies, M. Rauscher, C. M. Papadakis, Inner structure of thin films of lamellar poly(styrene-*b*-butadiene) diblock copolymers as revealed by grazing-incidence small-angle scattering. *Macromolecules* **40**, 630 (2007).
175. T. Nakato *et al.*, Electrooptic response of colloidal liquid crystals of inorganic oxide nanosheets prepared by exfoliation of a layered niobate. *J. Phys. Chem. C* **115**, 8934 (2011).
176. A. P. Roberts *et al.*, Gas permeation in silicon-oxide/polymer (SiO_x/PET) barrier films: role of the oxide lattice, nano-defects and macro-defects. *J. Membrane Sci.* **208**, 75 (2002).
177. R. T. Chern, W. J. Koros, E. S. Sanders, R. Yui, "Second component" effects in sorption and permeation of gases in glassy polymers. *J. Membrane Sci.* **15**, 157 (1983).

178. F. Piroux, E. Espuche, R. Mercier, The effects of humidity on gas transport properties of sulfonated copolyimides. *J. Membrane Sci.* **232**, 115 (2004).
179. L. Sun, W. J. Boo, A. Clearfield, H. J. Sue, H. Q. Pham, Barrier properties of model epoxy nanocomposites. *J. Membrane Sci.* **318**, 129 (2008).
180. N. Denkov *et al.*, Mechanism of formation of two-dimensional crystals from latex particles on substrates. *Langmuir* **8**, 3183 (1992).
181. T. P. Bigioni *et al.*, Kinetically driven self assembly of highly ordered nanoparticle monolayers. *Nat. Mater.* **5**, 265 (2006).
182. M. C. D. Mourad, E. J. Devid, M. M. van Schooneveld, C. Vonk, H. N. W. Lekkerkerker, Formation of nematic liquid crystals of sterically stabilized layered double hydroxide platelets. *J. Phys. Chem. B* **112**, 10142 (2008).
183. J.-C. Gabriel, P. Davidson, in *Colloid Chemistry I : vol. 226 of Topics in Current Chemistry*. M. Antonietti, Ed (Springer, Berlin / Heidelberg, 2003), pp. 119-172.
184. J. W. Goodby *et al.*, Characterization of a new helical smectic liquid crystal. *Nature* **337**, 449 (1989).
185. S. B. Kharchenko, J. F. Douglas, J. Obrzut, E. A. Grulke, K. B. Migler, Flow-induced properties of nanotube-filled polymer materials. *Nat. Mater.* **3**, 564 (2004).
186. C. Viney, W. S. Putnam, The banded microstructure of sheared liquid-crystalline polymers. *Polymer* **36**, 1731 (1995).
187. R. E. Stoiber, S. A. Morse, *Crystal Identification with the Polarizing Microscope*. (Chapman & Hall, New York, 1994), pp. 358.

188. K. Varoon *et al.*, Dispersible exfoliated zeolite nanosheets and their application as a selective membrane. *Science* **334**, 72 (2011).
189. A. C. Balazs, T. Emrick, T. P. Russell, Nanoparticle polymer composites: where two small worlds meet. *Science* **314**, 1107 (2006).